October 2012

Analysis and Testing of a Nano-Positioning Stage

Alex Damien Rutfield
Worcester Polytechnic Institute

Jeremy William Hagger
Worcester Polytechnic Institute

Joon-Ho Joseph Lee
Worcester Polytechnic Institute

Project Number NAG1201

ANALYSIS AND TESTING OF A NANO-POSITIONING STAGE

A Major Qualifying Project Report

Submitted to the Faculty

of the

WORCESTER POLYTECHNIC INSTITUTE

in partial fulfillment of the requirements for the

Degree of Bachelor of Science

in Mechanical Engineering

By:

_____

Jeremy Hagger

_____

Joon-Ho Lee

_____

Alex Rutfield

Date:

13 October 2012

Approved By:

_____

Nikolaos A. Gatsonis, Ph.D., Advisor
Mechanical Engineering Department, WPI

_____

Farshid Neylon-Azad, Affiliate Advisor
Group 74, MIT Lincoln Laboratory

Abstract

This project performed at the MIT Lincoln Laboratory characterizes the performance of a nano-positioning stage to be used in a laser communications system. The nano-positiong stage (NPS) is composed of a flexured linear stage and is actuated by piezo crystals in two degrees of freedom. The project involves the design of fixtures, finite element analysis, and experiments to predict performance, strength and dynamic response of the NPS. The results presented address the NPS performance characteristics of creep, hysteresis, total travel, cross-axis response, and temperature survivability. Recommendations for future testing and improvements of the current baseline design are presented.

Table of Contents

Acknowledgements

The project team would like to acknowledge and thank the following persons who played an integral role in helping us with this project:

• Farshid Neylon-Azad, MIT Lincoln Laboratory Project Advisor

• Professor Nikolaos Gatsonis, Ph.D., WPI Project Advisor

• Professor Ted Clancy, Ph.D., WPI – LL Site Advisor

• Lawrence Narkewich, Group 71 Engineer

• David Mandeville, Group 72 Fabrication Liaison

• Mike Shatz- Group 74 Leader

• Peter Lively, MIT Lincoln Laboratory Project Advisor

• Richard Cummings, Group 76

Authorship

Section Name	Primary Writer	Primary Editor
Chapter 1- Introduction	JH	AR&JL
1.1 Laser Communications and the LL Nano-Positioning System	JH&JL	AR
1.2 Laser Communication Systems and the Nano-Positioning System	JH&JL	AR
1.2.1 Coarse Adjustments	AR	JH&JL
1.2.2 Fine Adjustments and the Nano-Positioning Stage	JH	AR&JL
1.3 NPS Performance and Environmental Requirements	JL	AR&JH
1.3.1 Total Travel Requirements	JH	AR&JL
1.3.2 Open-Loop Accuracy Requirements	JL	AR&JH
1.3.3 Other Requirements of the NPS	JH	AR&JL
1.4 Project Goals, Objectives and Methodology	JH	AR&JL
Chapter 2- Finite Element Modeling and Analyses	JL	AR&JH
2.1 Room Temperature	JL	AR&JH
2.2 Thermal	JL	AR&JH
2.3 Vibration	JL	AR&JH
Chapter 3- Designs for NPS Test Fixtures	AR	JH&JL
3.1 Testing Features	AR&JL	JH
3.2 Room Temperature Test Fixture	AR	JH&JL
3.3 Thermal Test Fixture	AR	JH&JL
3.4 Vibration Test Fixture	AR	JH&JL
Chapter 4- Experimentation and Data Analysis	AR&JH	JL

4.1 Testing Setup	AR	JH&JL
4.1.1 Software	AR	JH&JL
4.1.2 Hardware	AR	JH&JL
4.1.3 Kaman Eddy-Current Sensors	AR	JH&JL
4.2 Room Temperature Tests	AR&JL	JH
4.2.1 Sensor Drift	AR	JH&JL
4.2.2 Creep	JL	AR&JH
4.2.3 Total Travel	JL	AR&JH
4.2.4 Hysteresis	JL	AR&JH
4.2.5 Resolution	JH	AR&JL
4.3 Temperature Tests	AR&JH&JL	AR&JH&JL
4.3.1 Thermal Sensor Drift	AR	JH&JL
4.3.2 Survival Cycling	JH	AR&JL
4.3.3 Thermal Actuation	JL	AR&JH
Chapter 5- Conclusions and Recommendations	AR&JH	JL
5.1 Conclusions	AR&JH	JL
5.1.1 FEA vs. Experimentation	JL	AR&JL
5.1.2 Total Travel	AR	JH&JL
5.1.3 Open-Loop Accuracy	AR	JH&JL
5.1.4 10 Mil Flexures vs. 12 Mil Flexures	JL	AR&JH
5.1.5 Temperature Survival	AR	JH&JL
5.2 Design Recommendations	JH	AR&JL

5.2.1 Target Assembly	JH	AR&JL
5.2.2 10 Mil Flexure Thickness	JH	AR&JL
5.2.3 Total Travel Budget	AR&JH	JL
5.3 Testing Recommendations	JH	AR&JL
5.3.1 Room Temperature	AR	JH&JL
5.3.2 Thermal	JH	AR&JL
5.3.3 Vibration	JH	AR&JL
5.3.4 Closed-Loop Testing	JH	AR&JL
5.4 Summary	AR	JH&JL

List of Tables

List of Figures

Acronym Definitions

Acronym	Definition
CTE	**Coefficient of Thermal Expansion**
DAQ	**Data Acquisition**
FEA	**Finite Element Analysis**
MIT LL	**Massachusetts Institute of Technology Lincoln Laboratory**
MQP	**Major Qualifying Project**
NI	**National Instruments**
NPS	**Nano-Positioning Stage**
PI	**Physik Instrumente**
Rcv Fiber	**Receiving Fiber**
RF	**Radio Frequency**
RTD	**Resistance Temperature Detectors**
SWAP	**Size Weight and Power**
Tx Fiber	**Transmit Fiber**
VI	**Virtual Instrument**
WPI	**Worcester Polytechnic Institute**

Chapter 1 – Introduction

MIT Lincoln Laboratory (MIT LL) is a federally-funded research and development facility and is government-owned, contractor-operated with a budget of nearly $1B. It works with the United States' Department of Defense, as well as a vast array of other sponsors. The Engineering Division (Division 7) of MIT LL designs and builds advanced technology systems in partnership with the other divisions within MIT LL. These systems are used in various programs and are also designed for testing, prototyping and operating purposes. In order to meet the requirements of the different systems, MIT LL relies on Division 7's extensive capabilities including, but not limited to, mechanical design and analysis, mechanical fabrication, system integration, environmental testing, and optical system design and analysis (Massachusetts Institute of Technology: Lincoln Laboratory [MIT LL], 2012).

Within Division 7, the Engineering Analysis and Testing Group (known as Group 74) is involved in many programs, including laser communications, as well as sensor communication payloads. Group 74 designs, fabricates and tests components and full systems to support hardware development. In addition to its design expertise, Group 74 also performs a wide-range of analyses and testing services, including thermal, structural, optical, aerodynamic and integrated analyses and testing for surface, airborne, and space borne communications systems and sensors (MIT LL, 2012). This Major Qualifying Project (MQP) group is embedded within a MIT LL program, in which Division 7 is tasked with designing and building the optical subsystem of a laser communication system. Division 6 is performing pointing, acquisition and tracking component of the program as well developing the communications hardware that will interface with the optical subsystem. This program is a Level 1 Program, so it has very high visibility and importance to MIT LL as a whole. Our MQP with Group 74 is involved in the

analysis and testing of one of the components of the laser communication system called a Nano-Positioning Stage (NPS). This NPS controls the pointing of the transmitted beam as it exits the optical subsystem. This MQP will provide conclusions as to whether the stage meets its design performance requirements, and recommendations for possible design improvements to the NPS.

1.1 Laser Communications and the LL Nano-Positioning System

Optical signals have been part of defense, public and private communication systems for centuries, from Ancient Roman soldiers who reflected sunlight from their shields to send battle signals (Majumdar & Ricklin, 2008), to the Chinese who used fire and smoke beacon towers along the Great Wall to warn of enemy invasions. The latest efforts in communication systems involve the use of lasers to encode data for many different types of communication links (Figure 1). Lasers are becoming more popular for communications over conventional microware radio frequency (RF) communication devices because of their narrow transit beam width, smaller antennas, lower power requirements and higher bandwidth (Hemmati, 2009; Lambert & Casey, 1995). MIT LL is working to push the boundaries of the next generation of communication systems with laser and fiber optic technology by reducing size weight and power (SWAP).

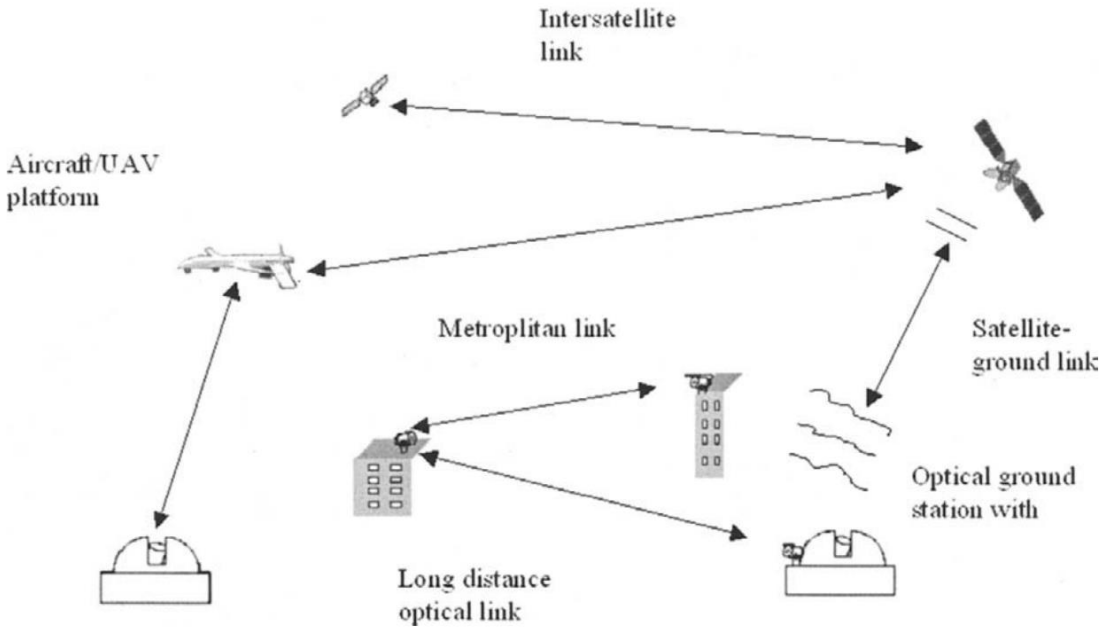

Figure 1: Examples of various Free-Space Laser Communications Architectures (Majumdar & Ricklin, 2008, p. 4)

Though most technological challenges involving laser communication have been resolved, fine beam pointing for long range communications to various earth orbits, and strategies to mitigate cloud coverage still require the most attention from laser communication system developers (Hemmati, 2009; Lambert & Casey, 1995). Currently, MIT LL is working on resolving one of these problems: designing a laser communication system that can precisely point optical beams over large distances. Notably, the lab is focusing on one of the most challenging aspects of free-space communication, i.e. laser beam pointing to and/or from a moving platform. The problem of laser communication can be broken down into optical line-of-sight stabilization and the provision of the appropriate pointing reference to the receiver location. Stabilization is usually achieved by using a high bandwidth control loop to sense and correct for the platform jitter. Pointing reference to the receiver is generally achieved by providing a beacon from the receiver location (Hemmati, 2009). While other laser communication systems have the ability to function over free space and over long distances, what makes MIT LL's system unique

is it's stability during constant platform movement and changes in environment while retaining micro-radian scale pointing accuracy.

1.2 Laser Communication Systems and the Nano-Positioning System

In designing a laser communication system to transmit high data rate communication over long distances, there are three significant challenges that must be overcome: (1) pointing, (2) acquisition and (3) tracking (Katzman, 1987). Acquisition is the process of initially locating one terminal from another, and it is performed using a relatively broad beam. The acquisition period for the MIT LL's laser communication system is at most 2 minutes. The beam is transmitted in a search pattern in the general direction of the relay, which has uncertainty in its position. This is done using coarse adjustments. Once initial contact is made, the two terminals are able to track each other through local angular disturbances using internal active elements, and switch to a narrower, higher power beam. After the two terminals have locked onto each other, the communication link needs to be kept stable through relative cross velocities and motions of the two terminals (Hemmati, 2009). The most difficult of these three steps to achieve is the maintenance of the communication link. Disturbance rejection platforms are one way to compensate for vibration and provide mechanical isolation for the communicating device. These platforms can provide coarse and fine adjustments to accurately position a beam in the same way that high-end microscopes can provide coarse and fine adjustments to focus on an image.

1.2.1 Coarse Adjustments

In precision aiming systems, coarse and fine adjustments are required to maintain a connection with the receiver. The coarse adjustment is used to adjust position to within the range of the fine adjustment mechanism, while the fine adjustments displace smaller amounts and in our case, only fractions of microns. This is very similar to the way a microscope is controlled. In

order to focus an optical microscope two knobs are used. The first knob moves the lens multiple orders of magnitude greater than the second knob. The first knob described would be the coarse adjustment while the second knob would be the fine adjustment.

1.2.2 Fine Adjustments and the Nano-Positioning Stage

MIT LL has developed a NPS for the purpose of fine adjustment that will support and position a Transmit Fiber (Tx Fiber) (Figure 2), as well as a Receiving Fiber (Rcv Fiber). The Rcv Fiber is on a separate stage that is identical and mirrored to the transmit stage, and it will not be tested and analyzed in this MQP.

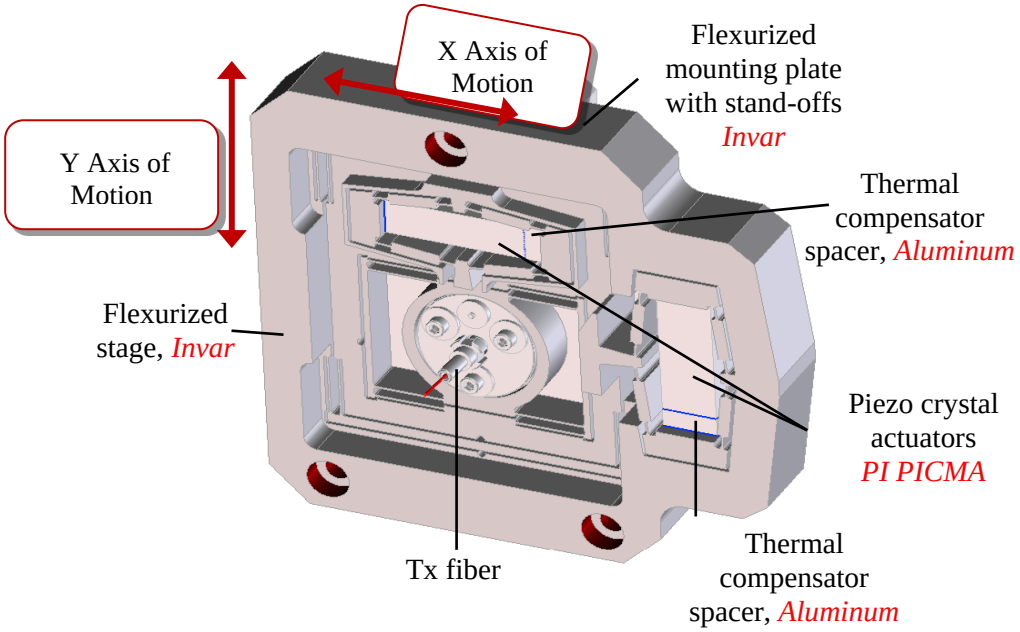

Figure 2: Labeled NPS with parts and their materials

The materials used in the design of the NPS were selected in order to make the Tx fiber housed in the center of the NPS as stable as possible through a variety of environmental conditions (i.e. changes in temperature) and performance factors. The various components of the NPS are discussed below.

1.2.2.1 Piezo Crystal Actuators

The fiber stage operates using two PICMA Multilayer Piezo Stack Actuators. Piezo stack actuators are a class of smart material, in which a crystal elongates or contracts when stimulated by a voltage. The voltage across the crystals causes a change within the crystal lattice of the material, making the crystals elongate or contract (generating mechanical strain). Within the NPS, as the crystals expand, they displace flexures causing the Tx fiber to actuate. As can be seen in the design (Figure 3), crystal expansion in the X axis causes the Tx fiber to move in the positive Y axis. Likewise, crystal expansion in the Y axis causes the Tx fiber to move in the positive X axis.

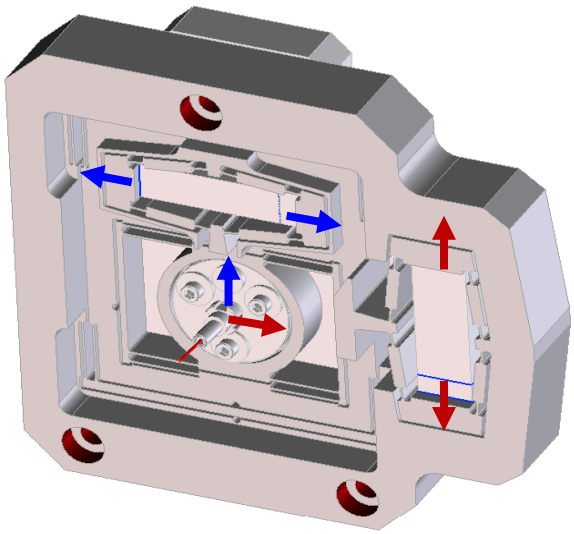

Figure 3: Piezo crystal actuation causes movement of the Tx fiber

The elongation of the crystal is on the order of fractions of microns at its smallest, and increases with applied voltage. A voltage of 100 volts causes a displacement in the crystals used in the system of 15 ± 10% microns (Physik Intstrumente, 2008), amplified to >100 microns through mechanical advantage offered by the stage's flexure design. This process allows for very precise movements of the Tx fiber in the X and Y axes.

1.2.2.2 Flexurized Stage

The assembly in which all of the other components are housed is made up of flexures that allow the Tx fiber to move very linearly in the X and Y axes with actuations of the crystals. The flexures are placed so that motion in one axis does not cause motion in the other axis. The purpose of the flexures is to amplify the actuations of the crystals by creating a mechanical advantage. With the use of flexures that create a mechanical advantage, the amount of travel of the Tx fiber is limited by the geometry of the flexures and not the elongation of the crystal. Our testing was completed on a NPS design with flexure thicknesses of 0.012" (12 mils). Analyses were done on a NPS design with flexure thicknesses of 12 mils, as well as 0.010" (10 mils).

The stage is composed of an Invar material (annealed Invar 36), due to its low coefficient of thermal expansion (CTE). A low CTE allows for minimal movement of the NPS with changes in temperature, and subsequently minimal movement of the Tx fiber.

1.2.2.3 Thermal Compensator Spacer

Unlike the invar stage, the Piezo crystal stack has a negative CTE in the polling direction. A negative CTE causes the crystal to shrink as temperature increases. Ideally, the Piezo crystal needs to have the same CTE as the invar stage so that the thermal expansion of the crystal does not actuate the stage with temperature changes. For this reason, an aluminum thermal compensator spacer is used to balance the negative CTE, so that the total CTE of the combined crystal/compensator mimics the CTE of the invar stage (Appendix A: Coefficient of Thermal Expansion**)**. The spacer, crystal, and stage are assembled using a high strength, aerospace grade adhesive.

1.2.2.4 Compression Springs

Compression springs are required to keep the Piezo actuators in compression. The Piezo actuators need to be under compression to give the crystals greater tensile strength. Under compression, the tensile strength of the crystal increases. If the crystal is not under compression, the odds of failure due to stresses increase. Two different size springs were used to compensate for the different sizes of the two Piezo actuators. The placement of the springs can be seen in Figure 12.

1.3 NPS Performance and Environmental Requirements

To ensure that the NPS design meets system level requirements, MIT LL devised a set of requirements shown in Table 1 and Table 2 based on the pointing error budget for the optical fiber. The performance requirements for the NPS relate to the movements of the Tx fiber through the actuations of the Piezo crystal, while the environmental requirements relate to the survivability of the NPS through exposure to extreme temperatures and vibrations. In Table 1 and Table 2, the requirements of total travel and open-loop accuracy are marked as values “To Be Determined” (TBD) and have been subsequently resolved through our tests and analyses of the stage.

Table 1: Performance Specifications

Category	Requirement	Value
Performance Specs	Total Travel	TBD
	Resolution	0.06 μm
	Open-loop accuracy	TBD
	Cross-axis response in X and Y (over full stroke)	2 μm
	Z-axis response (over full stroke)	30 μm
	Velocity	5 μ/s
	Acceleration	10 μ/s2
	Allowable tilt (X and Y)	± 1/2°

Table 2: Environment Specifications

Category	Requirement	Value
Environment Specs	Temperature • Operational (under thermal control) • Survival (requirement for internal hardware)	 25°C to 35°C -40°C to 70°C
	Shock Input	20G, 25 msec, half-sine

1.3.1 Total Travel Requirements

The Piezo crystals are to be loaded from 0 volts to 100 volts in their operation. The total travel of the Tx fiber is the distance the fiber traverses as a result of this voltage change. The total travel needed by the NPS is to be determined based on a set of requirements (Table 3). As can be seen in Table 3, the amount of stroke needed for thermal actuation is the only value that is listed as unknown. This value has been subsequently determined by measuring the displacement in the Tx fiber over the operational temperature range of 25 °C to 35 °C. Table 3 shows the

different contributors for the total travel requirements. During the course of this paper, the thermal actuation of the NPS will be solved for. The other values in Table 3 are known values.

Table 3: Total Stroke Requirements

Contributor	Value (µm)	Comments
Point ahead	± 4.7	
Boresight stroke	± 7	
Steer off 1.5 pixels	± 8.4	
Alignment	± 25	Misc. mechanical
Thermal actuation		Due to -CTE of Piezo Crystal
Thermal drift	± 0.26	Due to stage mounting
System level thermal drift	± 10	Due to optics
Sub Total		Total stroke needed

Point ahead refers to the need to be able to aim the laser slightly ahead of the relay in order to remain connected while the relay is in motion. The value is based upon the distance between the NPS and the relay, as well as the difference in velocities of the two components. The boresight stroke ensures that sights of the "gun" are aligned with the "barrel of the gun." In this case the sites are the others optics (what we are closing the loop on), and the gun is the Tx fiber. If they were not lined up, the laser would not be able to transmit through the NPS. "Steer off 1.5 pixels" takes into account the need to steer the beam off of bad pixels on the acquisition detector (if required). This needs to be taken into account in the total travel. The alignment term allows for small adjustments during optical alignment to optimize performance. Thermal actuation is caused by the differences in CTE for each of the materials in the NPS. It is expected to be small as design considerations were taken to mitigate these effects. Thermal drift is due to changes in the optic bench due to thermal effects. As the rest of the optics bench moves due to changes in temperature, so too will the NPS. This will affect how the NPS lines up during

boresighting. Thermal actuation is caused by internal changes in the stage, while thermal drift is caused by external changes. System level thermal drift is caused by the mirrors and lenses in the system. It is very similar to the thermal drift but it refers to the optics of the system.

1.3.2 Open-Loop Accuracy Requirements

During operation, it is desirable for the NPS to function open loop. In controls, open-loop control is defined as a control system in which there is no feedback, such as a position sensing. This means that the stage will not communicate back with the controller during the acquisition period. This is contrary to closed-loop control in which the device being controlled will give feedback on important parameters, which allows the controller to make changes based upon the feedback. Although the use of closed-loop control is commonit is desirable to accomplish all of the goals of the NPS using open-loop control. Open-loop control would make the device far less complicated and less expensive to produce. It would also reduce SWAP which is very constrained in this application. If the NPS does not meet its open-loop accuracy requirement, the open-loop concept will have to be reconsidered and a more conventional closed-loop approach will have to be taken.

The open loop accuracy budget (Table 4) is given as ±0.6 μm displacement at the fiber tip (in image space), or . ±2.5 μradians(in object space). . This conversion comes from several parameters including the focal length and the system magnification. Using equation (1) below, a specification for linear open loop accuracy can be derived from angular open-loop accuracy.

$$x = m * f * tan(\Theta) \quad (1)$$

$x = linear\ accuracy$

$m = system\ magnification$

$\Theta = angular\ accuracy$

$f = focal\ length$

The system magnification and focal length in Equation (1) are a function of the system optical design form. The parameters that comprise the open-loop accuracy of the NPS are creep, thermal drift, thermal actuation and hysteresis and will be discussed in detail in Chapter 4.

Table 4: Open-Loop Accuracy Budget

Error source	Value (µm)	Comments
Thermal actuation		Over 1 °C change
Creep		Over 2 min acquisition
Thermal Drift		Over 1 °C change
Hysteresis		Max applied voltage of 9.4 V
Sub Total		Requirement of ±0.6 µm

Open-loop accuracy is only a factor during the acquisition period, and thus all of the parameters only need to be considered for the two minute period. During this period, the NPS will encounter a maximum of 1 °C temperature change, a factor which is accounted for in the open-loop accuracy budget. Once the NPS has acquired the relay, the controller will have feedback on position from the return signal, and will no longer be operating with open-loop control. The NPS operates open loop through the point-ahead voltage range of ±4.7 volts (9.4 volts).

1.3.3 Other requirements of the NPS

Though total stroke and open-loop accuracy are the most important characteristics of the NPS that our tests and analyses involve, our testing of the NPS involve other parts of the performance and environment specifications in order to ensure that they meet their necessary

requirements. These include resolution, cross-axis response, Z-axis response, allowable tilt, temperature survivability, and shock.

1.3.3.1 Resolution

The voltage applied to the crystals changes in steps rather than in a continuous manner, which is due to the controller of the system; the smaller the voltage increments, the more expensive the controller. There is no need to spend resources on a controller that has better specifications than needed. The minimum resolution of the Tx fiber is 0.06 μm. The value for the resolution is determined by the smallest applied voltage to the crystals that can produce a readable displacement. The smallest readable displacement is the resolution. Final determinations are being made by the controls engineering team on the minimum step change to be applied.

1.3.3.2 Cross-Axis Response in X and Y (over full stroke)

In an ideal situation, the actuation of the Piezo crystal in the X axis (Figure 3) would move the Tx fiber solely in the X axis. Since this is not an ideal situation however, as the Piezo crystal actuates in the X axis, the Tx fiber will move in the Y axis as well as the X axis. This cross-axis response must be less than or equal to the specified value of 2μm.

1.3.3.3 Z-Axis response (over full stroke)

The Z axis response is the amount the stage moves in the Z axis during actuation in the X and Y axes. The Z axis is the axis normal to the X and Y axes seen in Figure 2. The fiber stage is not intended to move in the Z axis so the goal is to limit motion in that direction. A large displacement in the Z axis would take the stage out of focus with respect to the focusing lens. The focal length of the lens has some tolerance; therefore a small displacement is acceptable in the Tx fiber. Z-axis actuation is anticipated to be at a maximum when displacement in the X and

Y axes are also at a maximum. The requirement for Z-axis response is that it is less than or equal to 30 μm.

1.3.3.4 Allowable Tilt

The allowable tilt in both the X and Y direction is defined as the angular change about the respective axes. The allowable tilt is ±½^{o} about either axis. Although this is the required specification, there is some margin for error; it would be preferable that the stage did not tilt more than the requirement but it can function with greater tilt than the allowable ±½^{o}. Tilting too much means less of the energy goes along the desired path, which can result in clipping further down the optical path.

1.3.3.4 Temperature Survivability

The temperature requirements are twofold, survivability and operational. The survivability test ranges from -40°C to 70°C. This range is based on platformnon-operational requirements (storage requirements). Throughout this entire temperature range, the part cannot yield or lose its ability to operate. The NPS needs to survive multiple cycles between the minimum and maximum of the survivability range and remain operational.

1.3.3.5 Shock Input

The shock input requirement states that the NPS must survive a load of 20 g's for 25 milliseconds. The shock is in the form of a half-sine input as shown in Figure 4. Due to the high modal frequency of the NPS, for our simulation purposes the force can be simulated as a static load.

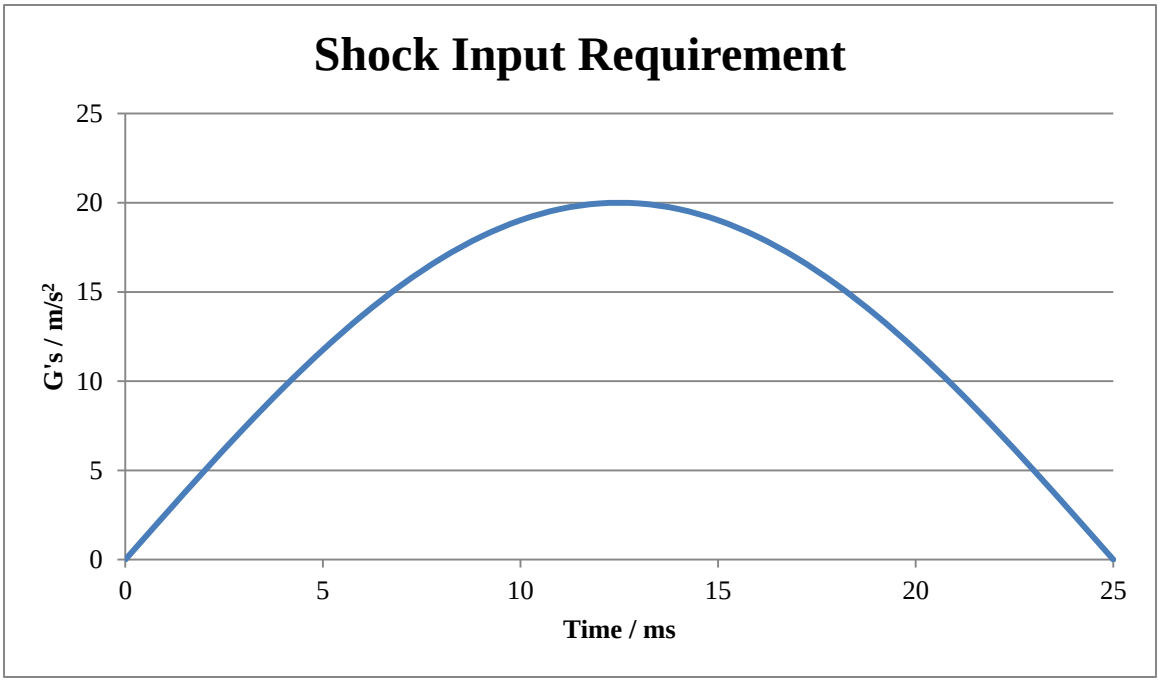

Figure 4: Shock input requirement of the NPS

1.4 Project Goals, Objectives and Methodology

The goal of this MQP is to assist in the development of a laser communication system at MIT LL. The objective is to analyze and test the current NPS design for functionality and survivability in order to meet the NPS's performance and environmental requirements. The analysis and testing process was used to model and characterize the abilities and limits of the NPS in an open-loop scenario. It was also used to determine the total stroke required and the open-loop accuracy budget for the NPS. In order to achieve the MQP goal and objectives, we followed approaches and methodologies as outlined below.

1. Simulate the NPS using finite element analysis.

Using advanced simulations through the finite element analysis (FEA) program in SolidWorks, called SolidWorks Simulation, the NPS was modeled through various performance, temperature and vibration conditions. The FEA results were used for the initial assessment for the NPS performance and environment requirements. They were also used as predictions for how the NPS would perform during physical testing.

2. *Design test fixtures and create test setups.*

In order to test the NPS under performance, thermal, and vibration conditions, various test fixtures needed to be designed. These designs take into account the time for fabrication, the importance of materials and their availability, as well as the test setup and the positioning of the NPS and its sensors. The test outline accounts for the NPS's requirements and time constraints of this MQP. The tests were run using the program LabView Signal Express and were designed to emulate the NPS's operating conditions.

3. *Characterize the NPS in relation to its performance and environmental requirements.*

The NPS was tested under room temperature conditions, at the thermal extremes as outlined in the environmental requirements, and through the operational temperature range. The NPS was tested to determine the total stroke requirements and the open-loop accuracy budget, as well as to confirm that the NPS met many of its other specifications. Error analysis was calculated and accounted for in all of our testing.

4. *Provide recommendations on the suitability of the chosen NPS design relative to its requirements.*

Upon completion of testing and analysis of the NPS, conclusions and recommendations were made and presented regarding the performance of the NPS, possible design improvements, and suggestions for future testing.

Chapter 2 – Finite Element Modeling and Analyses

Before physical testing, we performed finite element analysis (FEA) in order to evaluate the performance of the 12 mil flexure NPS and the 10 mil flexure NPS. Models will be verified later on using measured data. Modeling was conducted using the FEA program offered through SolidWorks, called SolidWorks Simulation.

FEA is used to determine how a component will react to certain conditions as a whole by discretizing the whole domain using finite elements. The FEA requires proper grid sizing in order to arrive at an accurate numerical solution. It is important that the size of the elements be chosen to reflect the precision of the results. Finer grids yield a more accurate result, but may require increased computational time (Cengel & Cimbala, 2009; Szabó & Babuška, 2011).

For our purposes, the finite element modeling and analyses were also used to compare the 12 mil flexure NPS to the 10 mil flexure NPS in order to characterize the differences in performance between the two flexure sizes. The refinement in the mesh was concentrated along the flexure joints since they are the areas that see the greatest stress, as shown in Figure 5 and Figure 6. The mesh density chosen provides good displacements results without sacrificing run times; a more refined mesh would be needed for detailed stress analysis. Using FEA, we were able to predict the NPS's performance with regards to total travel, cross-axis response, Z-axis response, thermal actuation, and modes of vibration.

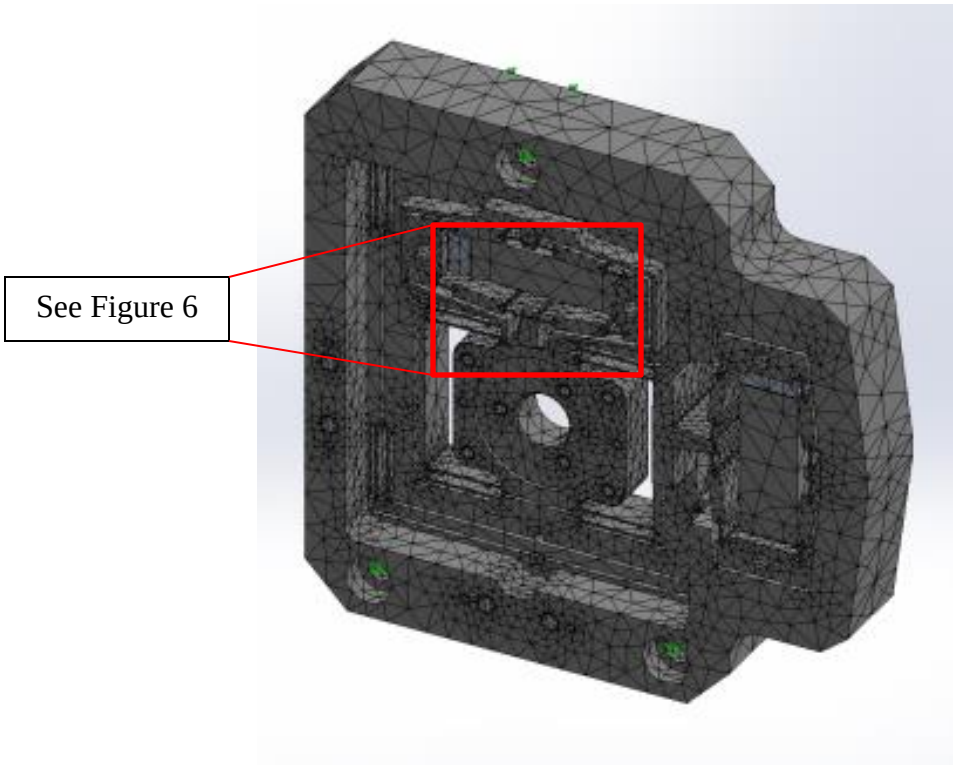

Figure 5: Mesh of the NPS concentrated along the flexures

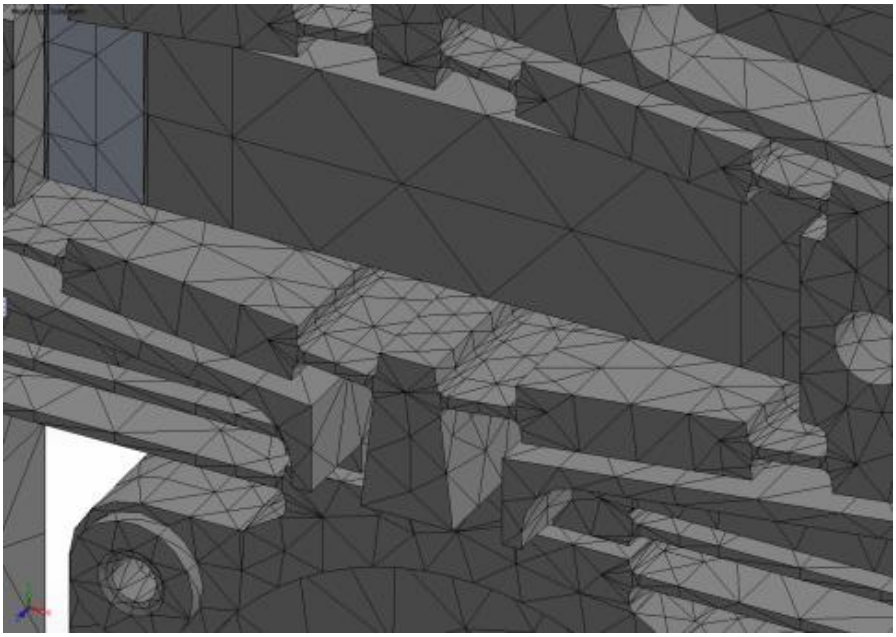

Figure 6: Close up view of Figure 5 with the mesh concentrated along the stage flexures

2.1 Room Temperature

The movement of the stage and the position of the transmission fiber are determined by the actuation of the Piezo crystals when they are stimulated by a voltage. Application of 100 volts to the crystals will cause them to displace 15 microns ±10%. It was not possible to model the crystal displacement through voltage stimulation, so we modeled the displacement in the crystals by a stimulation of temperature. Using Equation (2) and knowing the basic properties of the Piezo crystal, we determined the temperature needed to displace the crystal 15 microns. To stimulate the total travel over a full stroke, the minor crystal and the major crystal, as shown in Figure 7, were stimulated to their maximum displacement of 15 microns both individually and simultaneously.

$$\Delta L = L_{initial}\, \alpha\, \Delta \mathrm{T} \quad (2)$$

$\Delta L = change\ in\ length$

$L_{initial} = original\ lenghth$

$\alpha = coefficient\ of\ thermal\ expansion$

$\Delta T = change\ in\ temperature$

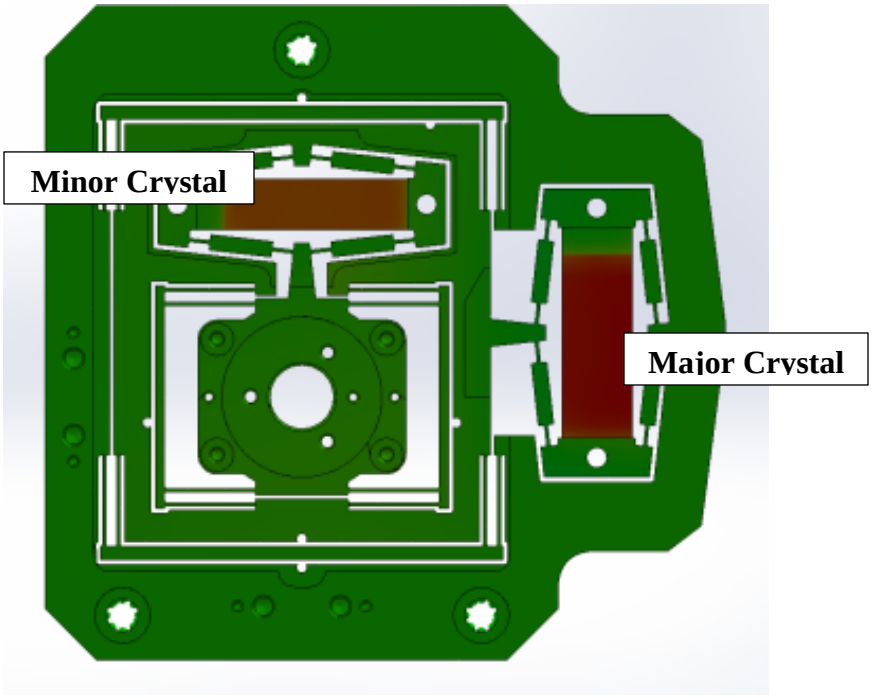

Figure 7: NPS with the Minor Crystal and the Major Crystal labeled

Along with the total travel, the cross-axis response and the Z axis response were also analyzed for the different scenarios. The results of the analyses of the 12 mil stage and the 10 mil stage can be seen in Table 5 and

Table 6, respectively.

Table 5: Displacement values for the NPS with 12 mil flexures

Minor Voltage	Major Voltage	X Travel	Y Travel	Cross-Axis Response	Z-Axis Response
0	100	109.650 µm		0.347 µm	0.224 µm
100	0		104.110 µm	0.306 µm	0.008 µm
100	100	109.350 µm	103.760 µm		0.232 µm

Table 6: Displacement values for the NPS with 10 mil flexures

Minor Voltage	Major Voltage	X Travel	Y Travel	Cross-Axis Response	Z-Axis Response
0	100	116.920 µm		0.310 µm	0.153 µm

100	0		112.800 µm	0.238 µm	0.001 µm
100	100	116.690 µm	112.490 µm		0.154 µm

The results of the analyses reveal a few of the unique features of the NPS. The first feature the analyses show is the asymmetry of the axes; the travel in the X axis is much larger than the travel in the Y axis. This feature is important to note for the control of the stage under operational conditions. The asymmetry means that a certain voltage applied to one crystal will not produce the same amount of displacement when applied to the other crystal. With regards to the accuracy budget and the stroke requirements, the requirements must be split to reflect the X and Y axes separately because of this asymmetry. The analyses also reveal the difference between the 12 mil and 10 mil flexure sizes of the stage. As was expected, the thinner flexures allow for a larger stroke in both the X and Y axes. The thinner flexure size also appears to minimize the cross-axis response and the Z axis response, though both are well below the requirements as given by the performance requirements. Data can be seen in Appendix B: Room Temperature Finite Element Analyses.

2.2 Thermal

The thermal testing of the NPS was modeled through its survival temperature range (-40°C to 70°C) and its operational temperature range (25°C to 35°C) to predict the amount of thermal actuation in the stage. Thermal actuation in the stage is caused by differences in the CTE of the materials in the NPS. The Piezo crystal is unusual in that it has a negative CTE in the polling direction, so its length decreases with increases in temperature. To make up for this negative CTE, the aluminum shims are used to normalize the CTE and match the CTE of the invar stage (Appendix A: Coefficient of Thermal Expansion Calculations). Though the aluminum shims are used to try and match the CTE of the invar stage, there is a small difference in the CTE's of the actuators and the stage. This difference is what causes actuation in the stage

over changes in temperature, and must be characterized to determine the total stroke needed in the stage, and the open-loop accuracy budget.

Heat transfer problems are commonly solved by finite difference or finite element analysis and modeling. “In the finite element approach, the temperature is assumed to vary over an element according to a simple polynomial relationship” (Doyle, Genberg, & Mechels, 2002, p. 16). As was seen with the modeling of the total travel, the thermal actuation of the NPS was greater in the X axis than in the Y axis over both the survival range (Figure 8) and the operational range (Figure 9). In Figure 8, the operational range is marked in green and the survival range is marked in red. The finite element analysis also showed that the actuation is linear in both axes.

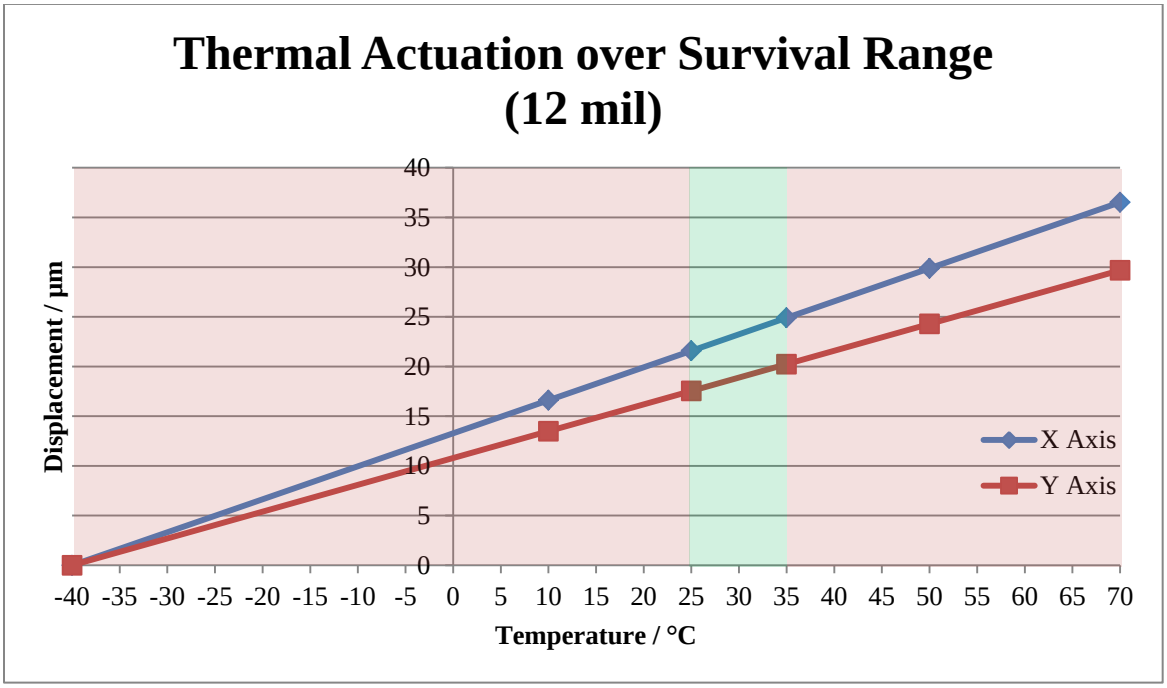

Figure 8: Graph of the thermal actuation of the NPS over the survival range of -40°C to 70°C for the 12 mil NPS design

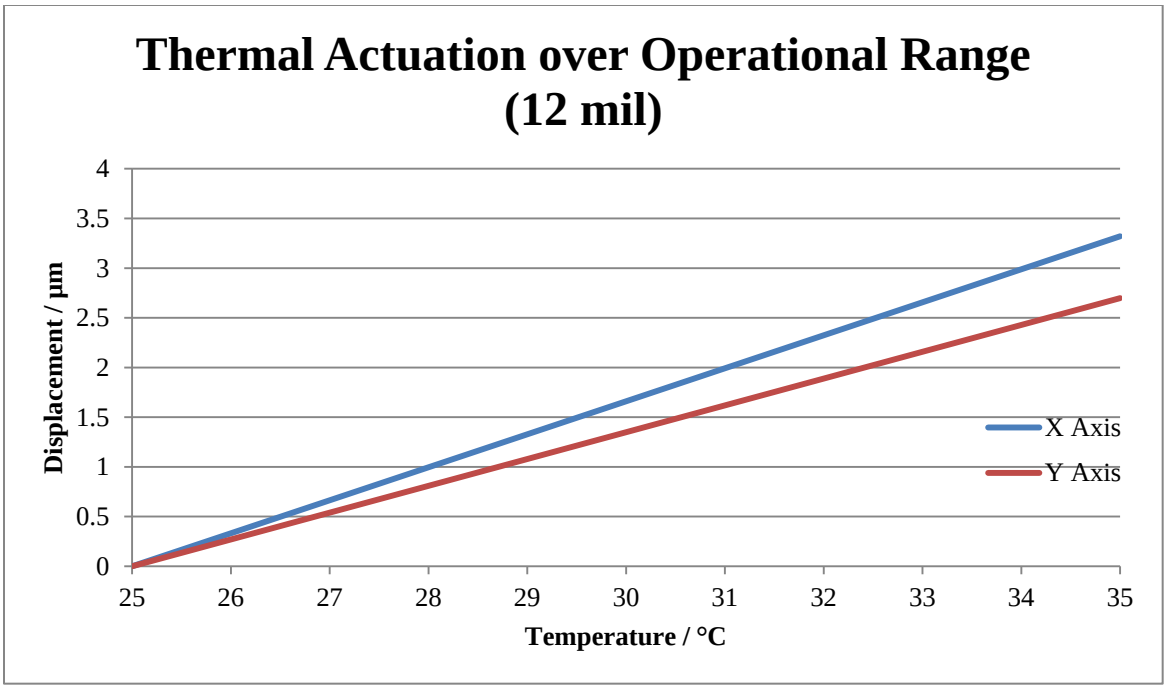

Figure 9: Graph of the thermal actuation of the NPS over the operational range of 25°C to 35°C for the 12 mil NPS design

From this model, we were able to predict the thermal actuation for the open-loop accuracy budget and the stroke requirements. Over 1°C, the thermal actuation was analyzed to be ± 0.17 microns in the X axis and ± 0.14 microns in the Y axis, shown in Table 7. Over the operational range of 10°C, the thermal actuation was analyzed to be ± 1.66 microns in the X axis and ± 1.35 microns in the Y axis, as shown in Table 8.

Table 7: Open-loop Accuracy Budget Thermal Actuation Modeling-12 mil Stage

Error source	Value (µm)	Comments
Thermal actuation	**± 0.17 (X)** **± 0.14 (Y)**	Over 1 °C change
Creep		Over 2 min acquisition
Thermal Drift		Over 1 °C change
Hysteresis		Max applied voltage of 9.4 V
Sub Total		Requirement of ±0.6 µm

Table 8: Total Stroke Requirements Thermal Actuation Modeling- 12 mil Stage

Contributor	Value (µm)	Comments
Point ahead	± 4.7	
Boresight stroke	± 7	
Steer off 1.5 pixels	± 8.4	
Alignment	± 25	Misc. mechanical
Thermal actuation	**± 1.66 (X)** **± 1.35 (Y)**	Due to -CTE of Piezo Crystal
Thermal drift	± 0.26	Due to stage mounting
System level thermal drift	± 10	Due to optics
Sub Total	**± 57.02 (X)** **± 56.71 (Y)**	Total stroke needed

With the stroke requirements, the modeled thermal actuation allowed us to predict the total stroke needed in the X axis and the Y axis. We predicted that the total stroke needed for the NPS is ± 57.02 microns (114.02 microns) in the X axis and ± 56.71 microns (113.42 microns) in the Y axis. Comparing this to the predicted total travel of the stage, shown in Table 9, we determined that the 12 mil NPS stage design will not meet its performance requirements with regards to total travel.

Table 9: Total Stroke Modeling-12 mil Stage

Axis	Predicted Travel (µm)	Stroke Needed (µm)
X	109.65	114.02
Y	104.11	113.42

After modeling the 12 mil NPS design, we modeled the 10 mil NPS design for thermal actuation to see if it too would nearly meets its performance requirements of total travel. As was

expected the 10 mil flexures cause the stage to actuate more in X and Y axes, though the difference in the actuation is relatively small over both the survival range, as shown in Figure 9,and the operational range, shown in Figure 10.

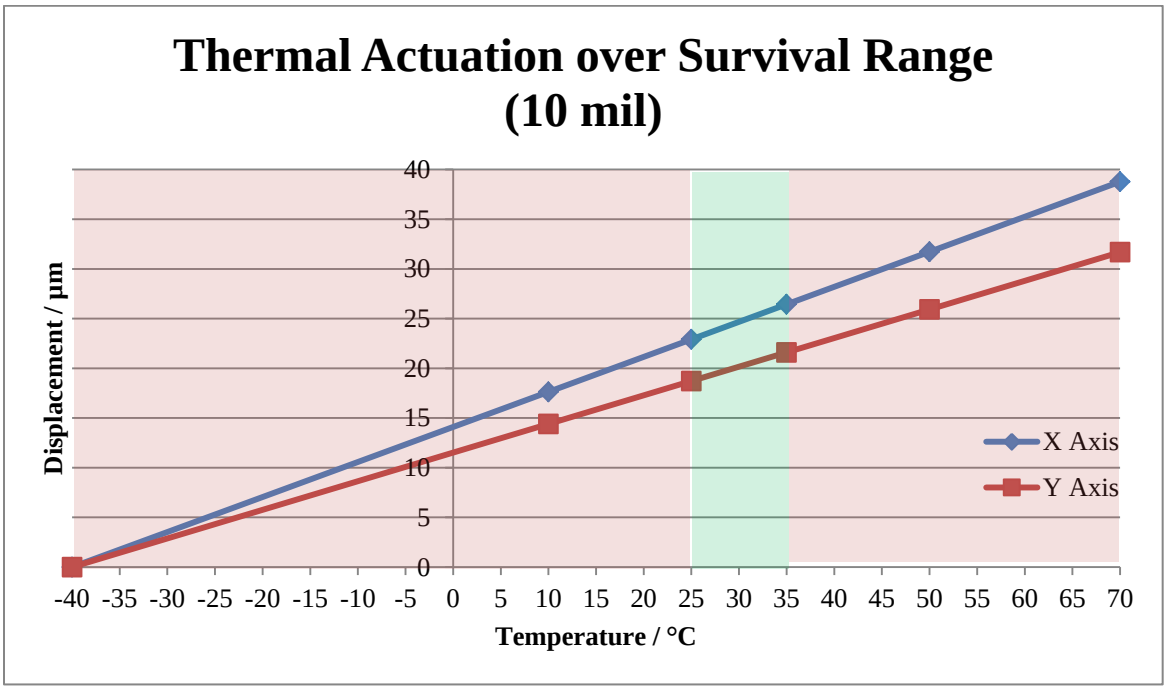

Figure 10: Projected Thermal Actuation over Survival Range-10 mil Stage

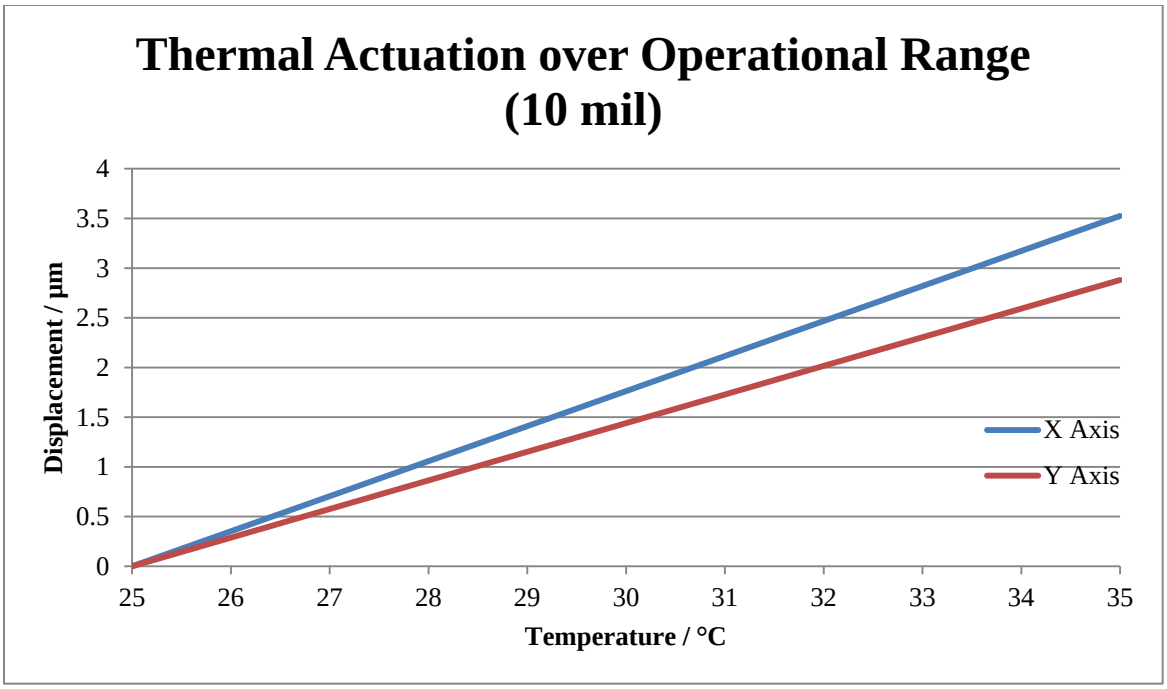

Figure 11: Projected Thermal Actuation over Operational Range-10 mil Stage

Over 1°C, the thermal actuation for the 10 mil NPS design was analyzed to be ± 0.18 microns in the X axis and ± 0.14 microns in the Y axis, as shown in Table 10, which is nearly the same as the 12 mil NPS design. Over the operational range of 10°C, the thermal actuation was analyzed to be ± 1.76 microns in the X axis and ± 1.44 microns in the Y axis shown in Table 11.

Table 10: Open-loop Accuracy Budget Thermal Actuation Modeling-10 mil Stage

Error source	Value (µm)	Comments
Thermal actuation	**± 0.18 (X)** **± 0.14 (Y)**	Over 1 °C change
Creep		Over 2 min acquisition
Thermal Drift		Over 1 °C change
Hysteresis		Max applied voltage of 9.4 V
Sub Total		Requirement of ±0.6 µm

Table 11: Total Stroke Requirements Thermal Actuation Modeling-10 mil Stage

Contributor	Value (µm)	Comments
Point head	± 4.7	
Boresight stroke	± 7	
Steer off 1.5 pixels	± 8.4	
Alignment	± 25	Misc. mechanical
Thermal actuation	**± 1.76 (X)** **± 1.44 (Y)**	**Due to –CTE of Piezo**
Thermal drift	± 0.26	Due to stage mounting
System level thermal drift	± 10	Due to optics
Sub Total	**± 57.12 (X)** **± 56.80 (Y)**	

With the stroke requirements, the modeled thermal actuation again allowed us to predict the total stroke needed in the X axis and the Y axis. We predicted that the total stroke needed for the 10 mil NPS design is ± 57.12 microns (114.24 microns) in the X axis and ± 56.71 microns (113.60 microns) in the Y axis. Comparing this to the predicted total travel of the stage, shown in Table 12, it was determined that the 10 mil NPS stage design is more likely to meet its performance. The Y axis is predicted to nearly miss the modeled stroke requirements while the X axis is predicted to pass the modeled stroke requirements.

Table 12: Total Stroke Modeling-10 mil Stage

Axis	Predicted Travel (µm)	Stroke Needed (µm)
X	116.92	114.24
Y	112.80	113.60

2.3 Vibration

Analysis was also considered to find the different modes for the 10 mil and 12 mil NPS designs. As can be seen in Table 13, the first mode of natural frequency occurs at 506.65 Hz for the 10 mil stage, and at 540.46 for the 12 mil stage. A visualization of the first 10 modes of frequency for both stage designs, along with the maximum displacements at these nodes, can be found in Appendix C: Vibration modal models for the 10 mil and 12 mil NPS Designs. These values are much greater than the shock frequency of 20 Hz, as was given by the environmental specifications, so it is determined that the shock will not excite the natural frequency of the NPS. This means that when the shock analysis is considered, only the acceleration of 20 G's will be a factoring component.

Table 13: Modes of natural frequency for the 10 mil and 12 mil NPS designs

Mode Number	Frequency 10 mil (Hertz)	Frequency 12 mil (Hertz)
1	506.65	540.46
2	717.32	771.06
3	999.94	1145
4	1064.8	1239.2
5	1226.1	1290.5
6	1237.7	1325.1
7	1459.3	1563.7
8	1467.8	1649.6
9	1480.9	1707.9
10	1548.6	1792.8

Chapter 3 – Designs for NPS Test Fixtures

In order to test the stage effectively, fixtures need to be developed to hold the NPS stably and effectively. It must allow for the NPS to move freely throughout its range of motion, not cause stresses that would not be seen in operation and have enough mass to be unaffected by changes in environment. Such testing fixtures are not available for purchase from vendors and have to be custom made for testing under three different environments: room temperature, thermal variations, and vibration. This chapter presents the design and fabrication of these fixtures for each of these three environmental tests.

3.1 Testing Features

In order to take displacement measurements, a target assembly was designed. The target assembly took the place of the fiber ferule holder during testing displaced in the X and Y axes simulating the displacement of the fiber. The target assembly is made of two different parts, the target blades and target ring. The target ring is made of invar to maintain the same thermal properties of the NPS. It is a circular design with a hole in the middle to mount around the fiber ferrule head. Clearance holes are in a triangular pattern to match up with the tapped holes on the NPS. The holes are sized for #0 screws. Two relief cuts are placed on the target ring to attach the target blades to the target ring. The relief cuts are placed so that target blades are perpendicular to the walls of the NPS. This is the proper orientation for the Kaman sensors to read displacement in the X and Y axes.

The target blade was designed based upon the recommendations from Kaman for the sensors. An aluminum target blade is necessary for the Kaman sensors to read displacement. Aluminum is also recommended by Kaman. The characteristics of aluminum allow for the

maximum accuracy of the Kaman sensors. The target blade is attached to the target ring using an epoxy.

Also in the test setup, spiral compressions springs were used to keep the actuators in compression. These springs will not be used in the final designs of the NPS due to the fact that they are too bulky and do not fit into the housing of the NPS. While the final springs were being designed and manufactured, these springs were used due to the fact that they were readily accessible. The springs also have nearly the same spring constants as the springs that are to be designed. Figure 12 shows the NPS as it was set up for testing. As can be seen, the Kaman sensor on the bottom of the NPS measures the displacement of the target blade in the X axis as the Piezo crystals are actuated.

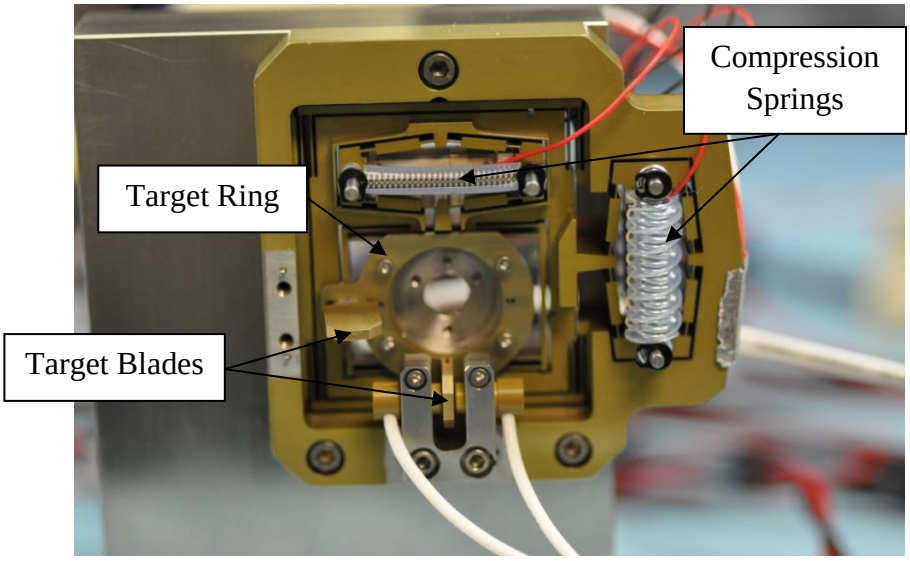

Figure 12: NPS setup for testing

3.2 Room Temperature Test Fixture

The first set of tests for the NPS are conducted at room temperature. Due to time limitations, a simple fixture design was pursued. The fixture is required to support the NPS as well as the displacement sensors. The fixture was designed of Aluminum Alloy 6061-T6, a material readily available in most machine shops. The material properties of Aluminum 6061-T6

provide needed stiffness to hold the weight of the NPS and the displacement sensors. Thermal properties were not considered for the design of this test fixture due to the fact that the testing would be completed at room temperature under negligible fluctuations of temperature.

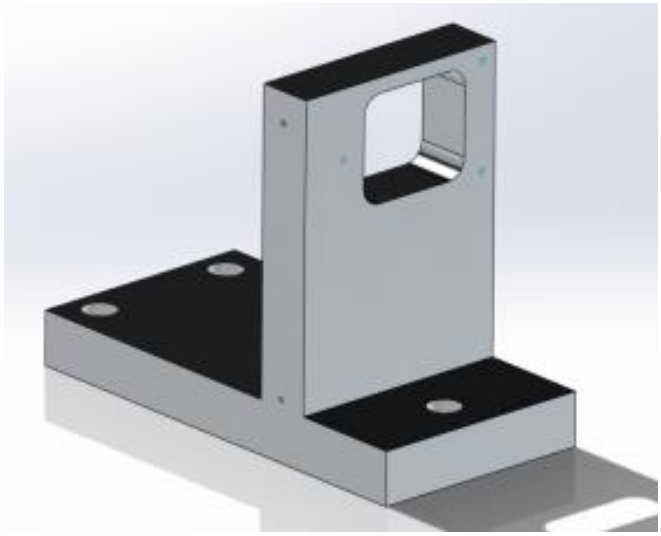

Figure 13: Room Temperature Test Fixture

After several design iterations, a "T" shaped fixture was conceived and the drawing is shown in Figure 13. The fixture is designed to be attached to an optics bench for optimal stability with three counter bore holes in the base to support ¼-20 screws. These holes match the 1 X 1 inch grid pattern of the optics bench. The part that protrudes from the base is designed to hold the NPS in its upright form as shown in Figure 14. The NPS was to be tested vertically in order to better simulate its operating conditions.

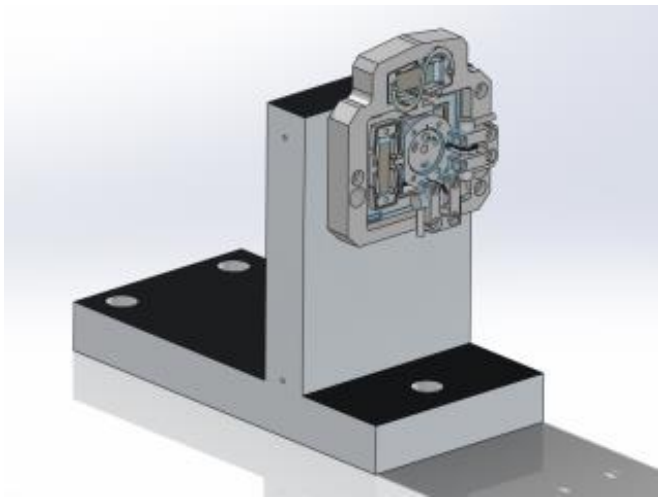

Figure 14: Room Temperature Test Fixture with attached NPS

The NPS was held in place with three #4-40 screws, just as it would under operating conditions. The carved window in the middle of the fixture is designed to compensate for the size of the fiber ferrule holder in the NPS, as well as for the protrusion of interior springs around the crystals. The window provides enough clearance so that the springs do not slide against the fixture and also allows testers to see the motion of the fiber ferrule holder during testing. A fillet radius of 0.25 inches is added to the design of the window to make it easy and fast to fabricate. On the side of the test fixture, two tapped holes are placed for #2-56 screws to attach the sensor clip for the NPS.

The final design consideration for the Room Temperature Test Fixture was to ensure that the NPS and its sensors had enough clearance from the base of the fixture. This was done by ensuring that all of the tapped holes were high enough for the necessary clearance.

3.3 Thermal Test Fixture

Because the testing under thermal conditions needed to closely replicate room temperature tests, the Thermal Test Fixture was designed to nearly match the Room Temperature Test Fixture. The material used for the thermal fixture is annealed Invar 36 to match the material

used for the NPS and its thermal properties. This ensures that there were no unnecessary stresses or displacements in the NPS, and that the fixture and the NPS expanded and contracted similarly over large temperature fluctuations. Springs and flexures were initially considered to allow the NPS to expand freely with minimal stresses and displacements, but both were rejected due to the fact that it would take more time to design and manufacture for relatively small gains in results. Springs may have also caused unintended consequences. They may have solved the thermal actuation issue but caused other problems along the way.

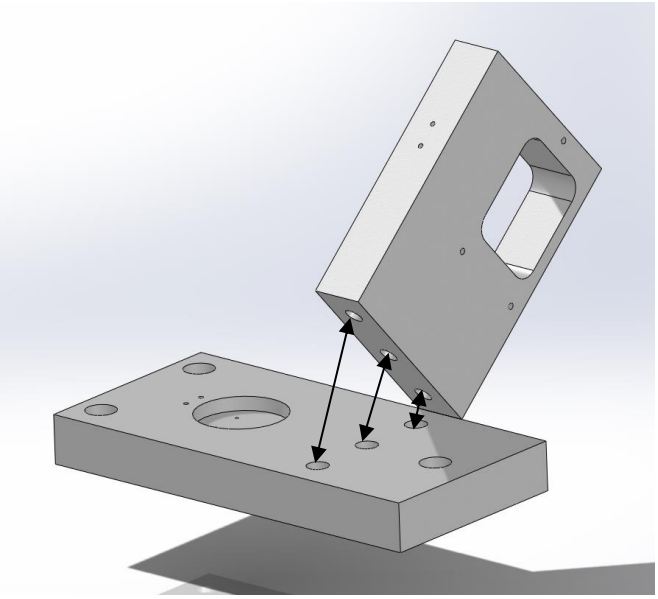

Figure 15: Thermal Test Fixture

The Invar Thermal Test Fixture shown in Figure 15 was designed in two pieces instead of one to mitigate the cost of manufacturing. The base and the stage holder are fitted together with three 5/16-18 screws as seen in Figure 15. Unlike the Room Temperature Test Fixture, the Thermal Test Fixture also took into consideration testing for thermal sensor drift. The decision was made to combine these fixtures to save time in manufacturing as well as the cost of supplies. In this test, the sensors will be characterized to determine if any displacement is measured due to temperature change when no displacement occurs. This test will be conducted by taking the

sensors off of the stage and attaching them directly to the test fixture. Any thermal sensor drift will have to be taken into account during further testing. On the base, a circle was milled out and screw holes were drilled to attach the Kaman sensors to the fixture as well as the target blades. The displacement of the target blades is what is measured by the Kaman sensors. The brackets for the Kaman sensors as well as the target ring are constructed of Invar. This negates any changes due to thermal expansion. The target blades are made of aluminum, which is the manufacturer specified material due to its electrical conductivity and its nonmagnetic properties.

Inside the milled out circle, a relief gap was placed under where the target blade will be located. The target blades are attached to the target with an adhesive. The relief gap underneath will give room for margin during the adhesive application. Without the relief gap, excess adhesive may cause the target assembly to not lay flat on the fixture and could cause extra stresses. It is important for the assembly to be flat on the test fixture to ensure accurate results from the Kaman sensors. Drawings can be found in Appendix D: Test Fixture Drawings.

3.4 Vibration Test Fixture.

Since vibration testing is to be conducted at room temperature, the Vibration Test Fixture is designed of Aluminum Alloy 6061-T6 because of its availability and its suitable mechanical properties relating to vibration stability. At MIT LL, vibration tests are performed on different sized blocks depending on the size of the test piece. The blocks have a 2 X 2 inch grid pattern of 5/16 inch tapped holes. The Vibration Test Fixture shown in Figure 16 is needed in order to attach the NPS to this grid pattern. The design is as symmetrical as possible in order to eliminate any inertial anomalies in the fixture during the vibration. This symmetry effectively allows us to use the NPS through different vibration specifications as if it were directly attached to the

vibration block. This also allows us to test the Rcv fiber stage on the same test fixture. This will save time for other teams working on the Rcv fiber stage in the future.

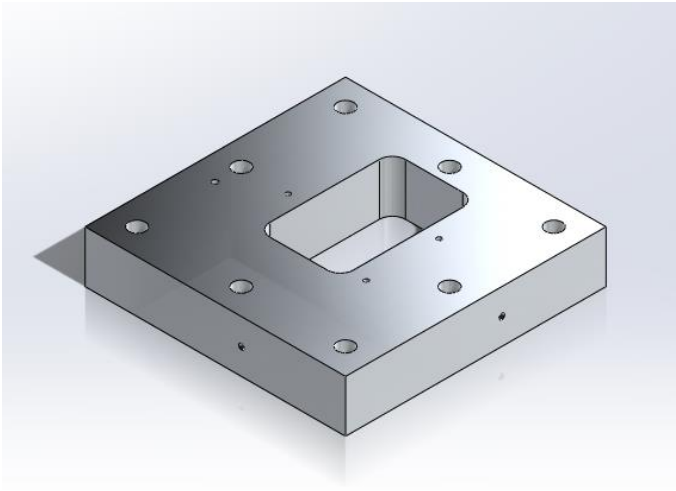

Figure 16: Vibration Test Fixture

The test fixture is designed as a 5 X 5 inch block with nine 5/16 inch clearance holes placed on a 4 x 4 inch square. Similar to the other test fixtures, a tapped-hole pattern is used that corresponds with the clearance holes of the NPS, as well as a clearance window to allow the NPS to sit without any interference.

Unlike the other two fixtures, the Vibration Test Fixture had #6 tapped screw holes placed on each of its four sides to fix the accelerometers used for testing. The accelerometers are placed so that data could be acquired on multiple axes while only using uniaxial accelerometers. The accelerometers can be placed on five faces of the fixture to provide extra data points. Having two accelerometers for each axis allows for more data points to achieve more accurate data. A #6 tapped hole was placed on the top face of the fixture to measure the third axis.

While designing the vibration fixture, we had to take into consideration the center of gravity and moment of inertia of the NPS. During vibration testing, the optic head, as well as the fiber ferrule holder, are not attached to our test stage. In vibration testing, it is extremely important to make sure that the center of gravity and moment of inertia of the piece being tested

is the same as the actual piece. In order to make up for the loss of mass from the optic head and fiber ferrule holder, a circular mass is designed to be placed on the NPS during the vibration test. Using the 'mass properties' feature of SolidWorks, the center of mass can be calculated with the replacement mass to ensure that it was the same as it would be under operating conditions. The piece has three #55 clearance holes to fit the pattern and size of the tapped holes on the NPS. The drawings can be found in Appendix D: Test Fixture Drawings.

Chapter 4 – Experimentation and Data Analysis

Experimentation was completed to acquire measured data that can be compared to models. Testing procedures and data analysis are presented in this chapter. Testing was completed at room temperature and a temperature range of -40°C to 70°C. The room temperature tests were completed in an ESD-Safe lab and the tests with temperature variations were completed in the environmental testing lab.

4.1 Testing Setup

This section details the test setup for our experimentation. It includes the details of the software used and the hardware. A detailed explanation of the displacement sensors used is also featured.

4.1.1 Software

LabView Signal Express was chosen as the program to write the virtual instruments (VI) needed for our test. A virtual instrument is the programming needed to connect the computer to the hardware needed for testing; it allows users to create measurement systems. Both the hardware and the software must be in sync to have a successful test. The program gives us the ability to read all of our sensors, as well as control the power supply being used.

LabView Signal Express comes with pre-written functions that can be used to generate the voltage output necessary for each test. With relative ease, step functions and sine functions can be created and implemented. The DAQ Assistant functions give the user the ability to adjust the sampling rate of the experiment, as well as the frequency in which samples are taken. It also gave us the ability to use a low-pass filter in order to remove some of the noise from the sensors. Filters were used for each channel which greatly increased the accuracy of the data acquired.

The decision was made to use this program due to its simple user interface and minimal programming required to begin data acquisition and signal analysis.

4.1.2 Hardware

The LabView Signal Express VI is the software end of the testing. The VI controls the multifunction data acquisition card located in the computer. The card used for our testing was the National Instruments (NI) PCI-6259 card. It is produced by National Instruments with a 16 bit analog to digital converter and the ability to handle 32 analog inputs and 4 analog outputs. The analog outputs have a range of ± 10 V.

The NI PCI-6259 card needs to connect to a breakout board in order to be wired into the system. The breakout board used for our testing was an SCB 68. Each breakout board is able to take 16 analog inputs and 2 analog outputs.

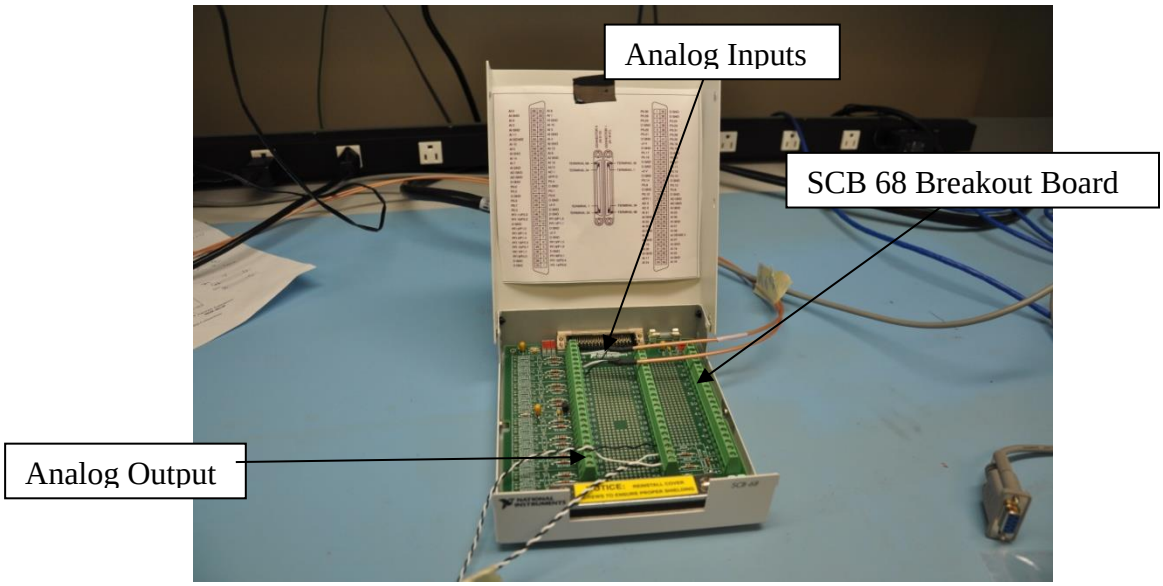

Figure 17: SCB 68 Breakout Board

For our testing, a voltage output of 100 V was necessary to drive the NPS. Since the NI PCI-6259 card was only able to output ±10 V, an amplifier was used to achieve the full voltage

range. It amplified the voltage by a magnitude of 10. This was the most effective way to achieve our full voltage range with the tools at hand.

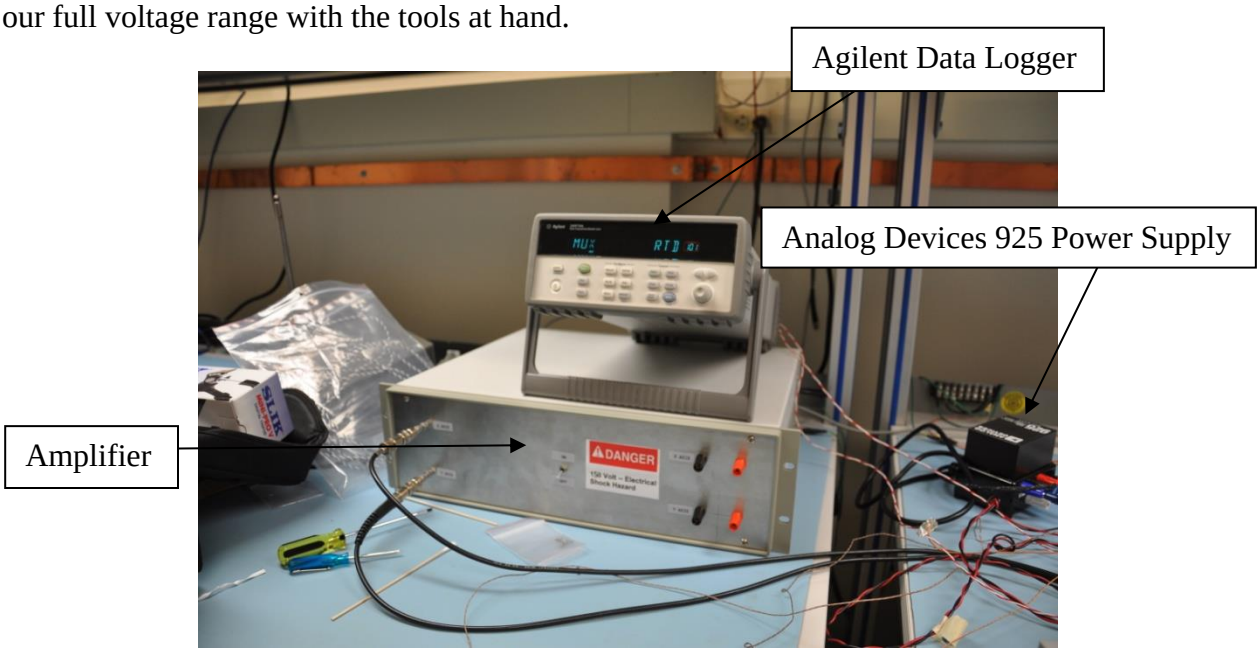

Figure 18: Amplifier, Data Logger and Sensor Power Supply

The amplifier used was custom made at MIT LL and was designed specifically for the needs of this project. The amplifier had two different inputs and outputs which gave us the ability to control both axes with different voltage outputs. Issues arose with the computer timing creating a slight delay in one of the axes. In order to mitigate this issue, the two axes were wired in parallel to only one output of the amplifier. This ensured that they both received a voltage output at the same time. Unfortunately, by doing this it forced both axes to receive the exact same voltage unless one was physically disconnected from the circuit.

In order to read the displacements, Kaman KD5100 sensors were employed. These are eddy-current sensors that are described in detail later in this chapter. They are extremely accurate sensors with nanometer resolution.

In order to collect all the necessary data, both hardware and software were required for the testing set up. For our data to truly be meaningful, other parameters were to be taken into

account. The main issues to be resolved were quantifying small temperature changes in the room, as well as isolating the NPS from the vibrations of the room.

Optimally, an air table would be used to dampen vibrations within a lab environment. Unfortunately, our team was unable to acquire an air table for testing. Instead, a foam block was used to dampen the vibrations. The entire fixture and stage was placed upon the foam block to isolate vibrations. This proved to be successful as vibrations were determined to be an extremely minimal source of error.

Unlike vibrations, there was no practical method with the time constraints to eliminate small temperature fluctuations in the room. Temperature readings of the important pieces of our experiment were recorded in order to determine if there was any correlation. A repeatable pattern could be accounted for in our data.

There were several points that were considered important for temperature measurement. The temperature of the invar, the KD 5100 box and the air temperature were all carefully monitored and recorded. Resistance temperature detectors (RTD) were used to measure the temperature. An RTD is a temperature measuring device that relies upon changes in resistance to determine the temperature. The data set for the particular RTD used in this experiment can be found in Appendix F: RTD Specification Sheet. There are several different kinds of RTDs and generic two-wire platinum RTDs were chosen for our experiments that are inexpensive and accurate to within ±0.1 °C (See **Error! Reference source not found.** for more information). To nsure the RTD remained attached to the surface it was measuring, 3M aluminum foil tape was used. The data sheet for the specific tape used can be found in Appendix G: 3M Aluminum Foil Tape Specification Sheet.

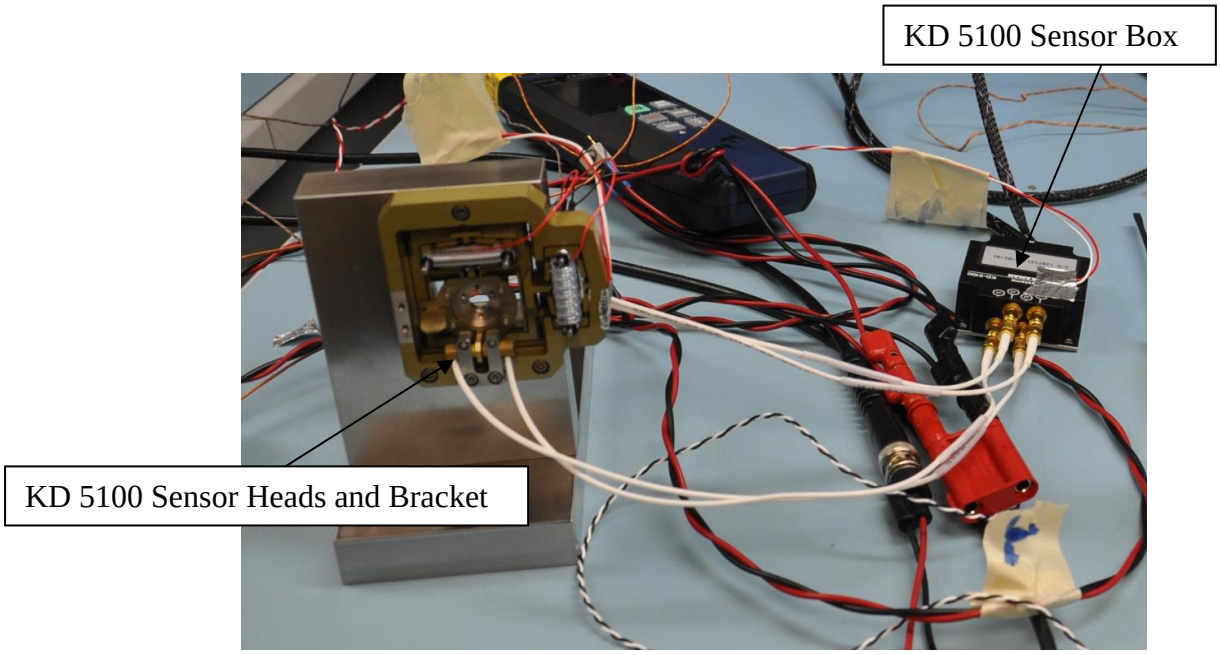

Figure 19: Sensors and NPS

Instead of using LabView Signal Express, Agilent Benchlink 3 software was used to record temperature data. In conjunction with an Agilent Data Logger, the software was extremely user friendly and easy to program. The driving factor in our decision to use Agilent over LabView was the PCI-6259 cards inability to generate a constant drive current. In order to read an RTD, a constant current is necessary. The Agilent Data Logger was able to provide a constant current source, as well as read the RTD by programming in the type of RTD being used. The Agilent Data Logger is preprogrammed with calibrations for different common RTDs.

A shortcoming with using multiple programs was that start times tended to vary by a small amount. In order to compensate for this, the system clock was used to determine the absolute start time of both our displacement data and temperature data. An offset was then used to ensure that all sets of data started at the same time.

This same setup was brought over into the thermal chamber to complete thermal testing. The thermal chamber used was a Thermotron. It gave us the ability to create simple temperature profiles. The program broke the profile up into stages. The options were a dwell period or a

linear change in temperature. From here, choices could be made in the temperature of the stage, how long the dwell period would be or the ramp rate in degrees Celsius per minute. It could easily be programmed on the fly and a feature to hold the temperature constant at any point during a profile was also available. The thermal chamber and computer setup can be seen in Figure 20.

Figure 20: Temperature Test Setup

The major issues with the thermal chamber were again vibrations and the fans in the chamber that would be running during testing. The vibrations were dampened using foam and the fans were considered an acceptable form of error. Shutting off the machine in the middle of a profile was considered to complete testing but was decided against due to the unnecessary strain put on the compressors by turning them on and off.

The laboratory setups used for testing proved to be effective throughout the course of testing. Many of the critical path issues were solved early on in the process and our set up minimized environmental and hardware errors.

4.1.3 Kaman Eddy-Current Sensors

Kaman eddy-current sensors are used to measure displacement of the Nano-Positioning Stage. These sensors were chosen due to their high long term stability and accuracy on the nanometer scale. Eddy-current sensors in general work by sensing the strength of eddy currents in a conductive target that are induced by a rapidly changing magnetic field produced at the probe's tip. The result is an analog voltage proportional to gap width.

The sensors arrangement was differential, requiring two sensor heads with a target placed in between them. The target is made out of aluminum due to the fact that it is nonmagnetic as well as electrically conductive. When the sensor moves, it must only move in the axis that would displace the target closer to one sensor and equally farther from the other. Inside the sensor heads are coils that are energized by an AC power source. This creates a magnetic coupling between the target and the sensor head. When the target and sensor head are close together, they have a stronger magnetic coupling than when they are far apart. The difference between the voltages created by the two sensor heads is what is seen by the data acquisition system. In the null position, the target is directly in between the two sensor heads and 0 volts should be read from the sensors.

For this application, the sensors are not in the null position when 0 V are applied to both of the Piezo crystals. This is due to the limit of the maximum voltage that can be created by the sensors which is ±10 V. If the null position was at 0 V through the Piezo crystals, the sensors would no longer be accurate in the projected further ranges of total travel. The null position was chosen to be at 60 V as this is the projected midpoint for the total travel. This allows the Kaman sensors a 10 V swing in either direction to accurately measure the total travel of the optic head.

Kaman eddy-current sensors are almost exclusively used when high accuracy is a necessity. For this reason, the manufacturer sends out specific data sheets for each sensor that allows the user to relate the voltage seen from the sensors to be directly related to displacement. In the Y axis, our sensor was rated at 0.1255 V/μm. In the X axis, our sensor was rated at 0.1253 V/μm. The calibration sheet for the Kaman sensors used can be found in Appendix H: Kaman Kd5100 Calibration Sheets. This is an extremely important distinction due to the extremely tight accuracy budget of this project, as well as many others that use Kaman eddy-current sensors.

4.2 Room Temperature Tests

Experiments were performed using the Room Temperature Test Fixture in an open air lab environment. This setup was used to conduct a series of specific tests to determine whether the stage meets requirements of the project sponsor and to provide recommendations in cases of failed tests. The room temperature analyses were conducted with the following tests: sensor drift; total travel; voltage vs. displacement; creep; hysteresis and resolution. All tests were conducted using the same setup. Temperature variation was recorded and was in an acceptable range of plus or minus one degree Celsius.

4.2.1 Sensor Drift

Characterization of the eddy-current sensors used for the NPS is the first step in being able to understand all further data about the NPS. With the extremely tight open-loop accuracy budget, it is important to be able to verify the manufacturer's data sheet. Kaman provided individual data sheets for each sensor with calibration information. In order to provide a coarse verification of the data sheet calibration, a displacement was induced in the stage and measurements were taken from the eddy-current sensors, while a dial indicator provided an independent verification of displacement to the level of tenths of mils (~2.5 microns).

Kaman states that the long term stability of the sensors is 5 x 10^{-6} inches per month and does not quantify short term stability. Any repeatable short term drift in the sensors output needs to be taken into account when analyzing further data.

The way this test was set up was by attaching one of the sensors to an invar testing fixture. Invar was chosen due to the fact that it was the same material as the sensor bracket and would reduce any effects of temperature actuation. An aluminum target blade was set up to give the Kaman sensors the reference they needed. RTD temperature sensors were attached using epoxy and aluminum tape to the sensor bracket itself as well as the Kaman 5100 box. These are extremely important to have in case any sensor drift was directly related to unexpected temperature changes in the room. The test was run for a one hour period.

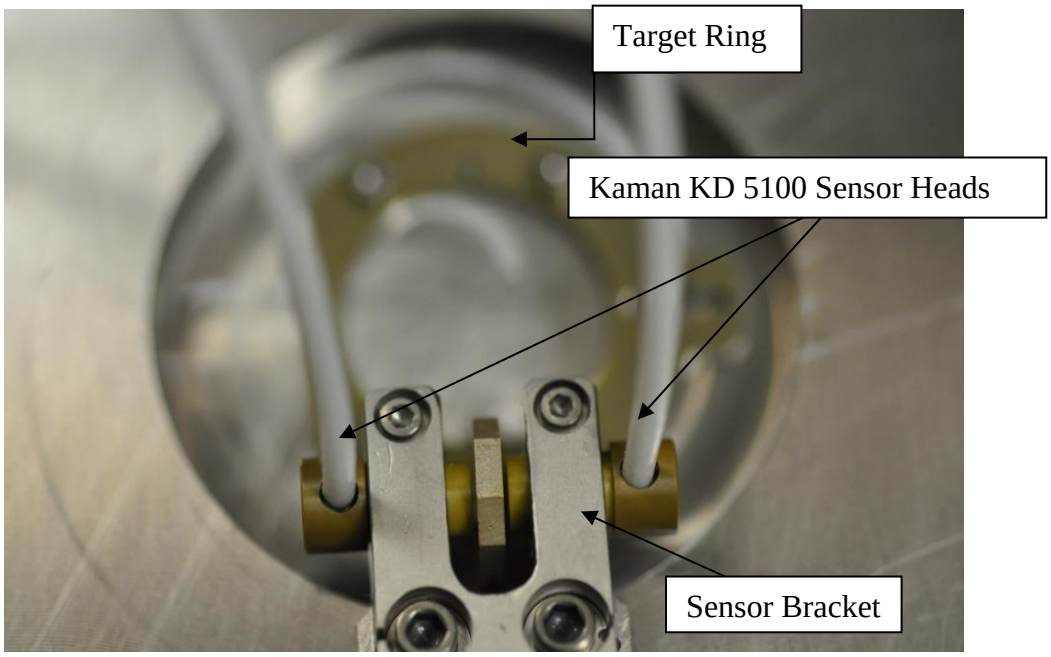

Figure 21: Sensor Drift Test Setup

Sensor drift could not be directly correlated to time. The data shows a correlation between the temperatures of the Invar stage and the sensor output (Figure 22).

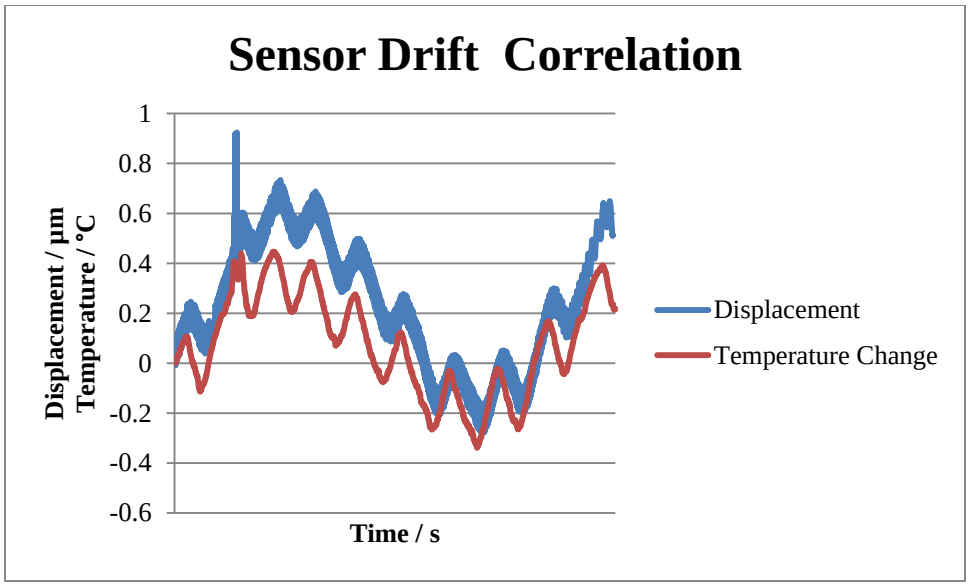

Figure 22: Sensor Drift Correlation

Further work is completed in this MQP that analyzes that correlation between temperature and the displacement output of the sensors.

4.2.2 Creep

The characteristics of the creep associated with the NPS in the X and Y directions were first analyzed. Creep is an observable phenomenon in Piezo Crystals (Physik Instrumente, 2008) that occurs when a set voltage is maintained for an extended period of time. As the voltage is changed from one set point to another, the crystal will continue to move in the same direction as the applied voltage with a linear displacement on a log scale as shown in Equation (3). This creep is a predetermined function for the Piezo Crystals and is defined by:

$$\Delta L\,(t, v) = \Delta L_{t=0.1}\left(1 + \gamma(v)\log\left(\frac{t}{0.1}\right)\right) \quad (3)$$

$\Delta L\,(t, v)$ = displacement *t* seconds after the change in voltage is complete to voltage "v"

γ = percent creep factor of the Piezo crystal (on the order of 1% to 2%)

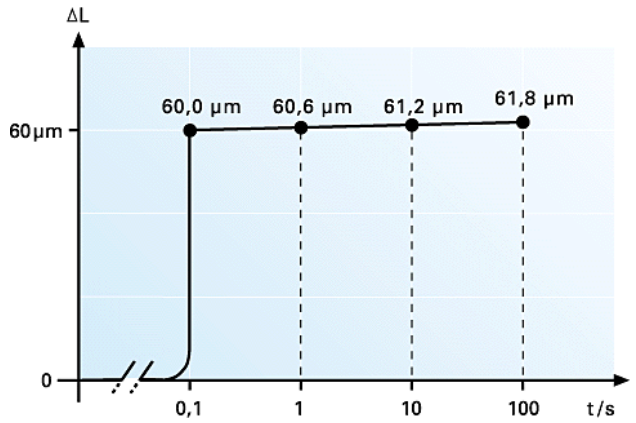

Figure 23: Piezo Creep (Physik Instrumente, 2008, p. 2-186)

As can be seen in Figure 23, the initial time value for the creep occurs 0.1 seconds after the change in voltage is complete. While this information may be true for the Piezo Crystals, it does not pertain to our results since our measurements are conducted around the placement of the transmission fiber. The transmission fiber had not reached its commanded position by 0.1 seconds after the voltage was applied. In order to determine the initial time value for our results, we determined the point at which the linear creep function began, shown in Figure 24, for voltages from 0 to 100 in increments of 10 volts. An example can be found in

Appendix J: **Creep Graphs**. As can be seen in the data, the initial time value does not occur exactly at the value of 0.1 seconds. Equation (4) is rewritten as:

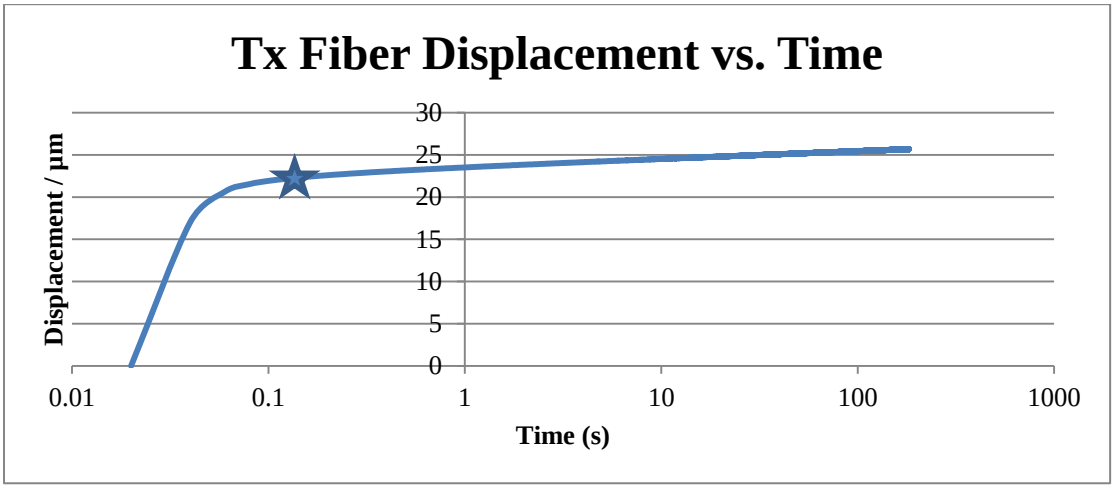

Figure 24: Tx Fiber Creep

$$\Delta L\ (t, v) = \ \Delta L_{t=start}\left(1 + \gamma(v)\log\left(\frac{t}{start}\right)\right) (4)$$

Using Signal Express, the creep was determined for voltages from 0 to 100 in increments of 10 V over an acquisition time of 2 minutes. For the NPS, 2 minutes is the maximum open loop period. The percent creep factor and the creep itself provided by Equation (5) were determined for each voltage in

Appendix K: Creep **Charts**

$$creep = \Delta L\ (120 + start) - \ \Delta L_{t=start}\ (5)$$

The creep value for the open-loop accuracy budget is taken over the voltage of 9.4 volts. It is estimated 0.4 volts is the greatest voltage difference to maintain point ahead during the acquisition period. The creep value is found by interpolating the data to solve for the creep at 9.4 volts.

By using the above Equations (4) and (5) as they pertain to the data, the creep is found with an applied voltage of 9.4 volts after two minutes. When the voltage is applied only in the X axis, the transmission fiber creeps 261 nm with a percent creep of 1.30%. When the voltage is applied only in the Y axis, the transmission fiber creeps 251 nm with a percent creep of 1.32%. When the voltage is applied in both axes, the transmission fiber creeps 262 nm in the X axis direction with a percent creep of 1.38% and 218 nm in the Y axis direction with a percent creep of 1.38%. Test data from each voltage step of the creep tests can be found in

Appendix K: Creep **Charts**

From this model, we were able to predict the maximum creep for the open-loop accuracy as shown in Table 14. Over a 2 minute acquisition period creep was measured to be ± 0.13 microns in each axis.

Table 14: Open-loop Accuracy Budget Creep-12 mil Stage

Error source	Value (µm)	Comments
Thermal actuation		Over 1 °C change
Creep	**± 0.13**	Over 2 min acquisition
Thermal Drift	TBD	Over 1 °C change
Hysteresis		Max applied voltage of 9.4 V
Sub Total		Requirement of ±0.6 µm

4.2.3 Total Travel

By evaluating the creep, the total travel can be accurately determined by finding the initial start values of voltages ranging from 0 to 100 volts. The total travel for the Tx fiber is determined by stimulating the voltage to the Piezo crystals from 0 to 100 volts in steps of 10 volts for a minimum of 2 seconds. Voltage is applied to the X axis while the Y axis is unloaded, to the Y axis while the X axis is unloaded, and to both axes simultaneously. By measuring both axes simultaneously, we are able to determine cross-axis response.

Due to large differences between filtered and unfiltered data near the initial start value, the data for the total travel is acquired 1 second after the change in voltage were complete for each test. In order to use this data to find the true values for the total travel, Equation (6) is used to provide $\Delta L_{t=start}$.

$$\Delta L_{t=start} = \Delta L\ (1) - \ \Delta L_{t=0.1}\left(\gamma \log\left(\frac{1}{start}\right)\right) (6)$$

Using Equation (6) above, creep was minimized when determining total travel. It gave us the ability to take the creep out of the data and get a true sense of where the total travel ended and where the creep began. This is important because the elongation due to creep was not to be considered for the total travel results.

The total travel in both the X and Y is determined, loaded and unloaded, as well as the cross-axis response are shown in Table 15. The variation of displacement with voltage is also determined and shown in Appendix I: Room Temperature Hysteresis Data. Unlike our previous assumptions, it was determined that the variance follows the path of a third degree polynomial

rather than that of a straight line. This was expected as the PI literature shows a third degree polynomial for the elongation of the crystal.

Table 15: Total Travel Results-12 mil Stage

X Voltage	Y Voltage	X Travel	Y Travel	Cross-Axis Response
0	100		101.036 µm	0.485 µm
100	0	111.451 µm		0.739 µm
100	100	110.43 µm	100.41 µm	

4.2.4 Hysteresis

Like creep, hysteresis is an observable phenomenon in open-loop operation and is based on crystalline polarization effects and molecular effects within the Piezo Crystals (Physik Instrumente, 2008). Also in a similar fashion to the creep, the hysteresis that we measured is reflective of the movement of the transmission fiber, not the Piezo crystals, though it is directly caused by the hysteresis generated in the crystals. Physik Instrumente states in its product catalog that the "amount of hysteresis increases with increasing voltage applied to the actuator (2008). The 'gap' in the voltage/displacement curve typically begins around 2% and widens to a maximum of 10% to 15%" (Physik Instrumente, 2008) as shown Figure 25.

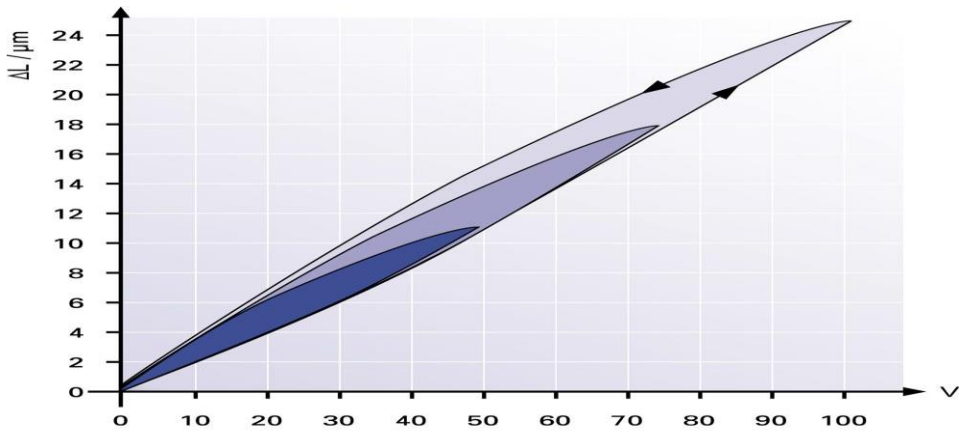

Figure 25: Hysteresis curves of an open-loop Piezo actuator for various peak voltages. The hysteresis is related to the distance moved, not the nominal travel range (Physik Instrumente, 2008, p 2-185)

In the measurement of the hysteresis, the same step function is applied as with the total travel by increasing the voltage applied to the Piezo Crystals from 0 to its maximum voltage in 2 second acquisition periods. After the maximum voltage is reached, the voltage was brought down to 0 volts in the same manner. Hysteresis curves are obtained for maximum voltages of 20, 40, 60, 80, and 100 volts. Hysteresis curves are obtained for voltage applied to the X axis while the Y axis was unloaded, voltage applied to the Y axis while the X axis was unloaded, and voltage applied to both axes simultaneously (Figure 26).

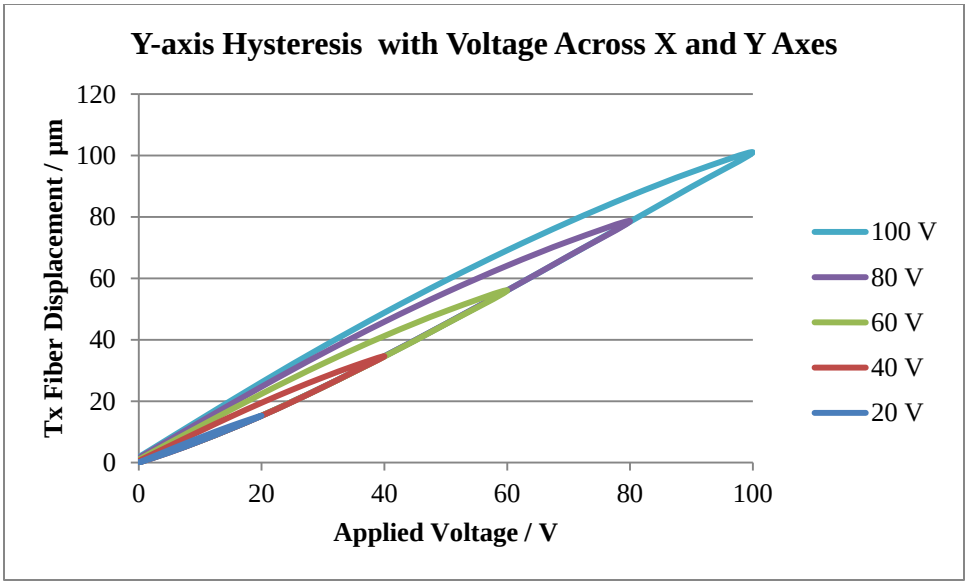

Figure 26: Example of a Hysteresis curve for voltage applied to the Y axis[1]

Like the results for the total travel, the data is acquired at 1 second after the change in voltage was complete due to large differences between filtered and unfiltered data near the initial start value. Equation (6) was used to shift the hysteresis to the initial start value.

Similarly to the Piezo Crystal specifications, the hysteresis is a maximum of 15.4% in the Y axis and a maximum of 14.4% in the X axis. In its operating condition, the NPS will only be exposed to open-loop hysteresis through its point ahead voltage range of 9.4 volts. In order to find the maximum hysteresis over this voltage range, we first analyze the "gap" in the voltage/displacement curves for each voltage as seen in Figure 27.

[1] See Appendix I: Room Temperature Hysteresis Data

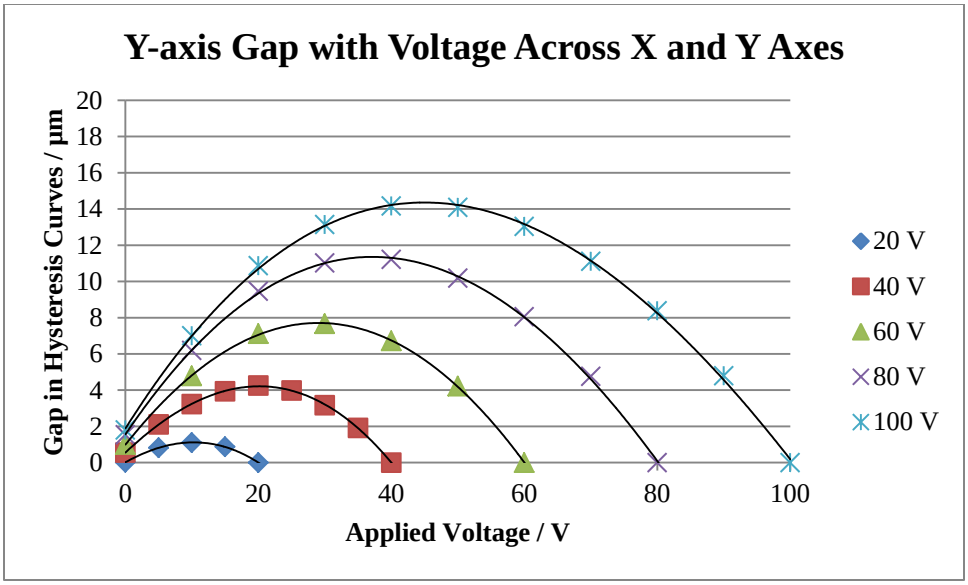

Figure 27: Example of a Hysteresis "Gaps" for various voltages where voltage was applied to the X axis[2]

The information about the gap allows us to precisely determine the maximum gap in the hysteresis curves for various voltages. From these maxima, we are able to accurately interpolate our results to find the maximum hysteresis at 9.4 volts as seen in Figure 28. From this model we were able to predict the hysteresis for the open-loop accuracy as shown in Table 16. Over a maximum applied voltage of 9.4 volts, the maximum hysteresis was measured to be 0.376 microns (± 0.19 microns) in the X axis and 0.347 microns (± 0.17 microns) in the Y axis.

[2] See Appendix I: Room Temperature Hysteresis Data for all hysteresis gap charts

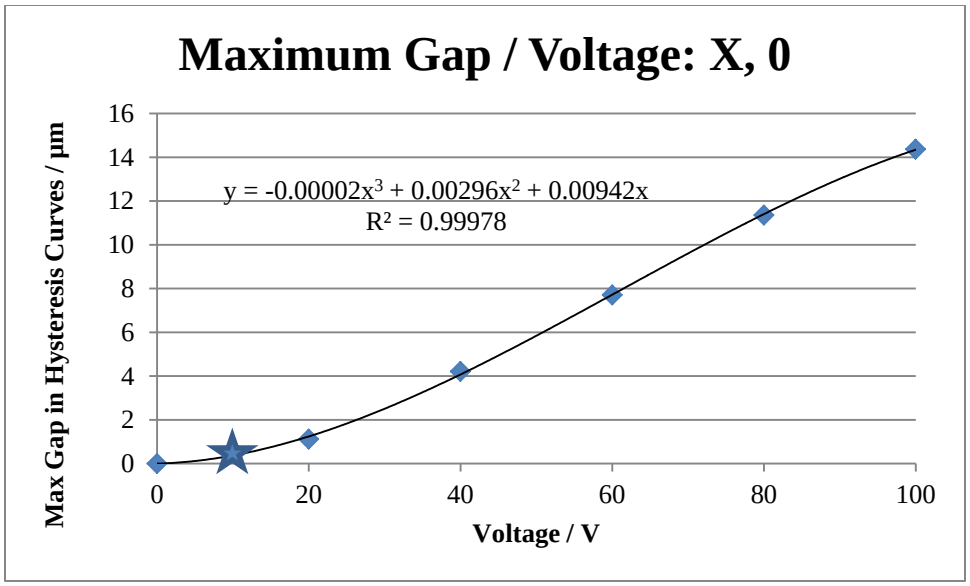

Figure 28: Example of the Maximum Gap in the Hysteresis for select voltages where voltage was applied to the X axis[3]

Table 16: Open-loop Accuracy Budget Hysteresis - 12 mil Stage

Error source	Value (µm)	Comments
Thermal actuation		Over 1 °C change
Creep	± 0.13	Over 2 min acquisition
Thermal Drift	TBD	Over 1 °C change
Hysteresis	**± 0.19 (X)** **± 0.17 (Y)**	Max applied voltage of 9.4 V
Sub Total		Requirement of ±0.6 µm

4.2.5 Resolution

The resolution is the smallest increment that the fiber optic head could move with a change in voltage. Performance specifications require that it be able to move in increments as small as 60 nm. Resolution testing, an original goal of this MQP, was not conclusive due to large overall error of our testing system.

[3] See Appendix I: Room Temperature Hysteresis Data for all maximum gap charts

A test plan was derived for the resolution test. Three different tests were to be run, one starting at 1 V, another starting at 50 V, and a final test beginning at 90 V. The voltage was to be increased by 10 mV increments up to 100 mV. Using data collected, linear interpolation would be used to determine the resolution at 1 mV. It was important to look at the data at low, medium and high voltages to determine whether the starting voltage had any factor upon the resolution.

Theoretically, the resolution of Piezo actuators is unlimited (Physik Instrumente, 2008). There is no threshold voltage and therefore the crystal can move in as small of increments as commanded. The limiting factor is the accuracy of the voltage driving system and, in particular, the noise caused by the voltage source, and ambient conditions. Noise on the order of μV can cause small changes in the length of the Piezo crystal. According to the data sheet for the PCI-6259 card, at the voltage range being used the accuracy of the voltage output was only 2 mV. Coupling this with noise from the amplifier, room vibrations and sensor noise, we decided that accurate resolution data could not be achieved using our test set up. The true resolution would be smaller than any value that could be derived with any confidence using our test set up. Further resolution testing is recommended for future work using a more precise test set up.

4.3 Temperature Tests

Thermal analyses of the stage were conducted using the setup described previously in a nitrogen-filled thermal chamber. This setup is used to conduct a series of specific tests that concluded whether the stage had met the requirements of the project sponsor. The thermal analyses were conducted using the following tests: survival cycling, total travel, voltage vs. displacement, creep, and thermal actuation. Every test was conducted by the same personnel using the same setup, equipment, and testing location.

4.3.1 Thermal Sensor Drift

Displacement data was taken from the sensors over the entire survivability range in order to quantify sensor drift of the Kaman KD5100 sensors. The crystals were left unloaded during this test. This test was completed using the fixed target setup (Figure 15). All of the components involved are made with Invar 36 except for the aluminum target blade. Changes in size of the aluminum target blade are small and occurred at the same magnitude over all of the thermal testing. It is not considered in the error. The ramp rate is set to 3°C per minute and the temperature dwelled at the extremes for 20 minutes.

Thermal data collected in the test was analyzed and as temperature increased so did the sensor readout for displacement. Over the course of the survivability range, the sensor readout increased by approximately 2.05 μm. The graph for this test can be found in Appendix M: Sensor Drift Graph. There is no distinct pattern to the increase that can be seen from the data. Possible reasons for the change in displacement are the different CTE values for the Invar components and the KD 5100 sensor heads. The sensors are rated to work beyond the survivability range, according to the manufacturer's data sheet.

4.3.2 Survival Cycling

This test consisted of three temperature cycles throughout a range of -40°C to 70°C at a ramp rate of 3°C per minute. The test began at room temperature and then begins three cycles which includes a twenty minute lag time at the maximum and minimum points in order for the stage to reach the air temperature. The temperature profile for this test can be found in Appendix L: Temperature Profiles. Additionally, the stage was placed on a 3 inch piece of Styrofoam to isolate it from the chamber vibration. The main purpose of this test is to inspect the stage after the cycling for any visible cracks or deformations. At the end of the test, inspection concluded

that there was no evidence of damage. Total travel tests were conducted before and after the survivability cycling to ensure no loss of travel was caused by thermal stresses.

4.3.3 Thermal Actuation

Thermal actuation of the NPS was an important consideration when determining the total travel of the NPS, as well as the open-loop accuracy. For total travel, the thermal actuation was measured over the operational range of 25 ºC to 35 ºC. For open-loop accuracy budget, the amount of thermal actuation was measured over a 1 °C temperature change within the operating range was considered. Based on input from a senior thermal analyst, it was determined that this would be the greatest amount of temperature change that the stage would see over the two minute relay acquisition period.

Testing was completed on the stage for thermal actuation with 60 V applied to the crystals. It was determined that there is a difference in the CTE of the crystal when voltage is applied compared to when it is not stimulated. One other consideration that was taken into account was the characteristics of the sensors over the temperature change. These were compensated for during the analysis of the data.

The NPS was attached to the Invar testing fixture for stability and to match the CTE of the NPS with its fixture. The temperature in the thermal chamber started at 25 °C and increased at a ramp rate of 0.75 °C per minute until the air temperature reached 40 °C. Data was recorded from when the NPS reached a temperature of 25 °C and recording stopped when the NPS reached 35 °C. Three test trials were completed to check for repeatability.

Upon analysis of the data, the thermal actuation was far greater than our models had projected. Looking at the differences between the experiment and the model, it was suspected that the difference in thermal conductivity between the Piezo crystal and the Invar was to blame,

along with the ramp rate of the temperature profile. We assumed that the temperature of the invar differed from the temperature of the crystal based off the fact that invar takes a much longer time to reach ambient temperatures. The data was discarded because the ramp rate exceeded that of operating conditions.

The second test setup for the thermal actuation included a thermocouple that was placed on the crystal. We monitored the temperature of the crystal to determine if there was a difference in temperature change between the crystal and the invar stage. This change would account for the difference in thermal actuation that we noticed in the first test. A thermocouple was used to monitor the temperature of the crystal instead of an RTD (which is more accurate) because it is smaller and was the only temperature detector that was able to fit onto the crystal. A new test profile was created with the ramp rate decreased to 0.5 $^{\circ}$C per minute. This is the maximum rate that the NPS will be exposed to during the acquisition period assuming linear temperature change (1 $^{\circ}$C change over a two minute acquisition period). The temperature profile for this test can be found in Appendix L: Temperature Profiles.

For the second test, only two trials were completed due to time constraints. Though only two trials were completed, the results compared very well with each other so they were considered valid. Completion of the second test sequence yielded results that differed greatly from the FEA (Figure 29 and Figure 30). Our results showed a thermal actuation of 4.08 μm in the X axis and a thermal actuation of 3.63 μm in the Y axis, while our model predicted values of 3.32 μm and 2.70 μm in the X and Y axes, respectively.

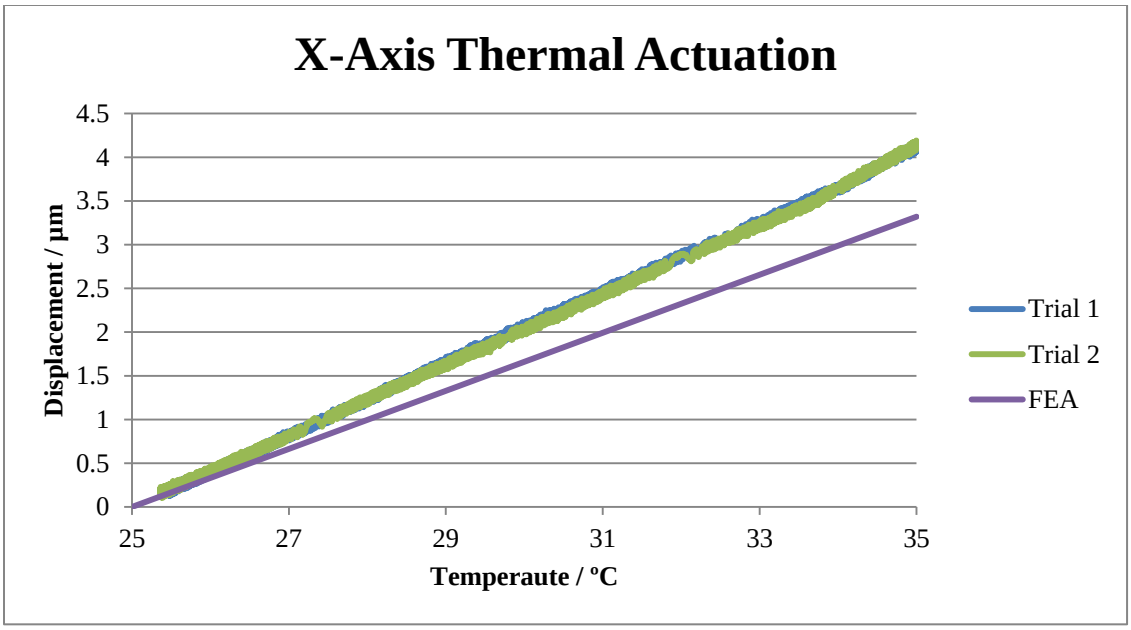

Figure 29: Measured X-axis thermal actuation compared to FEA

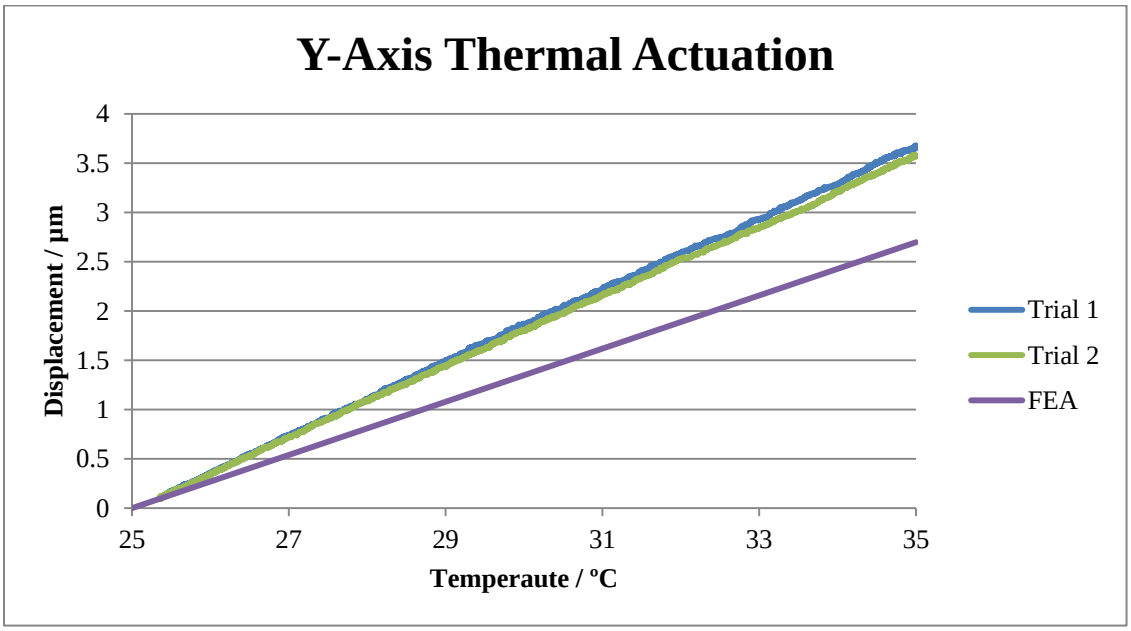

Figure 30: Measured Y-axis thermal actuation compared to FEA

Examining the temperature data from the tests, we noticed that the change in temperature for the crystal differed from the change in temperature for the invar stage by about 2 ºC in Trial 1 and Trial 2 (Figure 31 and Figure 32). It is worth noting that the temperature data in figures 31 and 32 is quite noisy, containing high frequency, moderate amplitude variation. This is suspected to

be the result of one of two local effects. The first is the close proximity of the thermocouple to the locally intense electric field strength of the crystals when actuated at 60V. The second effect is the proximity to the very rapidly oscillating magnetic field created by the eddy current position sensors. Both of these effects are likely to have some influence on the temperature readings of the thermocouple, however it is assumed that these phenomena are zero mean and do not affect the averaged temperature data.

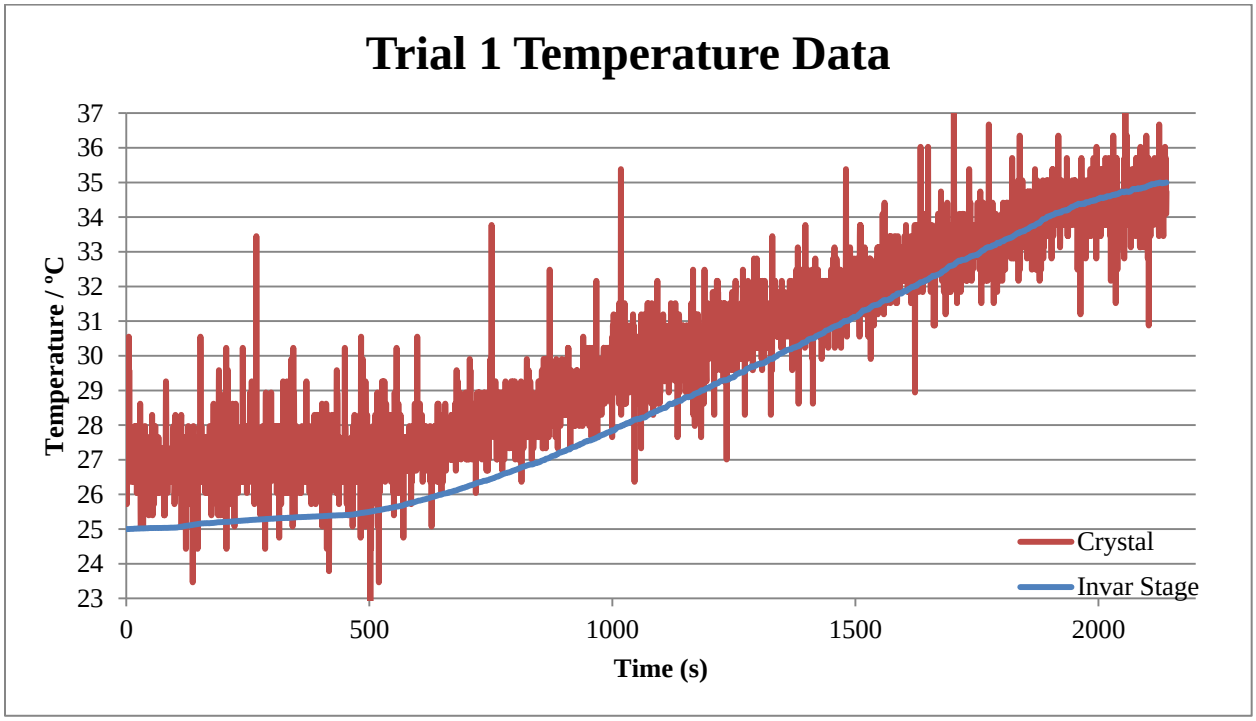

Figure 31: Difference in temperature of the crystal and invar stage for Trial 1

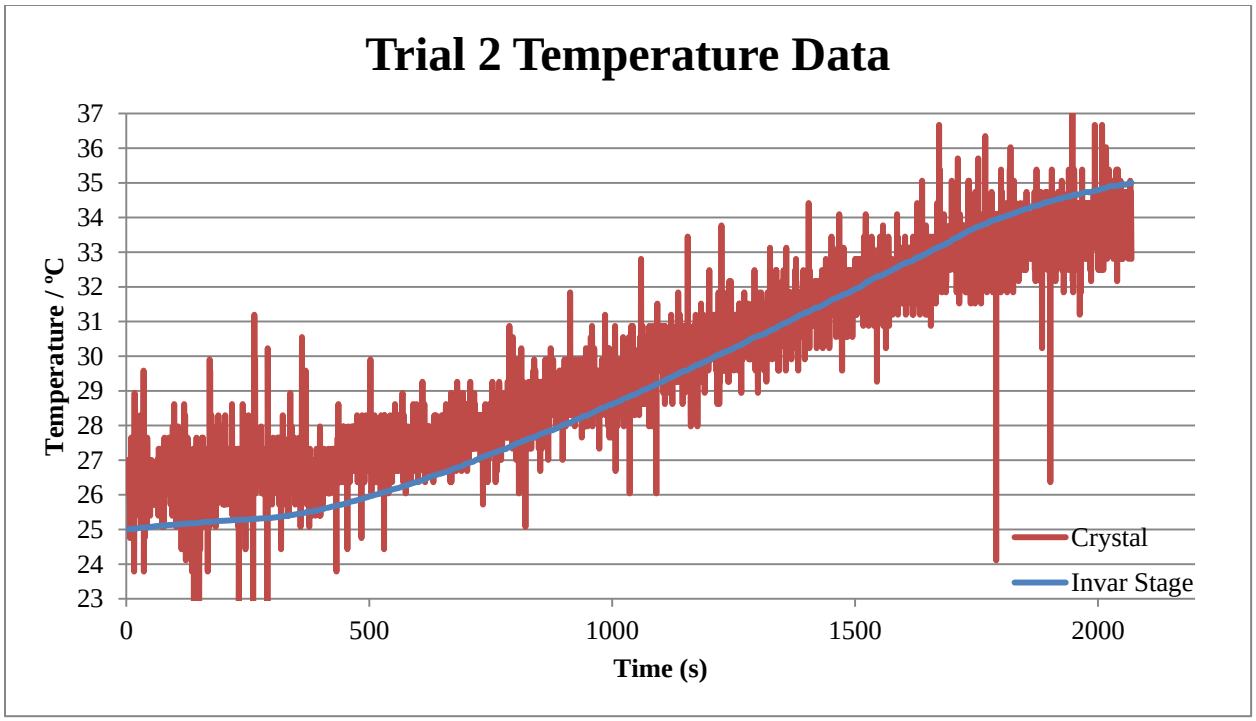

Figure 32: Difference in temperature of the crystal and invar stage for Trial 2

From these results, it was determined that the FEA from Chapter 2 was invalid. A new model was created in which the change of the temperature for crystals was 2 degrees less than that of the invar stage. The results from the new FEA correlate very well with the measured values for the thermal actuation validating our methods (Figure 33and Figure 34).

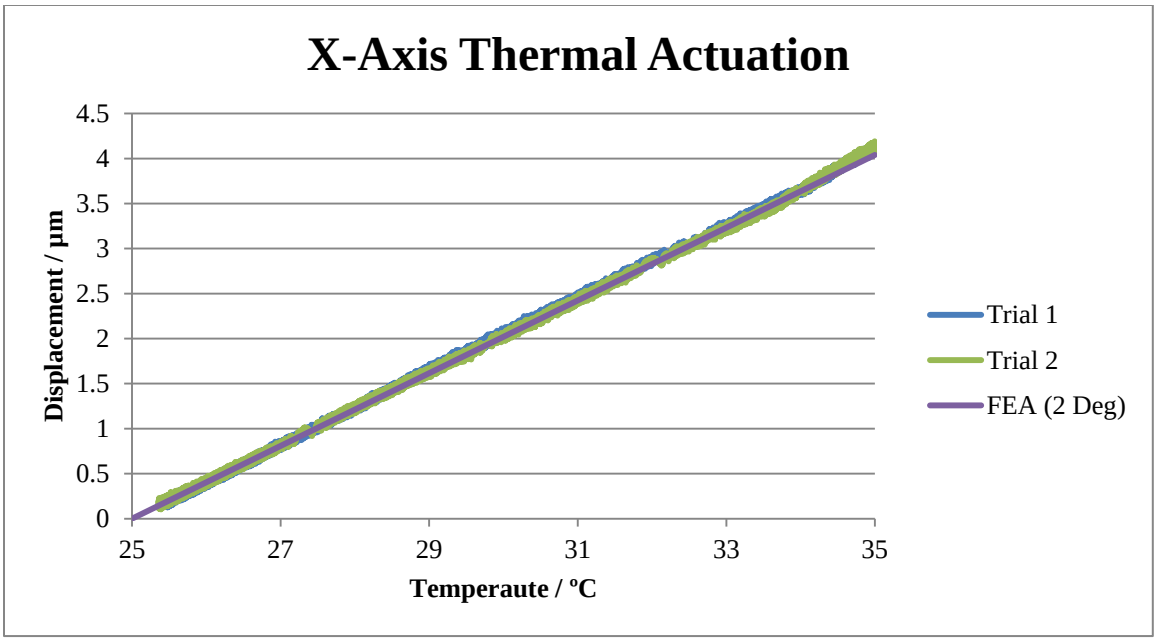

Figure 33: Measured X-axis thermal actuation compared to FEA with a 2 ºC change considered

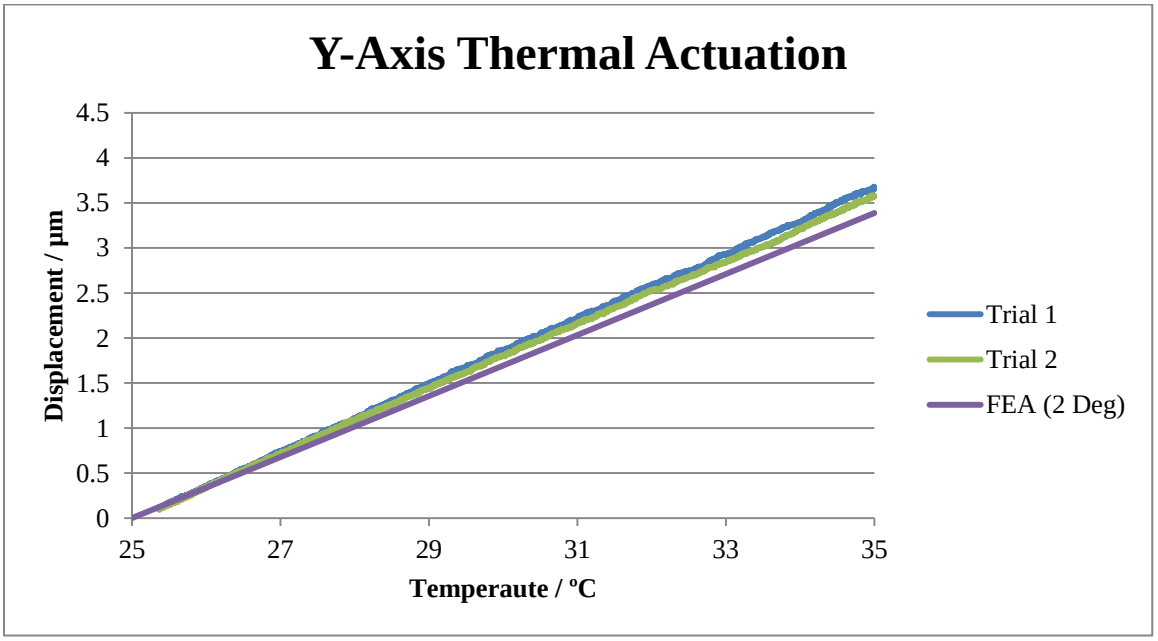

Figure 34: Measured Y-axis thermal actuation compared to FEA with a 2 ºC change considered

With the new model, we determined that the results could be considered valid for the total stroke requirements. Inputting these into the total stroke requirements (Table 17),

determinations were able to be made regarding the total stroke that was needed for the 12 mil stage.

Table 17: Total Stroke Requirements Thermal Actuation - 12 mil Stage

Contributor	Value (µm)	Comments
Point ahead	± 4.7	
Bore sight stroke	± 7	
Steer off 1.5 pixels	± 8.4	
Alignment	± 25	Misc. mechanical
Thermal actuation	**± 2.04 (X)** **± 1.82 (Y)**	Due to -CTE of Piezo Crystal
Thermal drift	± 0.26	Due to stage mounting
System level thermal drift	± 10	Due to optics
Sub Total	**± 57.40 (X)** **± 57.18 (Y)**	Total stroke needed

With the thermal actuation results over the operational range of temperature, we predicted that the total stroke needed for the NPS is ± 57.40 microns (114.82 microns) in the X axis and ± 57.18 microns (114.36 microns) in the Y axis.

We were also able to determine the open-loop accuracy by determining the thermal actuation over 1 $^{\circ}$C change. Over 1 $^{\circ}$C change, we can assume that the difference in temperature between the crystal and the invar stage can be no larger than 1 $^{\circ}$C. Since our results accounted for a 2 $^{\circ}$C change between the crystal and invar stage, we used FEA to predict the maximum amount of thermal change the NPS would be exposed to over the acquisition time. The FEA for a 1 $^{\circ}$C difference yields a thermal actuation of 0.37 µm in the X axis and a thermal actuation of 0.30 µm in the Y axis. With these values, we were able to fill in the remainder of the open-loop accuracy budget (Table 18).

Table 18: Open-loop Accuracy Budget Thermal Actuation - 12 mil Stage

Error source	Value (µm)	Comments
Thermal actuation	**± 0.18 (X)** **± 0.15 (Y)**	Over 1 °C change
Creep	± 0.13	Over 2 min acquisition
Thermal Drift	TBD	Over 1 °C change
Hysteresis	± 0.19 (X) ± 0.17 (Y)	Max applied voltage of 9.4 V
Sub Total		Requirement of ±0.6 µm

Chapter 5 – Conclusions and Recommendations

Upon completion of this MQP, conclusions and recommendations for future work have been drawn. Chapter 5 details the conclusions and recommendations.

5.1 Conclusions

This project has come to four main conclusions that are important to emphasize. They are the following:

1. The NPS has been characterized for performance over operating conditions
2. Minor changes to the NPS should allow it to reach its total travel goals over the full operational range
3. The NPS as tested accuracy is sufficient to meet its performance requirements open-loop over the full operational range
4. The NPS will survive the full storage temperature range

These conclusions will be detailed and explained thoroughly in the following sections.

5.1.1 FEA vs. Experimentation

This MQP has outlined data acquired from both FEA and experimentation. The FEA proved extremely useful in giving expectations of what would be seen in the laboratory. In some instances, it was noted that preliminary measured data did not correlate with the FEA. At this point, both the FEA and the test procedures were scrutinized. Errors in both were looked for to determine why the data did not correlate. It gave a means for refinement of both the FEA and the test procedures, yielding more accurate results.

Table 19 shows the comparison between the FEA and the measured data for total travel, and Table 20shows the comparison between the FEA and the measured data for thermal

actuation. It can be seen that the FEA correlates very well with our measured data is can be considered an accurate way to model the NPS

Table 19: FEA vs. Measured Total Travel

Axis	FEA (µm)	Measured (µm)
X	109.65	**110.0**
Y	104.11	**100.1**

Table 20: FEA vs. Measured Thermal Actuation

Axis	FEA (µm)	Measured (µm)
X	4.04	**4.09**
Y	3.39	**3.68**

Correlation could not be achieved for voltage vs. displacement analyses and testing. This is due to the fact that the FEA results were completed in a linear fashion, while the true travel acts as 3rd order polynomial. The end points of our voltage vs. displacement correlate, but the intermediate data points do not. This can be seen in Figures 27 and 28.

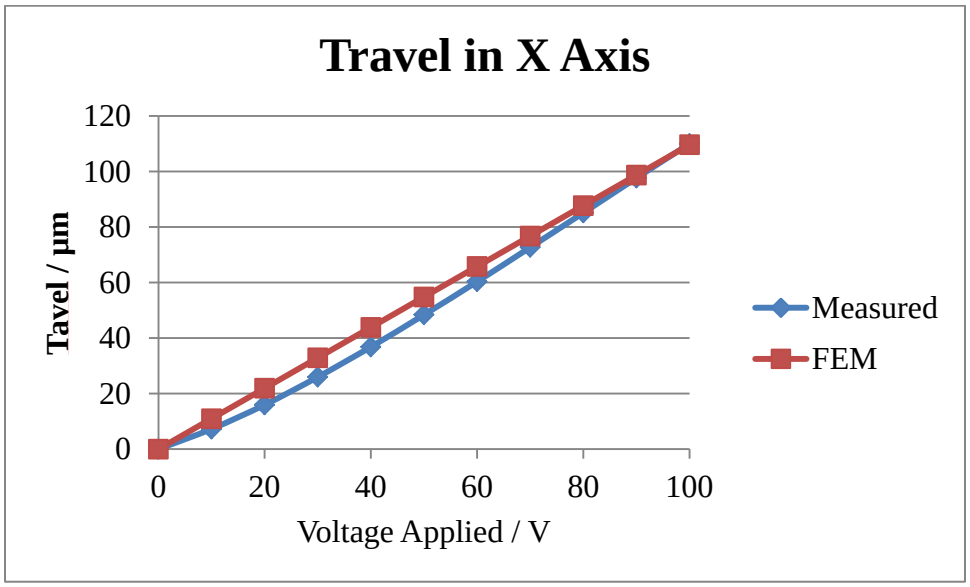

Figure 35: Total Travel in the X Axis

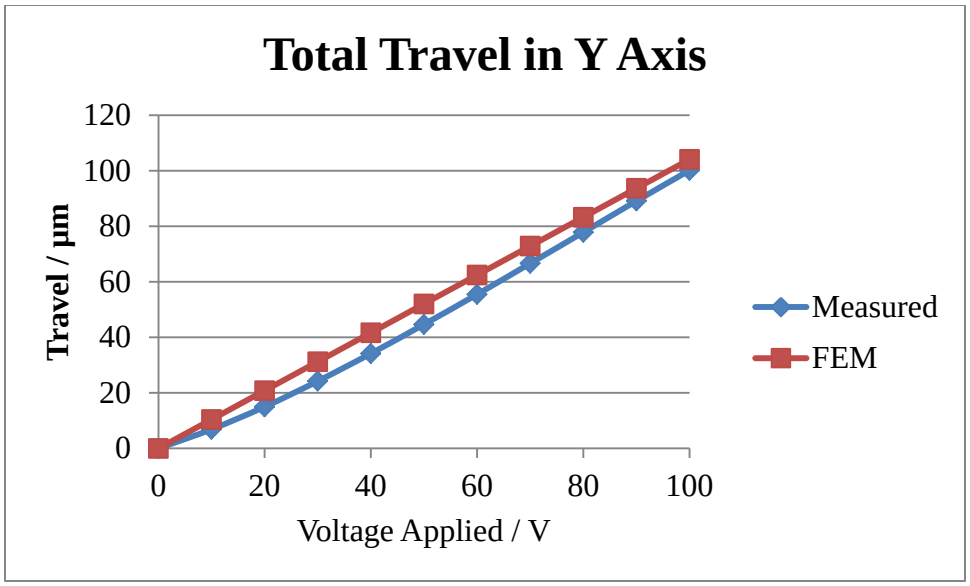

Figure 36: Total Travel in the Y Axis

Testing and analysis has proven that the tested stage did not meet the total travel requirements. As outlined in this paper, the total travel in both axes did not meet the requirements as found here. It is believed that the 10 mil design will pass the requirements based upon analysis of the total travel.

5.1.2 Total Travel

Through analyses and testing, it has been concluded that the 12 mil flexure design will be just shy of meeting the total travel requirements as given in this MQP. Table 21 compares the total stroke required to the FEA results and the measured data. The NPS falls just short of its requirements in both axes of motion. Recommendations will be made in section 5.2 that should ensure the NPS can make its total travel requirements.

Table 21: Total Travel Conclusions

Axis	FEA (µm)	Measured (µm)	Stroke Needed (µm)	Measured Difference (µm)
X	109.65	110.00	**114.80**	-4.80
Y	104.11	100.10	**114.36**	-14.26

5.1.3 Open Loop Accuracy

It is anticipated that open-loop control will be a viable option for the NPS. With the 12 mil design, ±0.09 μm remain in the budget for the X axis and ±0.11 μm remain in the budget for the Y axis for thermal drift. See Table 18 for each parameter in the budget. It is believed that the values for thermal drift will fit into these specifications but cannot be known for sure at this time. Further testing and analyses will need to be completed to determine the actual value for the thermal drift of the NPS.

5.1.4 10 mil Flexures vs. 12 mil Flexures

The 10 mil flexure thickness has been shown through analysis to generate a larger stroke in both the X and Y axes than the 12 mil design. Though, the implication of the 10 mil design will change the conclusions regarding the total travel requirements, as well as the open-loop accuracy requirements. Because the FEA regarding thermal actuation was validated by our measurements, we were able to predict the thermal actuation of the NPS with 10 mil flexures. This allowed us to determine the change in the total travel requirement and the open-loop accuracy budget. From our analysis, we determined that 10 mil flexure thickness does cause an increased thermal actuation, though the amount of the actuation is very small with regards to the budget requirements. Over the survival range, considering a 2°C difference between the stage and the crystals, the difference in the thermal actuation between in the 10 mil and 12 mil designs is estimated to be ±0.13 microns in the X axis (Figure 37) and ±0.11 microns in the Y axis (Figure 38).

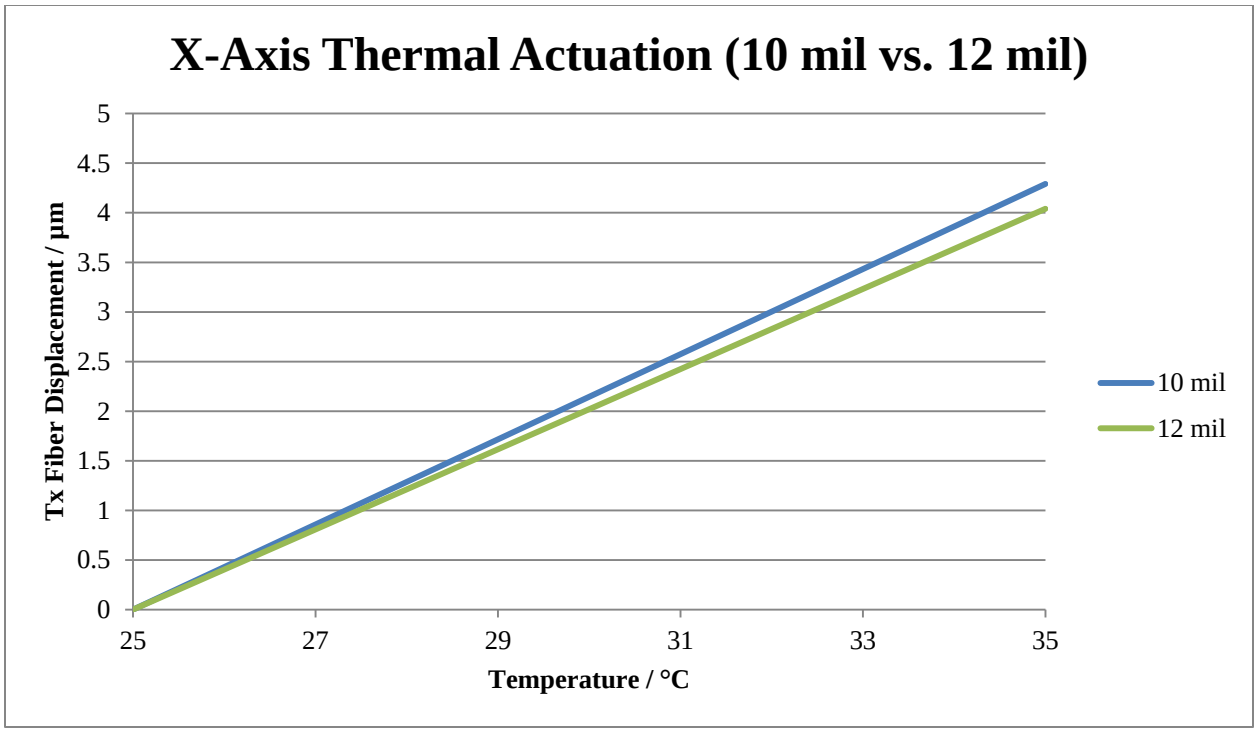

Figure 37: X-axis thermal actuation comparison for the 10 mil vs. 12 mil design and a 2°C difference

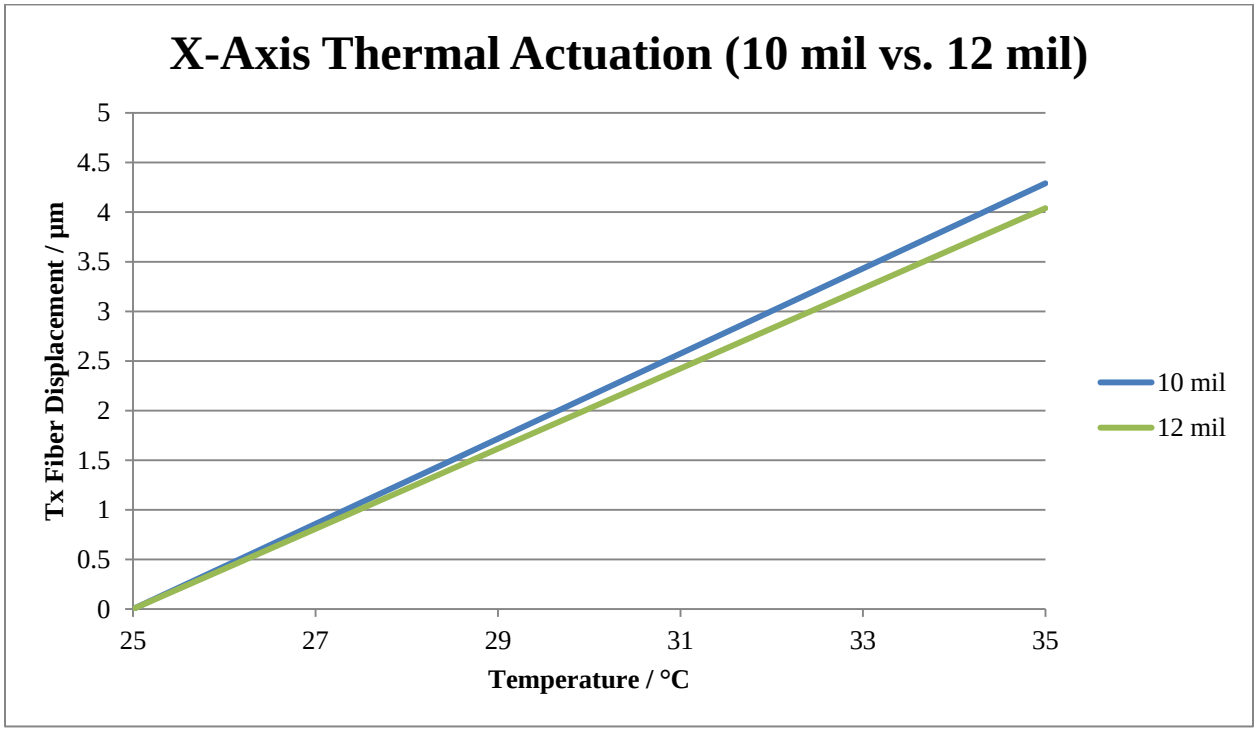

Figure 38: Y-axis thermal actuation comparison for the 10 mil vs. 12 mil design and a 2°C difference

During the acquisition period, considering a maximum temperature difference between the stage and the crystals of 1°C, the difference in the thermal actuation between in the 10 mil and 12 mil designs is estimated to be ±0.01 microns in both the X and Y axes (See Appendix N: Thermal Actuation Graphs (10 mil vs. 12 mil) for all graphs relating to the thermal actuation differences in the 10 mil vs. 12 mil designs). Accounting for this difference, the 10 mil stage will still meet the open-loop accuracy requirements. Since the thermal actuation difference between the two designs was very small, it can be assumed that the hysteresis and creep values will follow the same results. This can only be confirmed through testing since the hysteresis and creep cannot be tested for using FEA.

5.1.5 Temperature Survival

Through testing, it was concluded that the NPS survived the full storage range of -40°C to 70°C. Thorough inspection showed no signs of physical deformation of the NPS due to stresses caused by extreme temperatures. The total travel of the NPS remained the same before and after thermal cycling. This leads us to conclude that the NPS can be stored at any temperature in the storage range and still remain operational when the temperature is brought back into the operational range.

5.2 Design Recommendations

Through testing and analyses, this MQP has come up with several design recommendations for MIT LL. These recommendations are based on testing and analyses done throughout the MQP as well as first-hand experience using the stage. They will be detailed in this section.

5.2.1 Target Assembly

Over the course of testing, it was found that the aluminum target blades had problems staying attached to the target ring. It is believed that during the calibration process for the sensors the epoxy is put under stress and the bond between the target ring and blade fails. Our MQP group recommends a redesign of the target assembly. To eliminate the possibility of the epoxy failing, the entire assembly should be fabricated from one piece. The entire piece should be constructed of Invar to keep all of the thermal properties consistent with the rest of the stage. Invar is not a suitable material for the target due to constraints posed by the KD 5100 sensor heads. Aluminum is the optimal material for the target blades. The Invar target blades will need to be covered with aluminum to ensure that the sensors work.

The small displacements of the aluminum target blades caused by the epoxy shifting during thermal cycling also posed issues with calibrating the sensors. A small movement in the target blade can result in a large displacement. To receive accurate data, sensors had to be constantly recalibrated. Having to recalibrate the sensors added an extra variable into the equation which needed to be accounted for.

5.2.2 10 mil Flexure Thickness

Modeling has shown that switching the flexures to 10 mil thickness will give the NPS more than the total travel of the 12 mil thickness stage according to our physical testing and FEA. FEA results show that the 10 mil design has a total travel of 116.92 μm in the X axis and 112.80 μm in the Y axis. Testing will have to be completed to verify this model. It is expected that this design will also be able to satisfy the other specifications for the NPS but testing will have to be completed to verify this.

5.2.3 Total Travel Budget

The total travel is comprised primarily of two factors, alignment and system level thermal drift. This can be seen in Table 22.

Table 22: Alignment and System Level Thermal Drift

Contributor	Value (µm)	Comments
Point head	± 4.7	
Bore sight stroke	± 7	
Steer off 1.5 pixels	± 8.4	
Alignment	**± 25**	**Misc. mechanical**
Thermal actuation	± 2.05 (X) ± 1.84 (Y)	Due to –CTE of Piezo
Thermal drift	± 0.26	Due to stage mounting
System level thermal drift	**± 10**	**Due to optics**
Sub Total	± 57.12 (X) ± 56.80 (Y)	

The alignment can be reduced by increasing the tolerances on the entire optics bench. If the bench is fabricated with extreme precision, the budget required for alignment will decrease. Better thermal control may decrease the budget for the system level thermal drift. With both of these numbers decreased, the stage will be able to meet its total travel requirements.

5.3 Testing Recommendations

Additional testing of the NPS is recommended to ensure that it will be able to meet all of its specifications. Testing includes room temperature, thermal, vibration, and closed-loop which will be discussed in the following sections.

5.3.1 Resolution

During the course of testing, a test plan for determining the resolution of the NPS was derived. Unfortunately, the hardware set up used for the other tests could not handle such precise testing. It is recommended that another team use more precise hardware to determine the resolution of the NPS. This is a crucial figure to know for the controls engineering team. Theoretically, the Piezo crystal can has no limits on resolution but testing needs to be completed to determine the resolution for the entire NPS.

5.3.2 Thermal

Voltage vs. displacement at varying temperatures is important in determining the feasibility of the NPS. It will be important to know whether or not the total travel of the NPS will meet the specifications throughout the entire operational range. The testing and analyses completed within this MQP has shown that at room temperature, the NPS with the 12 mil flexures will fall just short of the necessary total travel. Analysis has shown that the NPS with 10 mil flexures will meet the specifications for total travel at room temperature. The next step in the process will be analyses and testing of the 10 mil NPS for voltage vs. displacement throughout the entire temperature operational range.

Understanding the creep of the 10 mil NPS is crucial in fully understanding the total travel of the NPS, as well as the open-loop accuracy. Creep is a key parameter in the open-loop accuracy budget and for open-loop accuracy to be an option; the NPS must perform within budget allocations throughout the entire operational range. With regards to the total travel of the stage, it's impossible to truly know where the travel ended and creep began until a full analysis of the creep has been completed. Creep has been shown to be as great as 3.5 μm after two minutes, which is a non-trivial amount of the total travel. For these reasons, it will be important

for future groups to perform and analyses and testing of the creep throughout the entire operational temperature range.

5.3.3 Vibration

Using the vibration fixture and test plan developed by this MQP, vibration testing will need to be completed on the NPS. Vibration analyses were completed during the course of this MQP, and measured data must be acquired to verify these models. During operation, vibrations may pose an issue to the NPS. Models suggest that the first model frequency is high, but verification will be needed to support the models. For the 12 mil stage, the first modal frequency is 540 Hz. For the 10 mil stage, the first modal frequency is 506 Hz.

Shock will also need to be analyzed and tested. This analysis cannot be completed using SolidWorks Simulation but this group recommends using Nastran. Upon completion of modeling, testing will need to be completed to verify the models. This test can be done on the same shaker as the previous vibration testing. The acceleration must reach 20 G and be sustained for 25ms. It is recommended that baseline testing of total travel be completed before and after the test to prove the survival of the NPS.

Unfortunately, due to lack of additional stages and time constraints we would like to recommend this test as part of future work on this stage. Group 74 was only able to provide one stage for testing. This made it impossible to perform vibration testing on stage in parallel with our other tests, which was our original intention. This stage was critical to obtain data throughout all of our other tests and Group 74 was hesitant to put it through a vibration test which would put it at risk of being damaged. For all of these reasons we were unable to perform vibration testing of the NPS but we do recommend it as part of future work on the stage.

5.3.4 Closed-Loop Testing

In order to fully confirm that the stage design is appropriate and meets all performance requirements we recommend a series of closed-loop tests be performed. The closed loop testing should start by setting an initial position and moving to a final position. After this is successful and completed a larger sweep of an area or specific space should be performed. Next, a flight like mission or simulation should be run using appropriate behavior and testing. Finally tracking in real time exactly what the stage should be doing is necessary to conclude that all the performance requirements and expectations of the stage have been met in a closed-loop setting.

5.4 Summary

This MQP group has found that the NPS will function as intended with an open-loop control method during the acquisition period. The NPS design is accurate and robust, however it currently falls slightly short of its needs for total travel. With minor adjustments outlined earlier in this section, the NPS should be able to meet all of its performance and environmental requirements.

This MQP provided valuable information to MIT LL. With the testing and analyses completed, design changes will be made. Physical test fixtures have also been developed to complete further testing, as well as VI's which can be used in the future. The conclusions and recommendations drawn in this project will help MIT LL achieve its end goals for highly accurate beam pointing by a nano-positioning stage within a laser communications demonstration system.

Works Cited

Cengel, Y. A., & Cimbala, J. M. (2009). Grid generation and grid independence. In B. Stenquist (Ed.), *Fluid mechanics: Fundamentals and applications* (Second ed., pp. 857). New York, NY: McGraw-Hill.

Doyle, K. B., Genberg, V. L., & Michels, G. J. (2002). *Integrated optomechanical analysis* Society of Photo Optical.

Hemmati, H. (2009). *Near-earth laser communications* CRC Press.

Katzman, M. (1987). Laser satellite communications. *Englewood Cliffs, NJ, Prentice-Hall, Inc., 1987, 250 p.no Individual Items are Abstracted in this Volume., 1*

Lambert, S. G., & Casey, W. L. (1995). *Laser communications in space* Artech House.

Majumdar, A. K., & Ricklin, J. C. (2008). *Free-space laser communications: Principles and advances* Springer Verlag.

Massachusetts Institute of Technology: Lincoln Laboratory. (2012). Technical Divisions. Retrieved from http://www.ll.mit.edu/employment/division7.html

Physik Intstrumente. (2008) *Piezo Nano Positioning: Inspirations 2009.*

Szabó, B. A., & Babuška, I. (2011). *An introduction to finite element analysis* Wiley.

Appendix A: Coefficient of Thermal Expansion Calculations

The equation of linear expansion due to thermal expansion is:

$$L * \alpha * dT = dL$$

Where L is the initial length, α is the coefficient of thermal expansion, dT is the change in temperature, and dL is the change in length.

The expansion of the crystal, epoxy, and thermal compensator (shim) need add together to give an effective expansion:

$$dL_{crystal} + dL_{shim} + dL_{epoxy} = dL_{eff}$$

$$(l * \alpha * \cancel{\Delta T})_{crystal} + (l * \alpha * \cancel{\Delta T})_{shim} + 4(l * \alpha * \cancel{\Delta T})_{epoxy} = (l * \alpha * \cancel{\Delta T})_{eff}$$

$$\frac{(l * \alpha)_{crystal} + (l * \alpha)_{shim} + 4(l * \alpha)_{apoxy}}{l_{eff}} = \alpha_{eff}$$

	L (in)	α (ppm/°C)
Crystal	0.704	-3
Shim	0.100	23
Epoxy	0.015	57.6
Eff	0.819	1.59

$$l * \alpha * \Delta T = \delta$$

$$(l * \alpha * \cancel{\Delta T})_{crystal} + (l * \alpha * \cancel{\Delta T})_{shim} + 3(l * \alpha * \cancel{\Delta T})_{apoxy} = (l * \alpha * \cancel{\Delta T})_{Eff}$$

$$\frac{(l * \alpha)_{crystal} + (l * \alpha)_{shim} + 3(l * \alpha)_{apoxy}}{l_{Total}} = \alpha_{Eff}$$

$$\frac{(0.709\ in * -3\ \frac{ppm}{°C}) + (0.100\ in * 23\ \frac{ppm}{°C}) + 3(0.005\ in * 57.6\ \frac{ppm}{°C})}{(0.709 + 0.100 + 3 * 0.005)in} = \mathbf{1.258}\frac{\boldsymbol{ppm}}{°C}$$

$$= \alpha_{Eff}$$

$$\alpha_{invar} = \mathbf{1.260}\frac{\boldsymbol{ppm}}{°C}, \boldsymbol{difference\ in}\ \alpha = \mathbf{0.002}\ \frac{\boldsymbol{ppm}}{°C}$$

Appendix B: Room Temperature Finite Element Analyses (10 mil vs. 12 mil)

Minor: 0 V, Major: 100 V

X Displacement 10 mil	X Displacement 12 mil
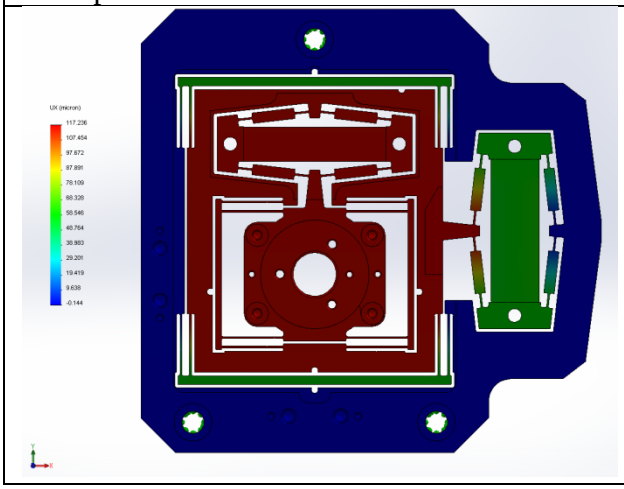	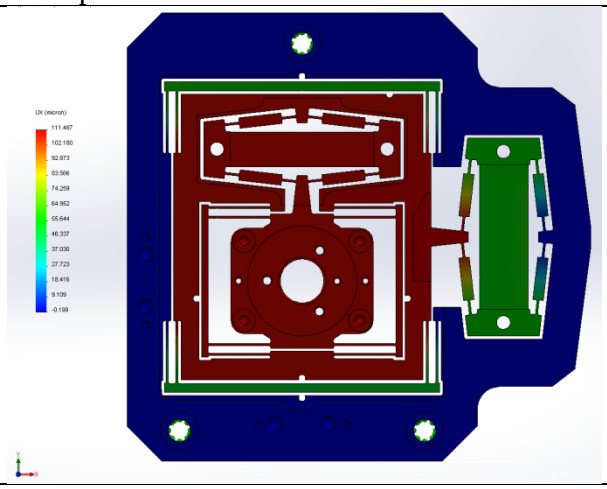

Cross-Axis Response 10 mil	Cross-Axis Response 12 mil
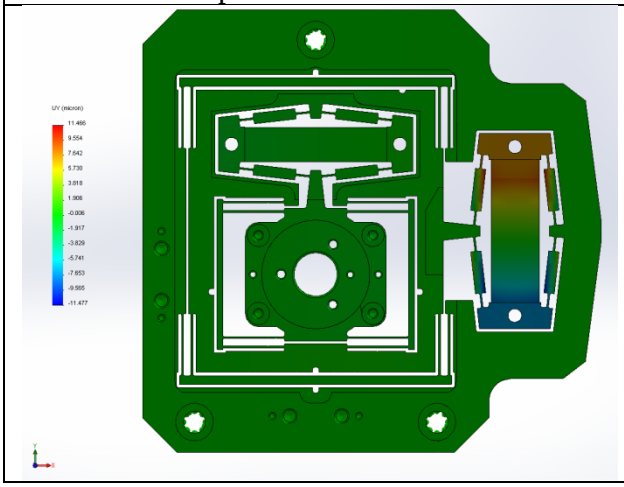	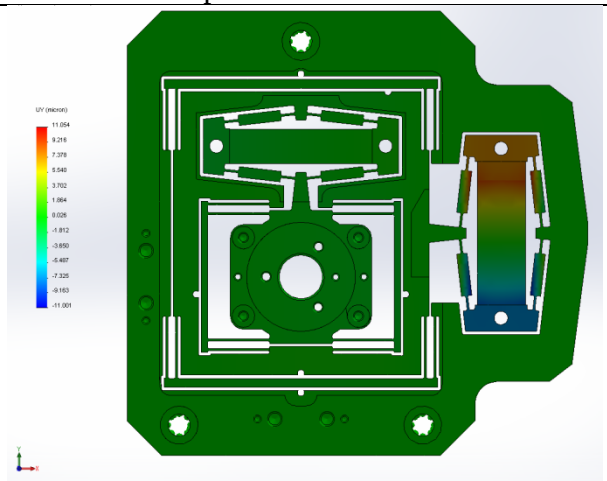

Minor: 100 V, Major: 0 V

Y Displacement 10 mil	Y Displacement 12 mil
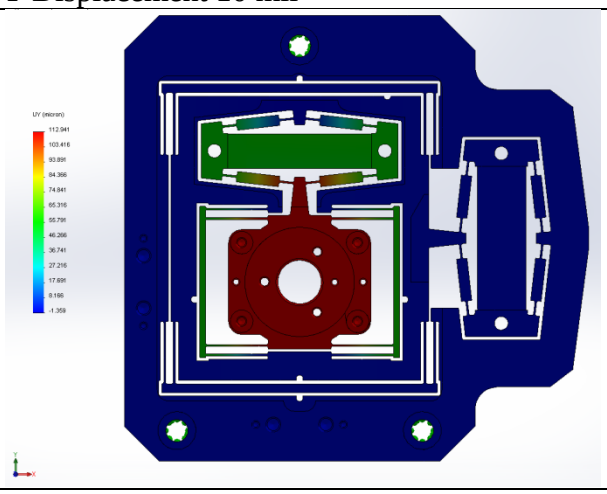	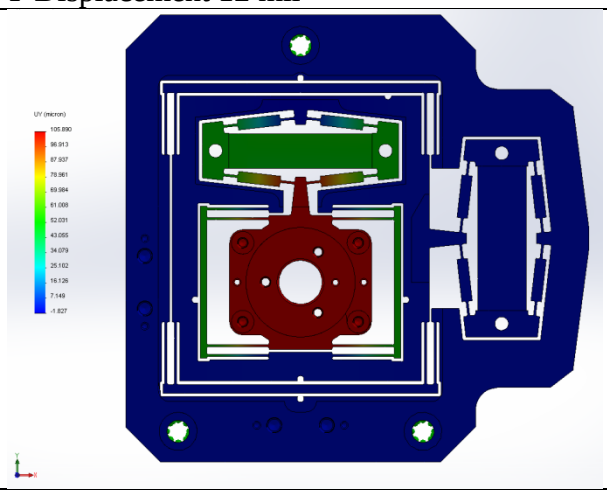

Cross-Axis Response 10 mil	Cross-Axis Response 12 mil
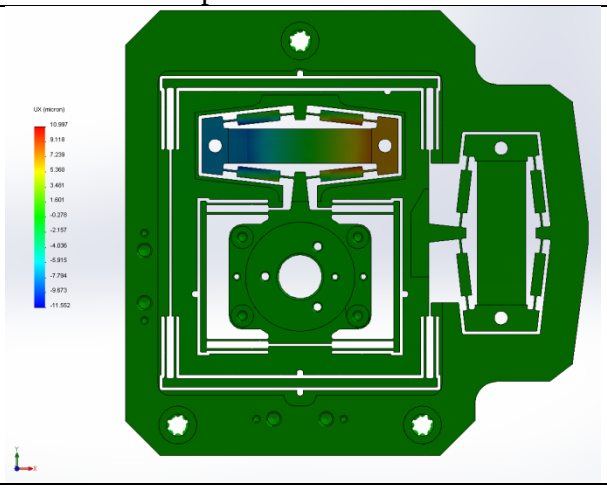	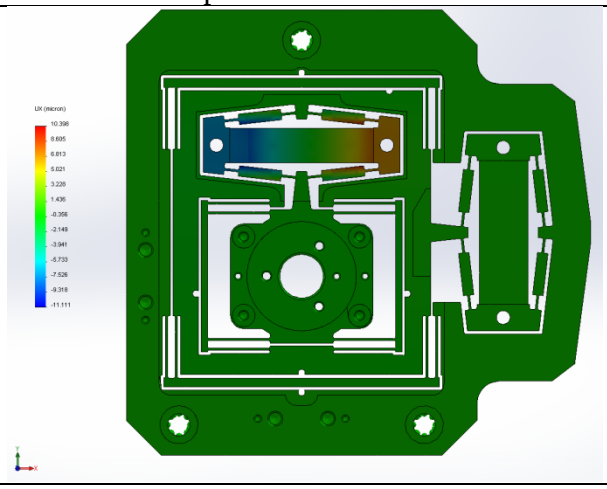

Minor: 100 V, Major: 100 V

X Displacement 10 mil	X Displacement 12 mil
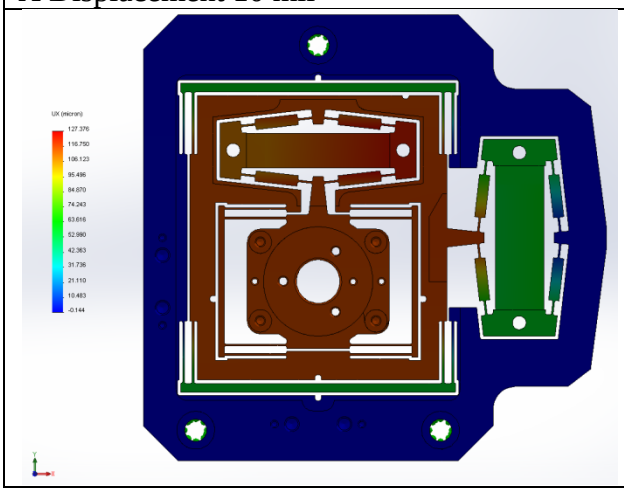	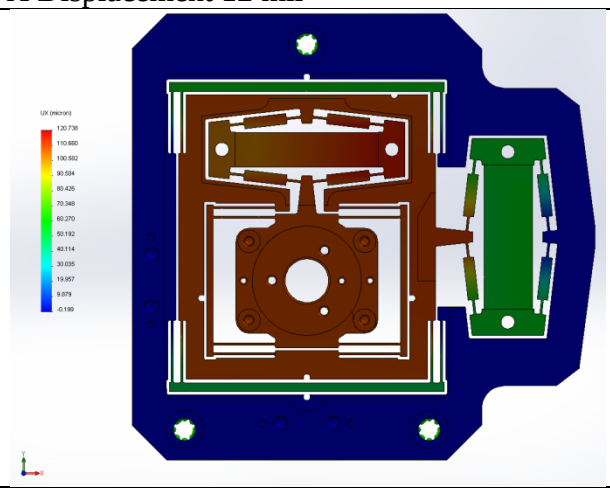

Y Displacement 10 mil	Y Displacement 12 mil
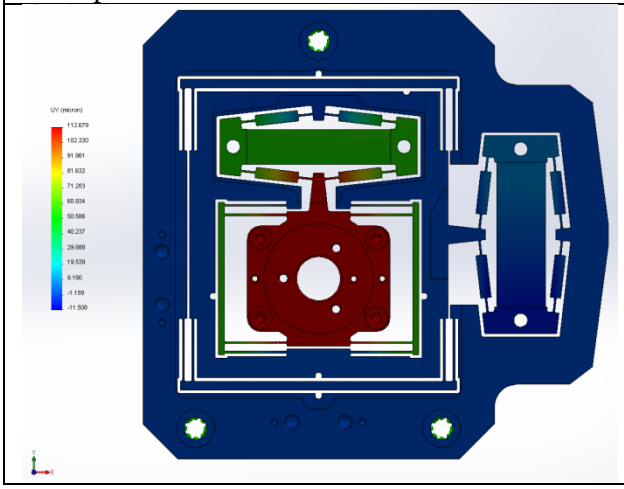	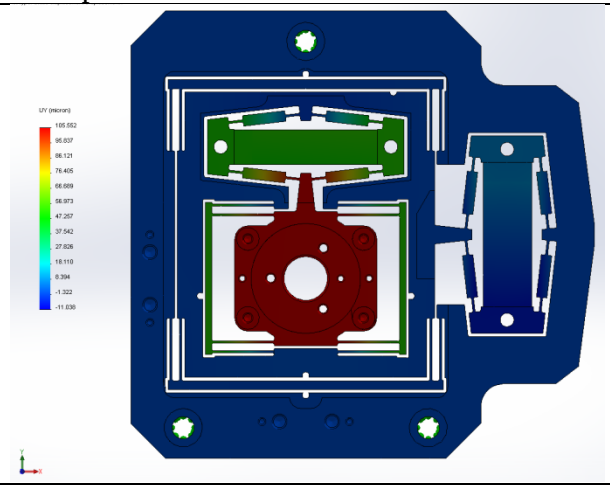

Appendix C: Vibration modal models for the 10 mil and 12 mil NPS Designs

10 mil Mode 1 (506.65 Hz)	12 mil Mode 1 (540.46 Hz)
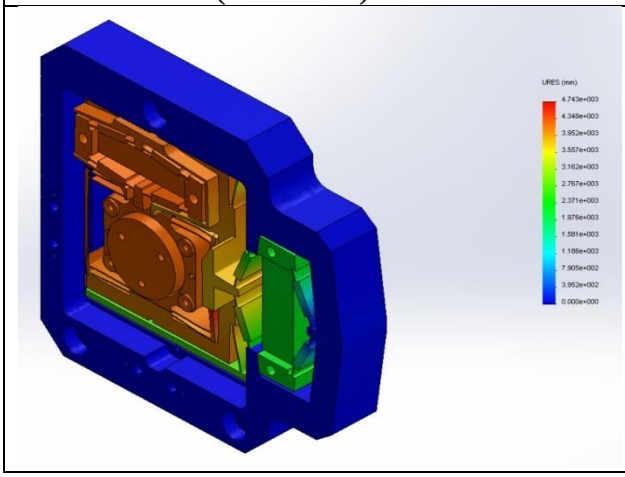	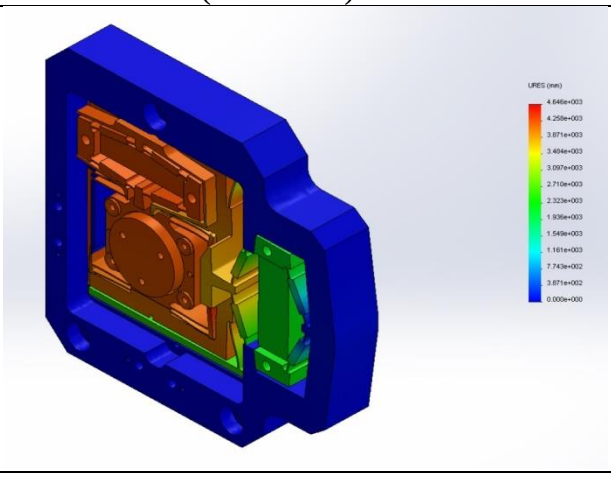

10 mil Mode 2 (717.32 Hz)	12 mil Mode 2 (771.06 Hz)
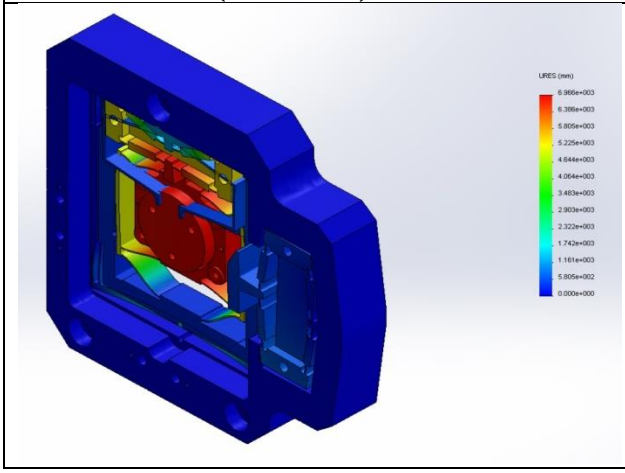	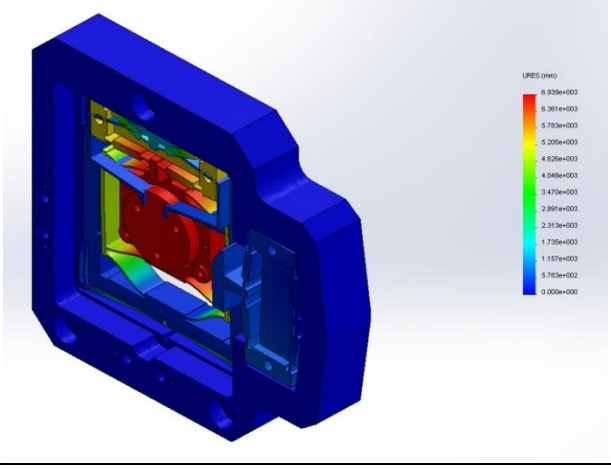

10 mil Mode 3 (999.94 Hz)	12 mil Mode 3 (1145.0 Hz)
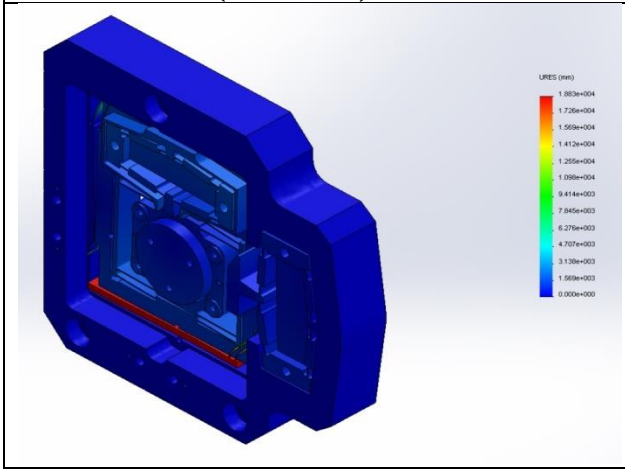	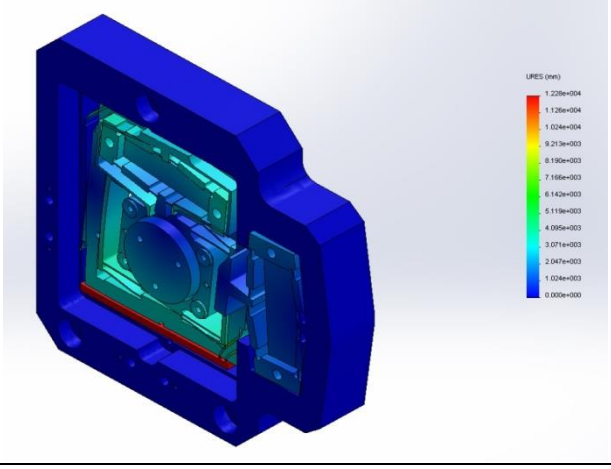

10 mil Mode 4 (1064.8 Hz)	12 mil Mode 4 (1239.2 Hz)
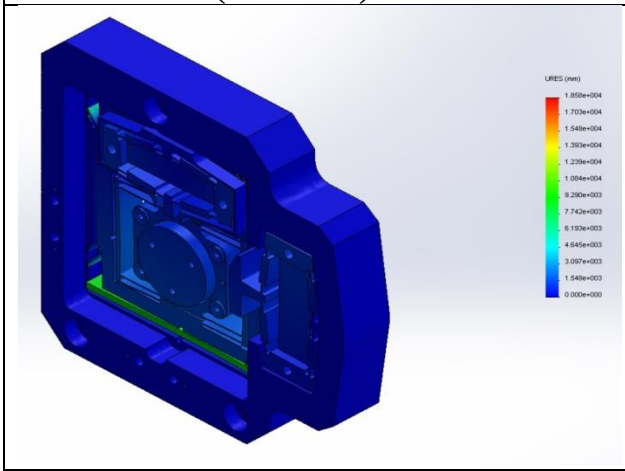	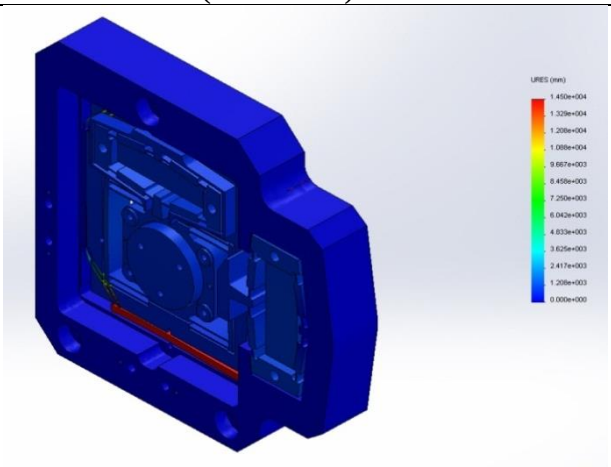

10 mil Mode 5 (1226.1 Hz)	12 mil Mode 5 (1290.5 Hz)
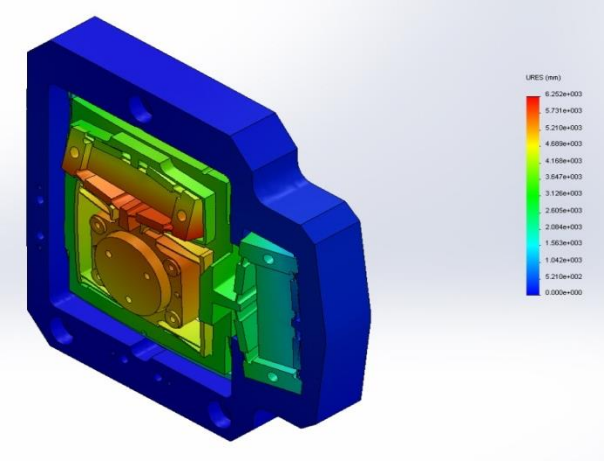	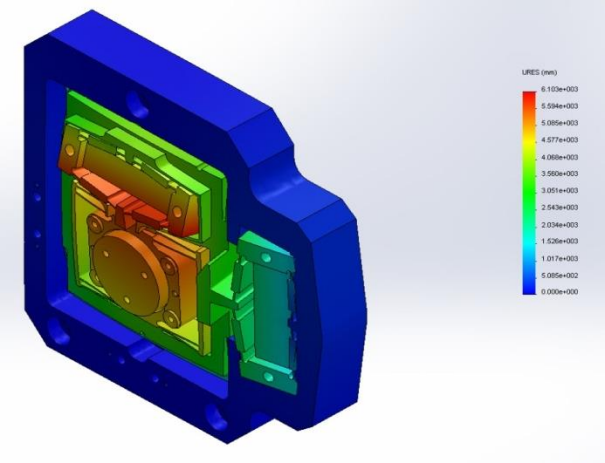

10 mil Mode 6 (1237.7 Hz)	12 mil Mode 6 (1325.1 Hz)
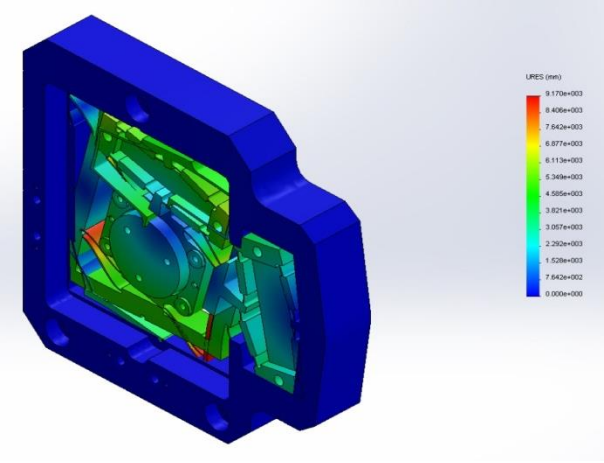	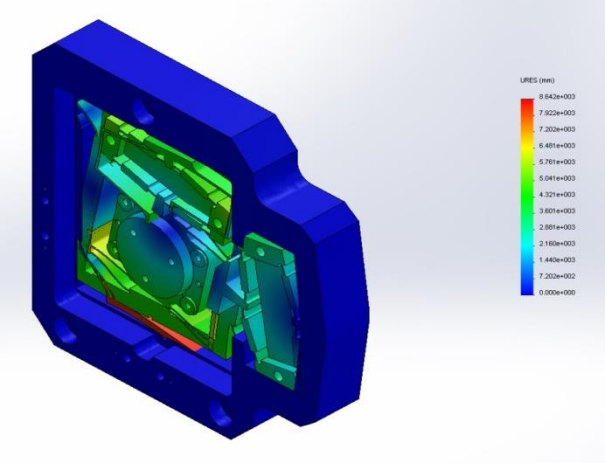

10 mil Mode 7 (1459.3 Hz)	12 mil Mode 7 (1563.7 Hz)
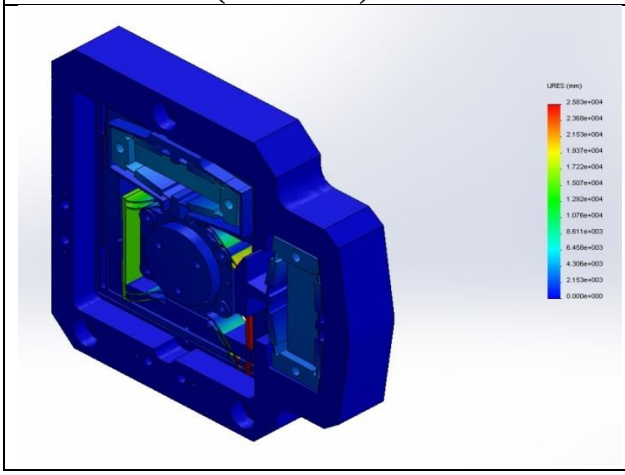	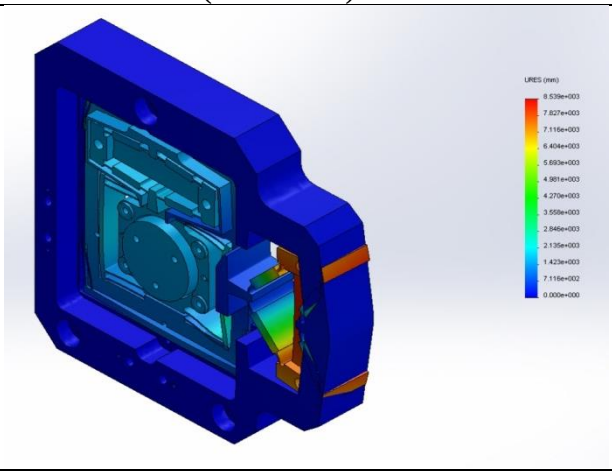

10 mil Mode 8 (1467.8 Hz)	12 mil Mode 8 (1649.6 Hz)
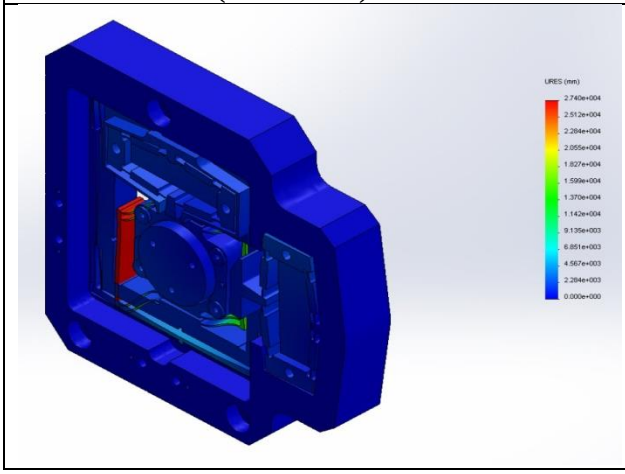	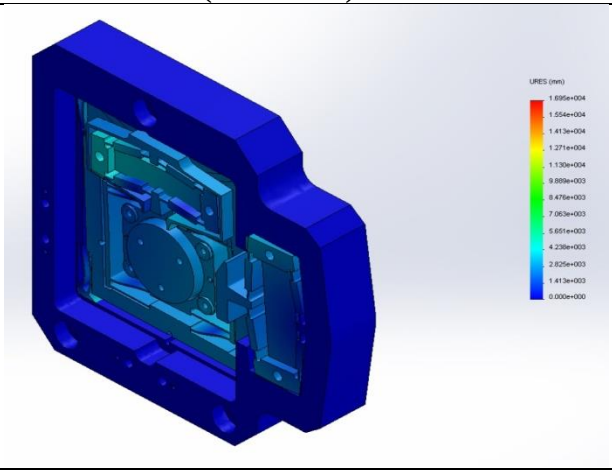

10 mil Mode 9 (1480.9 Hz)	12 mil Mode 9 (1707.9 Hz)
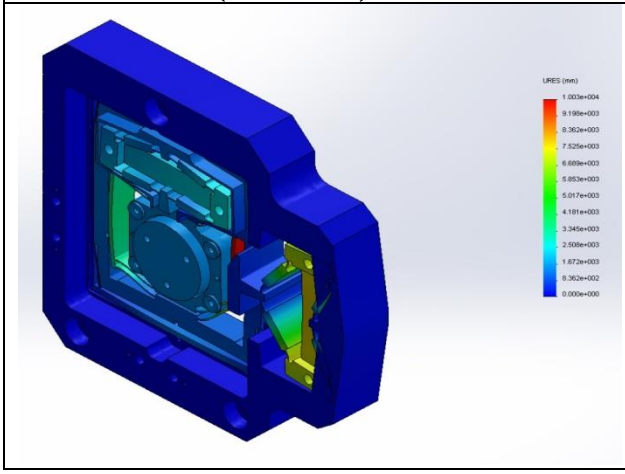	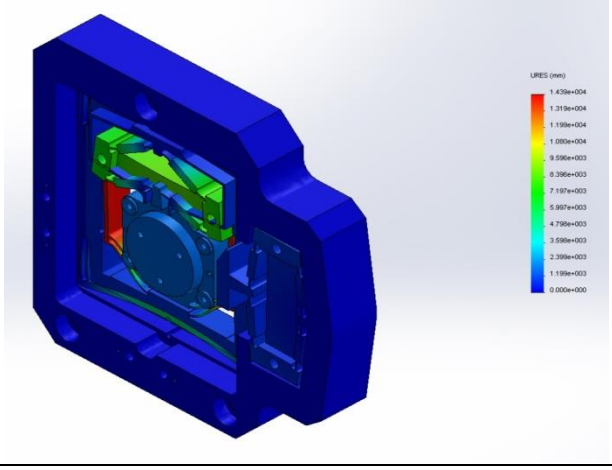

10 mil Mode 10 (1548.6 Hz)	12 mil Mode 10 (1792.8 Hz)
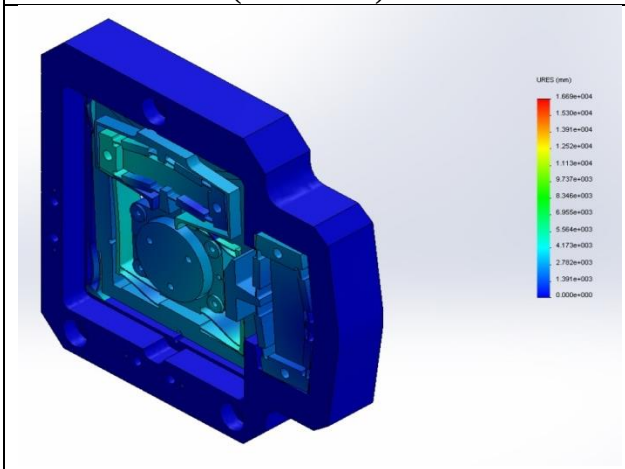	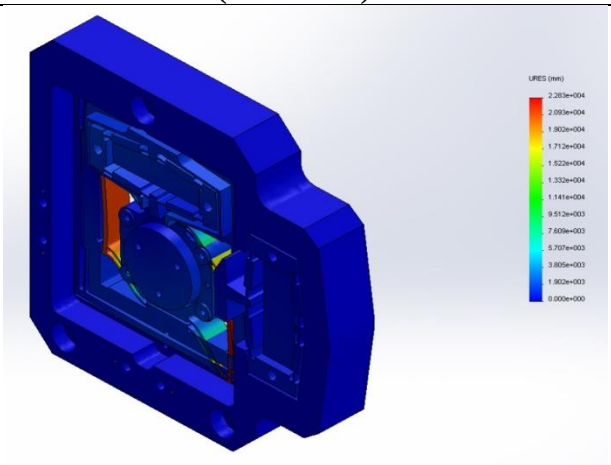

Appendix D: Test Fixture Drawings

Invar Test Fixture Base:

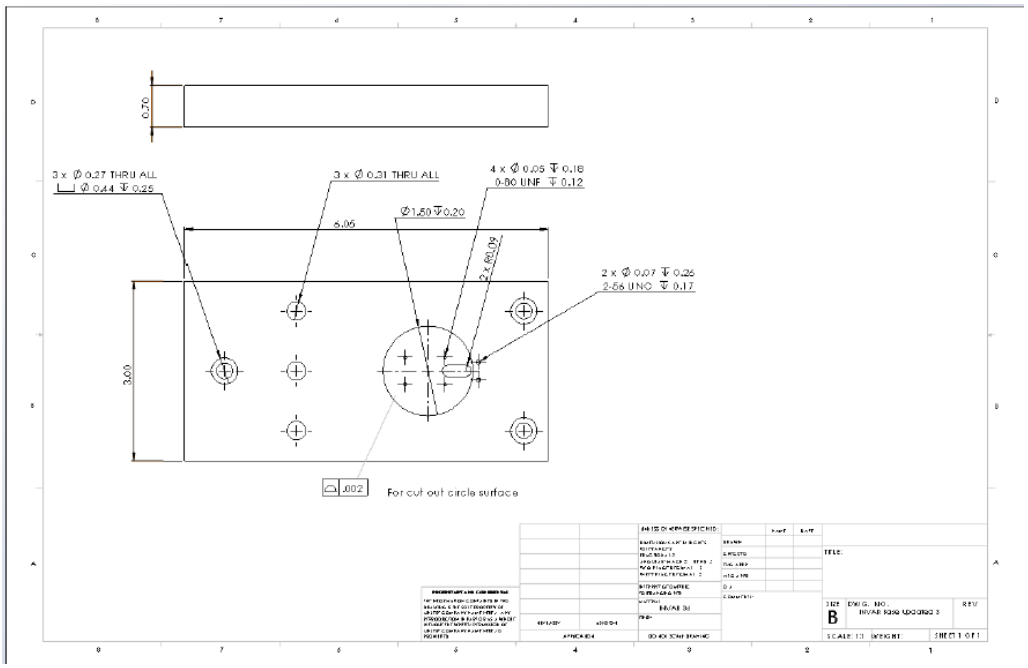

Invar Test Fixture Top:

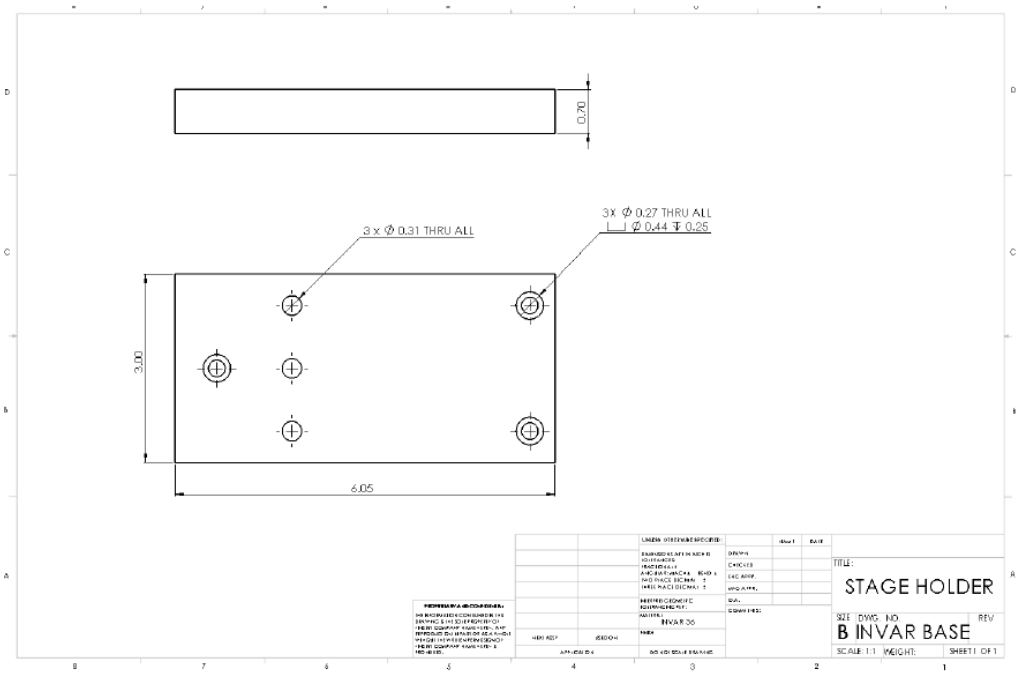

Aluminum Test Fixture:

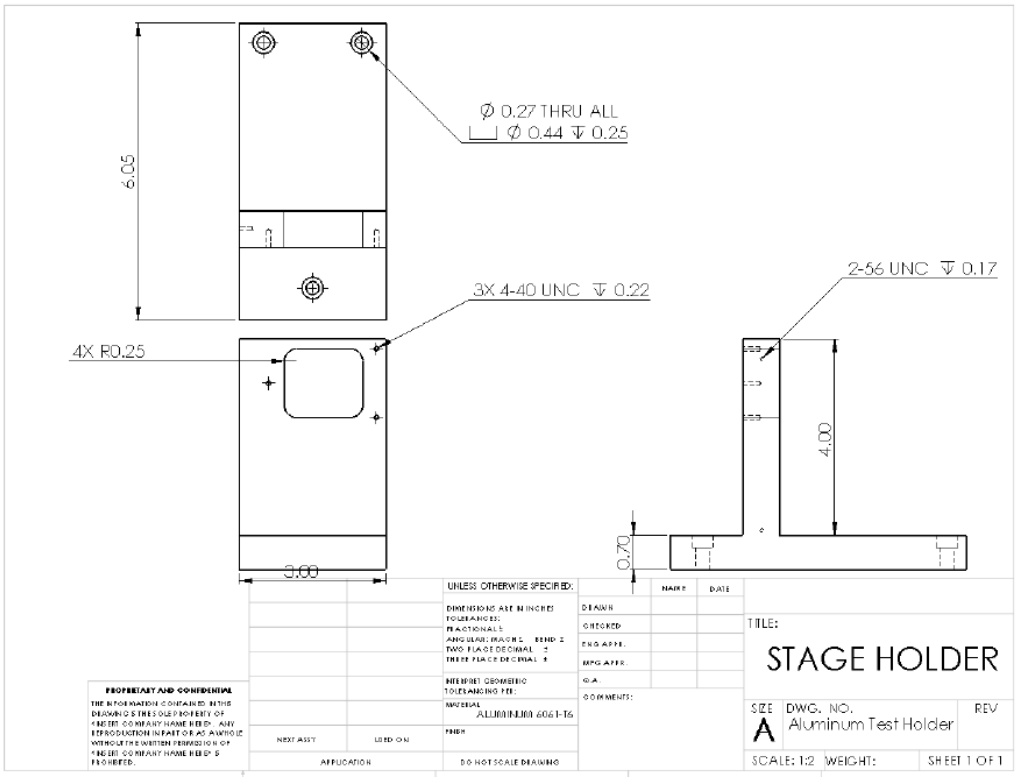

Vibration Test Fixture:

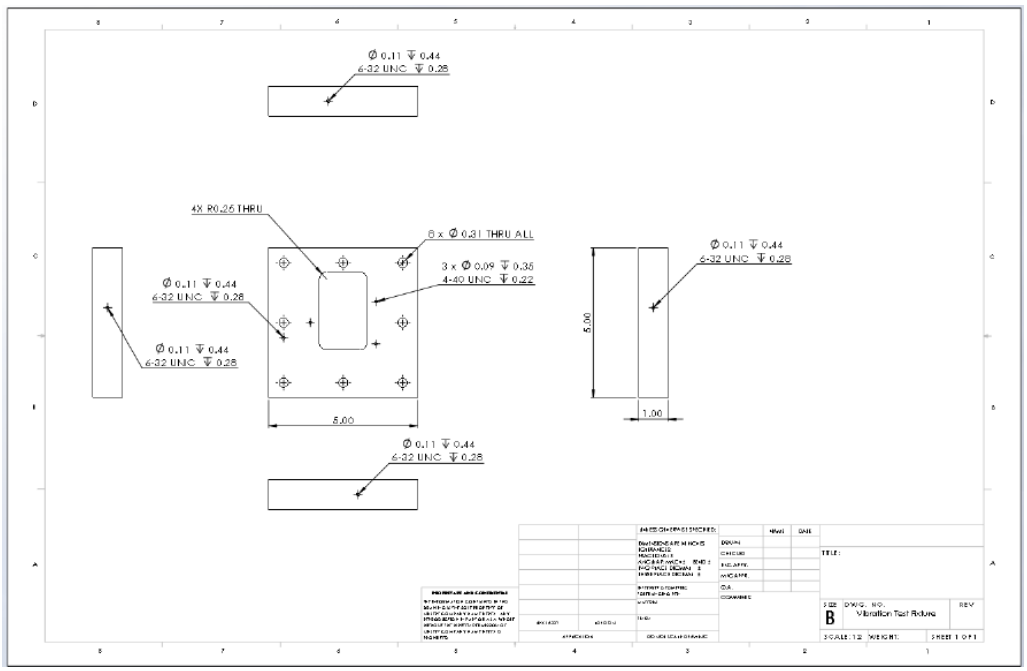

Appendix E: NPS Part Fabrication List

Part Name and #	#	Dimensions per piece (in)	Invar Required	Priority	Estimated completion date
809635-2 Shim 5x5 Piezo Crystal				2	8-22 in the AM Skip is doing
809635-3 Shim 7x7 Piezo Crystal	2			2	8-22 in the AM Skip is doing
809636-2 Bracket, Position Sensor Target	3	1.025 x .04 x 1.25	0.15 in^3	1	
809636-3 Target Blade	7			1	
809637 Bracket Fiber Stage Position Sensor	4	.6 x .675 x .25	.31 in^3	1	
809640 Flexure Block, Blank, Tx & Bcn	1	.425 x 2.75 x 2.55	5.5 in^3	3	
809569 Flexure Block, Tx & Bcn	1	SAME PIECE AS 809640	SAME PIECE AS 809640	3	Ar 191810 has been place for two parts estimated delivery ?
INVAR Test Top	2	3 x 4 x .75	18 in^3	2	Dave will order
INVAR Base	2	3 x 6.05 x .7	25.41 in^3	2	Dave will order
Vibration Fixture	1	5 x 5 x 1	Aluminum 6061	4	

Appendix F: RTD Specification Sheet

DATA SHEET R-SCAPLC

RdF

SEALED PLATINUM SURFACE TEMPERATURE SENSOR MODEL 29399

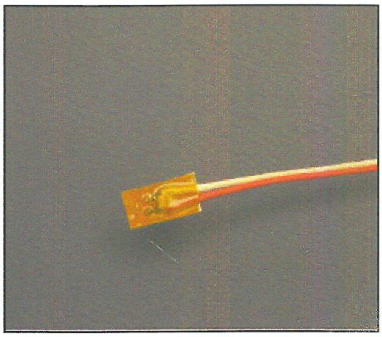

This low cost, sealed platinum surface RTD is the world's toughest for surface temperature measurement. The IEC 751 sensor is refractory sealed for ±0.05°C stability. Its small strong design allows this package to conform on curved surfaces for accurate response in milliseconds. Leads welded within the sealed RTD provide this sensor's durablity. Moisture resistance for condensing environments is provided by Kapton® lamination that encapsulates the assembly. Standard operating range is –50°C to 150°C.

- ***Strong welded leads***
- ***Full platinum RTD stability***
- ***Tough***
- ***Moisture resistant***
- ***Strain isolated***
- ***Temperature range is –50°C to 150°C***
- ***Time constant is 0.3 seconds on metal surfaces***
- ***Long-term stability better than ±0.05°C (0.02Ω) per 5 years***

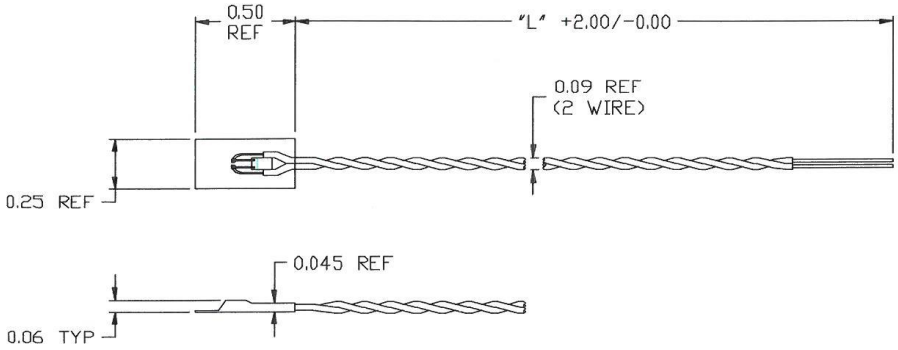

Specialists in Temperature Measurement

AS9100
ISO 9001:2000
CERTIFIED COMPANY

Performance Specifications

Temperature Range
–50°C to 150°C (–60°F to 300°F)

Sensing Element
International grade thin film platinum
$\alpha = 0.00385\ \Omega/\Omega/°C$

Ice Point Resistance
1000 ± 1.2Ω, (±0.3°C)
International Class B, (±0.12%)

Time Constant
<0.3 Seconds on metal surfaces

Self-Heating
>15 mW/°C mounted

Interchangeability
$\pm(0.3°C + 0.005|t|°C)$,
IEC 751 Class B

Long Term Stability
Better than 0.05°C (0.02Ω) per 5 years

Insulation Resistance
>50 MegOhms at 50VDC at 25°C

Maximum Current
2 mA for limited self heating

Recommended Current
1 mA maximum

Case Material
Kapton®, Sensor is refractory passified overall before lamination

Lead Material
26 AWG nickel-plated, stranded copper
TFE Teflon® insulated twisted leads

Size Reference
0.25" wide x 0.5" long
Thickness over sensor: 0.06"
Thickness over leads: 0.045"

Ordering Specifications

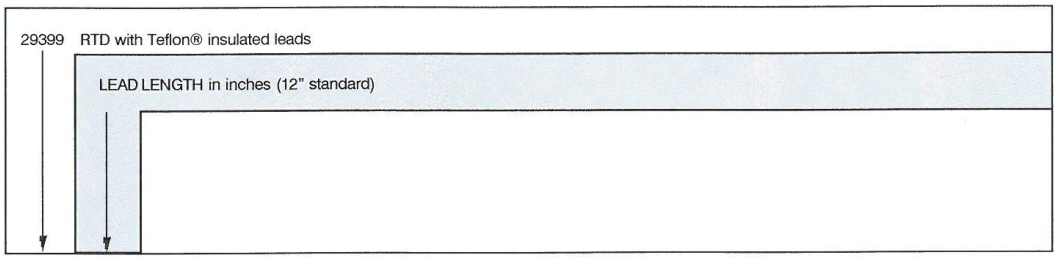

29399 – 12 – Typical write-up for 29399

RdF Specialists in Temperature Measurement
RdF Corporation • 23 Elm Avenue, Hudson, NH 03051-0490
800.445.8367 / 603.882.5195 • fax 603.882.6925 • sensor@rdfcorp.com
www.rdfcorp.com

Proudly manufactured in USA

AS9100 ISO 9001:2000 CERTIFIED COMPANY

R-SCAPLC 09/04 Rev - PRINTED IN USA

Appendix G: 3M Aluminum Foil Tape Specification Sheet

3M

Aluminum Foil Tape

425 • 427

Technical Data **July, 2004**

Product Description

3M™ Aluminum Foil Tapes 425 and 427 are 5 mil nominal dead soft aluminum foil backing combined with a transparent acrylic adhesive. 3M aluminum foil tape 427 offers an easy-release liner.

Product Construction

Backing	Adhesive	Color	Liner	Standard Roll Length
Dead soft aluminum	Acrylic	Shiny silver	Easy-release paper (3M aluminum foil tape 427)	60 yds. (55 m)

Typical Physical Properties

Note: The following technical information and data should be considered representative or typical only and should not be used for specification purposes.

		ASTM Test Method
Adhesion to Steel: 3M aluminum foil tape 425 3M aluminum foil tape 427	 47 oz./in. width (51 N/100 mm) 50 oz./in. width (55 N/100 mm)	D-3330
Tensile Strength:	30 lbs./in. width (525 N/100 mm)	D-3759
Backing Thickness:	2.8 mils (0.07 mm)	D-3652
Total Tape Thickness:	4.6 mils (0.12 mm)	D-3652
Liner Thickness: 3M aluminum foil tape 427	 3.1 mils (0.08 mm)	D-3652
Elongation at Break:	8%	D-3759
Temperature Use Range:	-65° to 300°F (-54° to 149°C)	
Water Vapor Transmission Rate:	0.1g H_2O/100 sq. in./24 hrs. (1.55 g/m^2/24 hrs.)	D-3833
Approximate Weight:	0.013 lbs./yd./in. width (4.77 gms/m/24 mm)	

Features

- Flame resistant. Meets U.L. 746C (File E 122798) and 723, Class "L" low flammability rating (File R 7311).
- Can be certified to meet SAE-AMS-T-23397 and L-T-80B.
- Meets requirements of F.A.R. 25.853(a).
- The very low moisture vapor transmission rate makes these tapes a good sealant.
- The acrylic adhesive, combined with the durable aluminum backing, offers ideal properties for long serviceable life in and outdoors.
- Good candidate as a maskant in electroplating of aluminum because it will not contaminate the bath.
- Aluminum backing provides excellent reflection of both heat and light.
- Best results obtained when applied to a clean, dry surface above 32°F (0°C).

IMPORTANT: These tapes are not intended for medical usage. Neither 3M nor the Food and Drug Administration have evaluated or reviewed this tape for medical application. 3M does not recommend or endorse the usage of the aluminum tape for medical application. User assumes all risk and liability whatsoever in connection with usage of product in a medical application.

Appendix H: Kaman KD5100 Calibration Sheets

KAMAN PRECISION PRODUCTS
MEASURING AND MEMORY
217 SMITH STREET
MIDDLETOWN, CONNECTICUT 06457
CUSTOMER SERVICE (860) 632-4442

CALIBRATION RECORD

CUSTOMER: MIT Lincoln Labs DATE: 24-Sep-12

CUSTOMER P.O.# : 7000208501
KAMAN S/O # : S1208203
SYSTEM MODEL NO.: KD5100-15N004A

SYSTEM SN: S1208203-01-01
SENSOR SN: S1208203-01-01 S2
SENSOR SN: S1208203-01-01 S4

DISPLACEMENT MM	OUTPUT VOLTS	LEAST SQUARES FIT VOLTS	NON-LINEARITY % FSO
-0.080	-10.026	-10.021	-0.03%
-0.064	-8.019	-8.023	0.02%
-0.048	-6.009	-6.025	0.08%
-0.032	-4.016	-4.027	0.05%
-0.016	-2.019	-2.029	0.05%
0.000	-0.036	-0.031	-0.03%
0.016	1.955	1.967	-0.06%
0.032	3.922	3.965	-0.22%
0.048	5.950	5.963	-0.07%
0.064	7.956	7.961	-0.03%
0.080	10.004	9.959	0.22%

SUPPLY VOLTAGE (VOLTS ±15
TARGET MATERIAL: Aluminum
TARGET CURVATURE: Flat
CALIBRATION NULL (MM): 0.25
P/N: 855273-048
NOTES:
CHANNEL #: B

NON-LIN SPEC: 0.50%
MAX NON-LIN: 0.22%
SCALE (V/MM): 124.873

Minor vertical Y-Axis

CALIBRATION TECHNICIAN: Larry Brown
L.Brown

FORM 235 4/6/10

KAMAN PRECISION PRODUCTS
MEASURING AND MEMORY
217 SMITH STREET
MIDDLETOWN, CONNECTICUT 06457
CUSTOMER SERVICE (860) 632-4442

CALIBRATION RECORD

CUSTOMER: MIT Lincoln Labs DATE: 21-Sep-12

CUSTOMER P.O.# : 7000208501
KAMAN S/O # : S1208203
SYSTEM MODEL NO.: KD5100-15N004A

SYSTEM SN: S1208203-01-01
SENSOR SN: S1208203-01-01 S1
SENSOR SN: S1208203-01-01 S3

DISPLACEMENT MM	OUTPUT VOLTS	LEAST SQUARES FIT VOLTS	NON-LINEARITY % FSO
-0.080	-10.002	-10.042	0.20%
-0.064	-8.028	-8.039	0.06%
-0.048	-6.048	-6.037	-0.06%
-0.032	-4.064	-4.034	-0.15%
-0.016	-2.048	-2.032	-0.08%
0.000	-0.045	-0.029	-0.08%
0.016	1.961	1.973	-0.06%
0.032	3.971	3.976	-0.02%
0.048	5.990	5.979	0.06%
0.064	7.992	7.981	0.05%
0.080	10.000	9.984	0.08%

SUPPLY VOLTAGE (VOLTS	±15	NON-LIN SPEC:	0.50%
TARGET MATERIAL:	Aluminum	MAX NON-LIN:	0.20%
TARGET CURVATURE:	Flat	SCALE (V/MM):	125.161
CALIBRATION NULL (MM):	0.25		
P/N:	855273-048		
NOTES:			
CHANNEL #:	A		

Major Horizontal x-axis

CALIBRATION TECHNICIAN: Larry Brown
L.Brown

FORM 235 4/6/10

Appendix I: Room Temperature Hysteresis Data

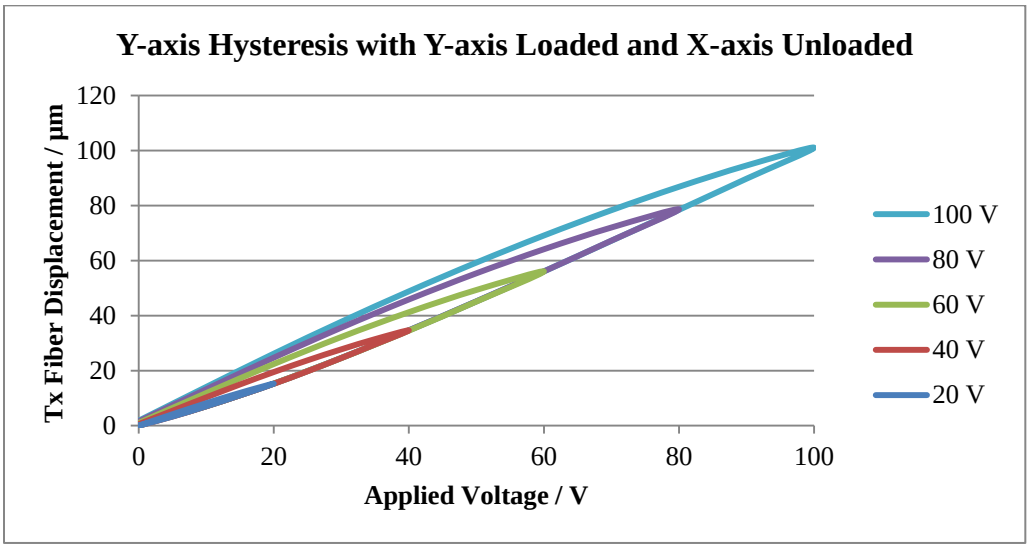

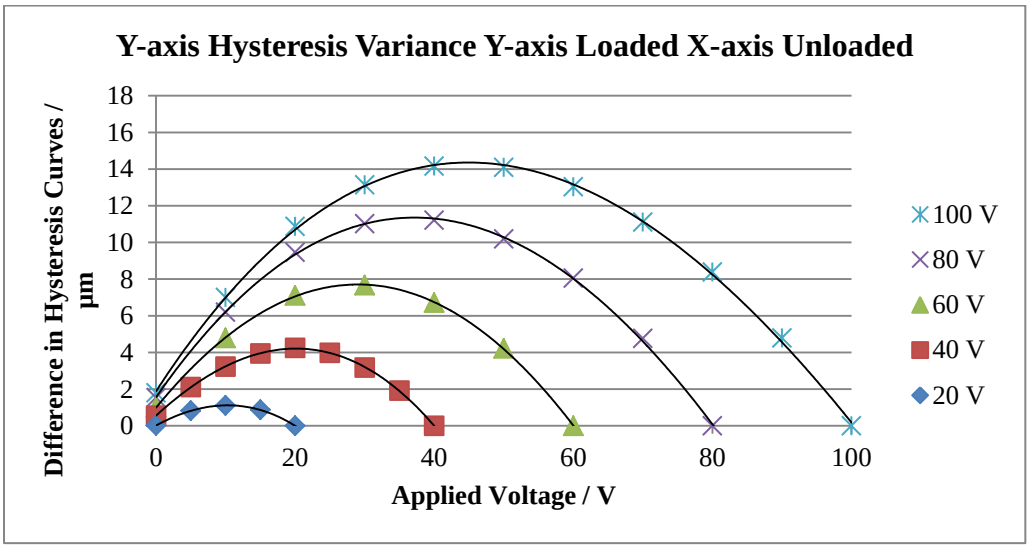

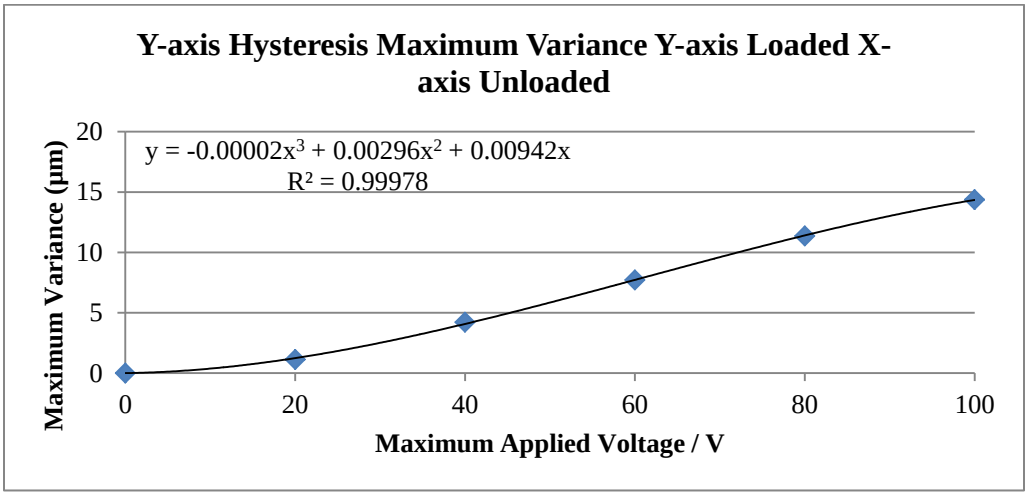

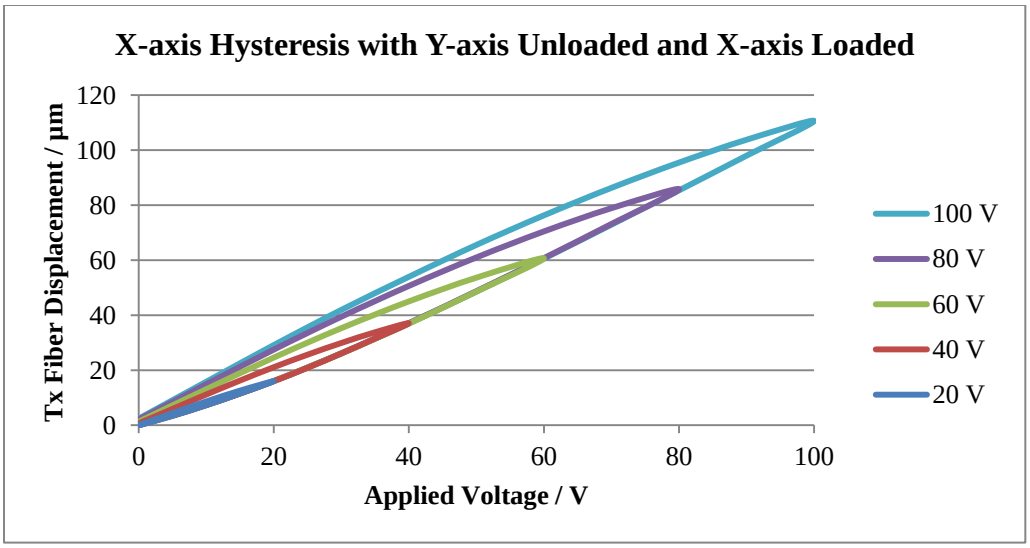
X-axis Hysteresis with Y-axis Unloaded and X-axis Loaded
Tx Fiber Displacement / µm
120
100
80
60
40
20
0
0
20
40
60
80
100
Applied Voltage / V
100 V
80 V
60 V
40 V
20 V

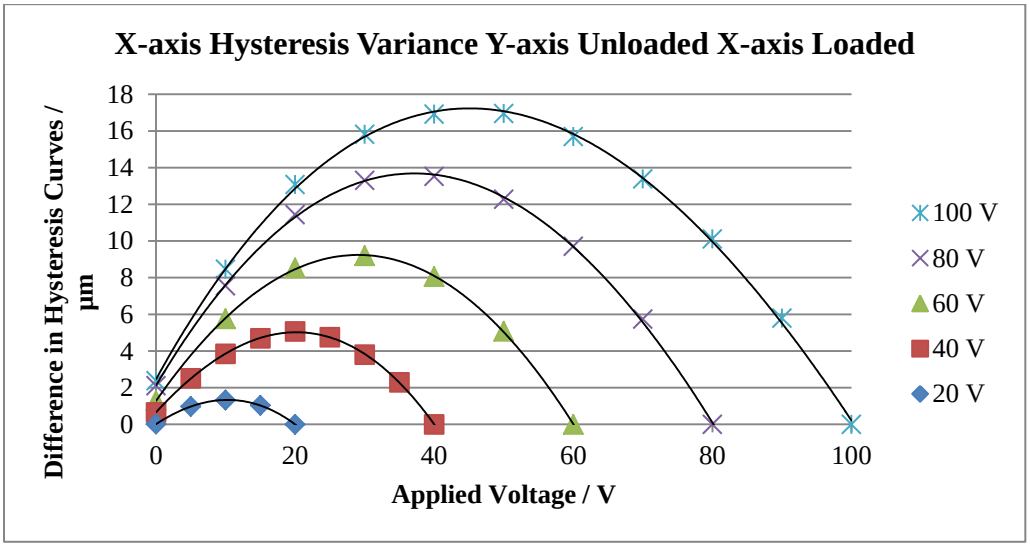
X-axis Hysteresis Variance Y-axis Unloaded X-axis Loaded
Difference in Hysteresis Curves / µm
18
16
14
12
10
8
6
4
2
0
0
20
40
60
80
100
Applied Voltage / V
100 V
80 V
60 V
40 V
20 V

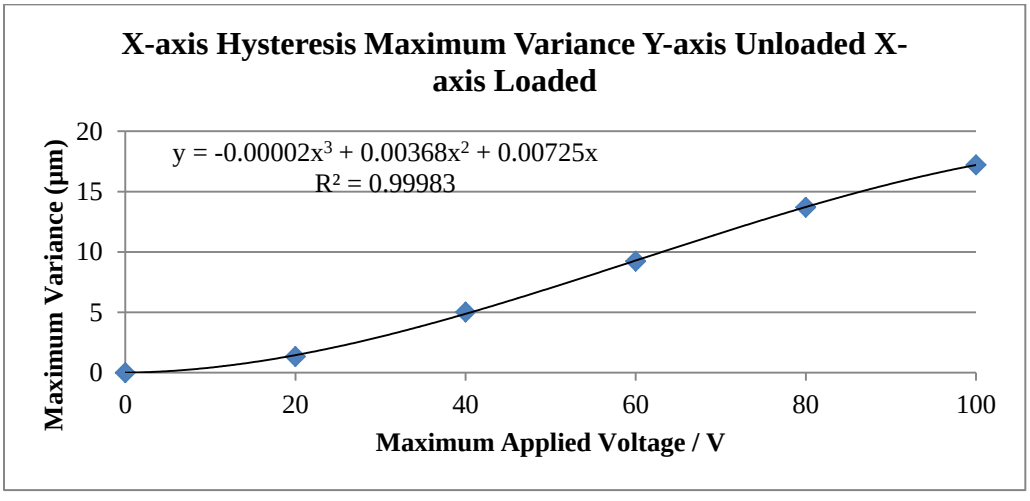
X-axis Hysteresis Maximum Variance Y-axis Unloaded X-axis Loaded
Maximum Variance (µm)
20
15
10
5
0
y = -0.00002x3 + 0.00368x2 + 0.00725x
R² = 0.99983
0
20
40
60
80
100
Maximum Applied Voltage / V

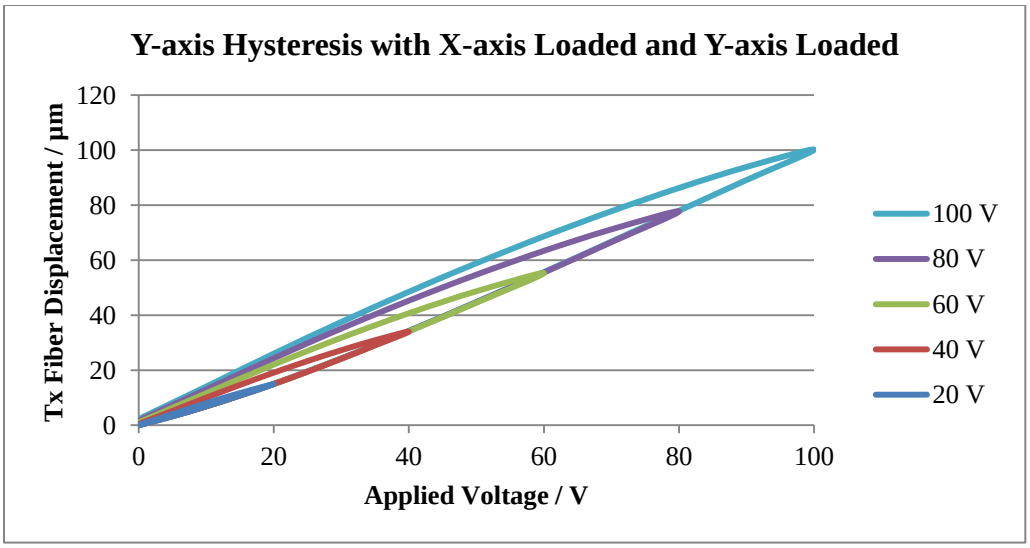
Y-axis Hysteresis with X-axis Loaded and Y-axis Loaded
Tx Fiber Displacement / µm
120
100
80
60
40
20
0
0
20
40
60
80
100
Applied Voltage / V
100 V
80 V
60 V
40 V
20 V

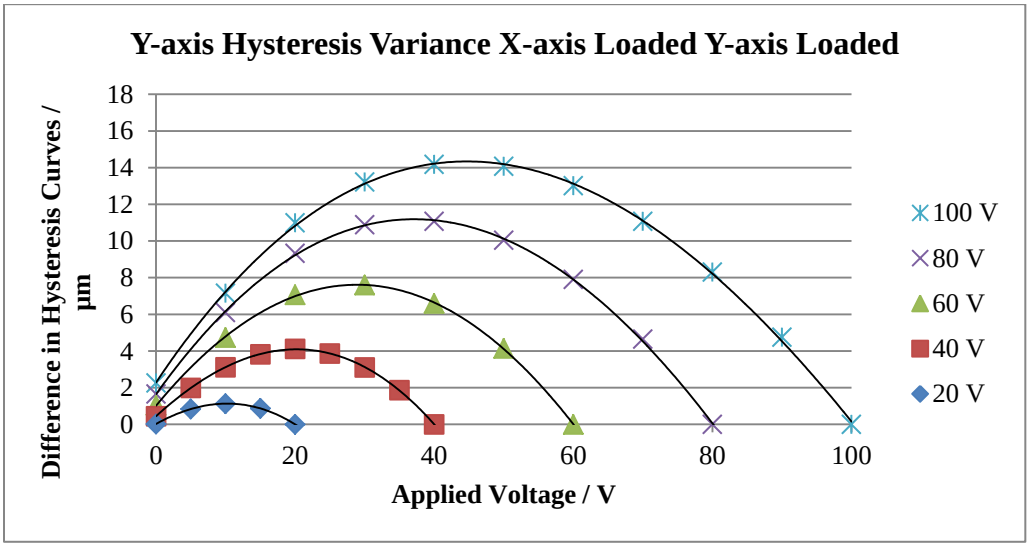
Y-axis Hysteresis Variance X-axis Loaded Y-axis Loaded
Difference in Hysteresis Curves / µm
18
16
14
12
10
8
6
4
2
0
0
20
40
60
80
100
Applied Voltage / V
100 V
80 V
60 V
40 V
20 V

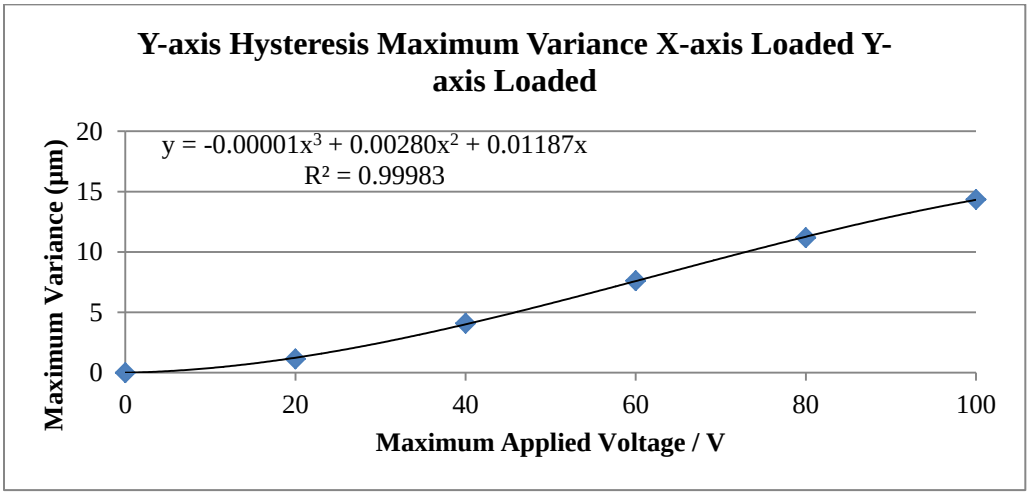
Y-axis Hysteresis Maximum Variance X-axis Loaded Y-axis Loaded
y = -0.00001x³ + 0.00280x² + 0.01187x
R² = 0.99983
Maximum Variance (µm)
20
15
10
5
0
0
20
40
60
80
100
Maximum Applied Voltage / V

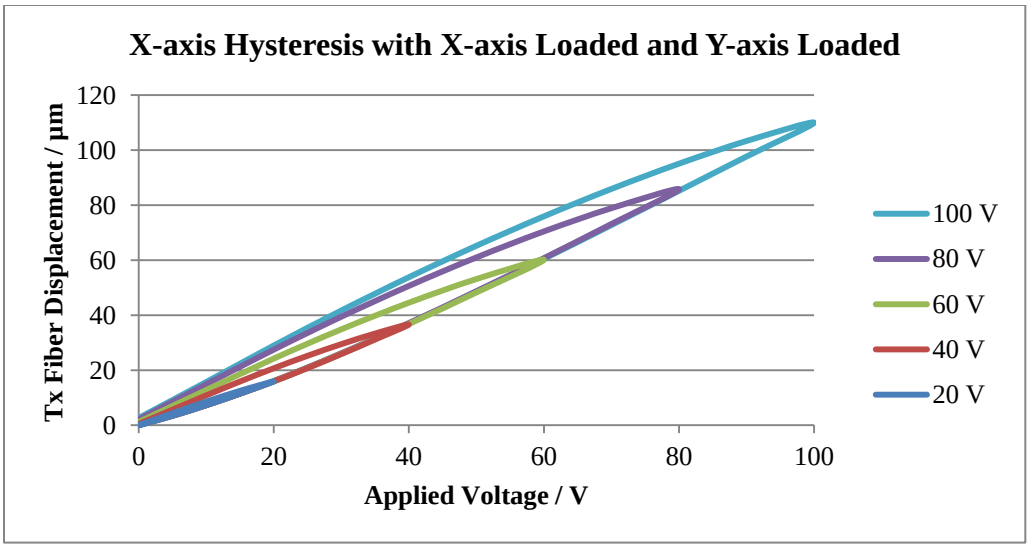
X-axis Hysteresis with X-axis Loaded and Y-axis Loaded
Tx Fiber Displacement / µm
120
100
80
60
40
20
0
0
20
40
60
80
100
Applied Voltage / V
100 V
80 V
60 V
40 V
20 V

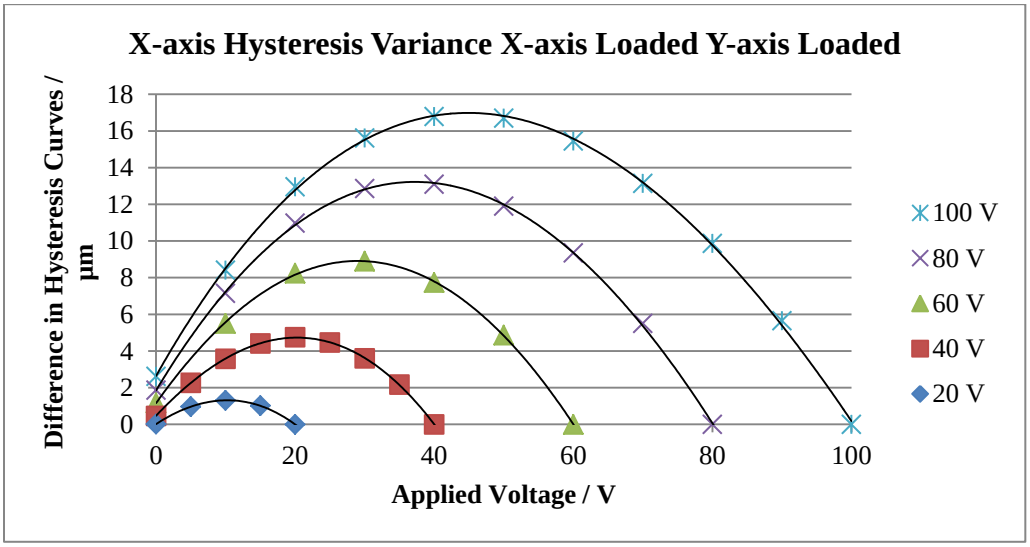
X-axis Hysteresis Variance X-axis Loaded Y-axis Loaded
Difference in Hysteresis Curves / µm
18
16
14
12
10
8
6
4
2
0
0
20
40
60
80
100
Applied Voltage / V
100 V
80 V
60 V
40 V
20 V

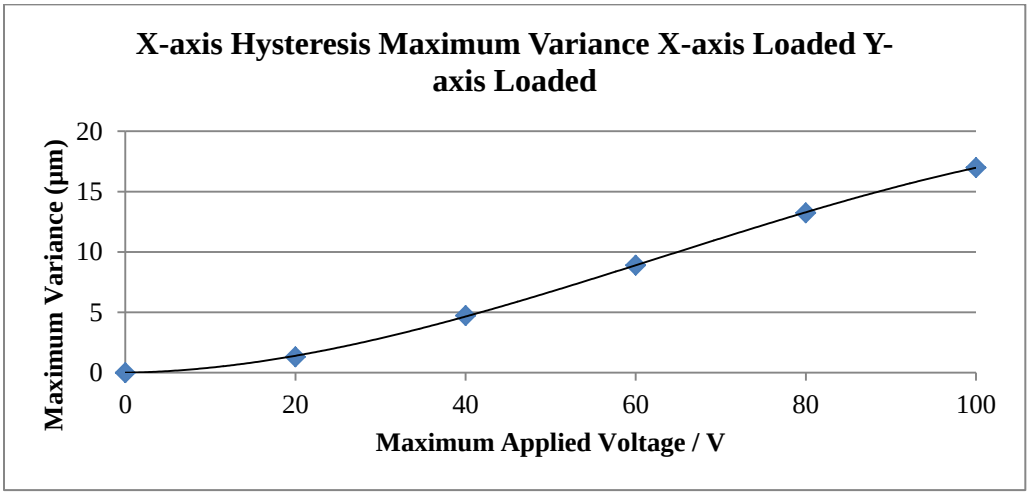
X-axis Hysteresis Maximum Variance X-axis Loaded Y-axis Loaded
Maximum Variance (µm)
20
15
10
5
0
0
20
40
60
80
100
Maximum Applied Voltage / V

Appendix J: Creep Graphs

Sample Creep Graphs:

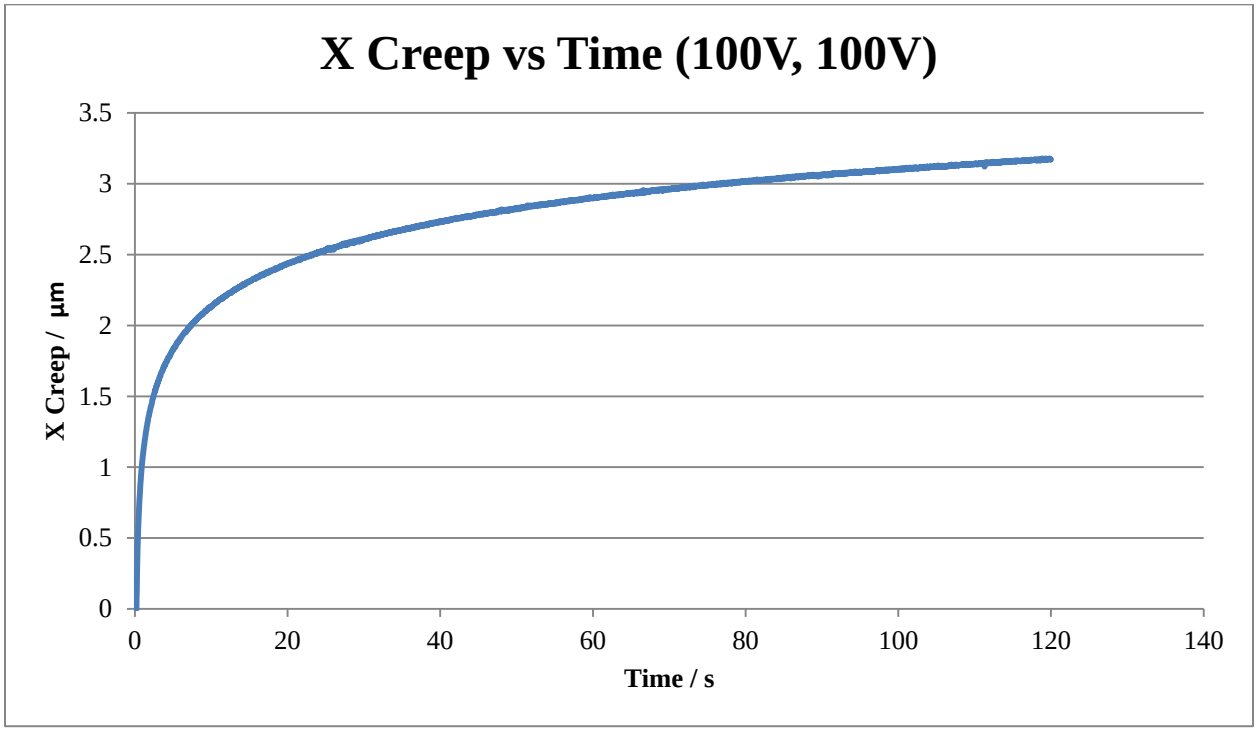

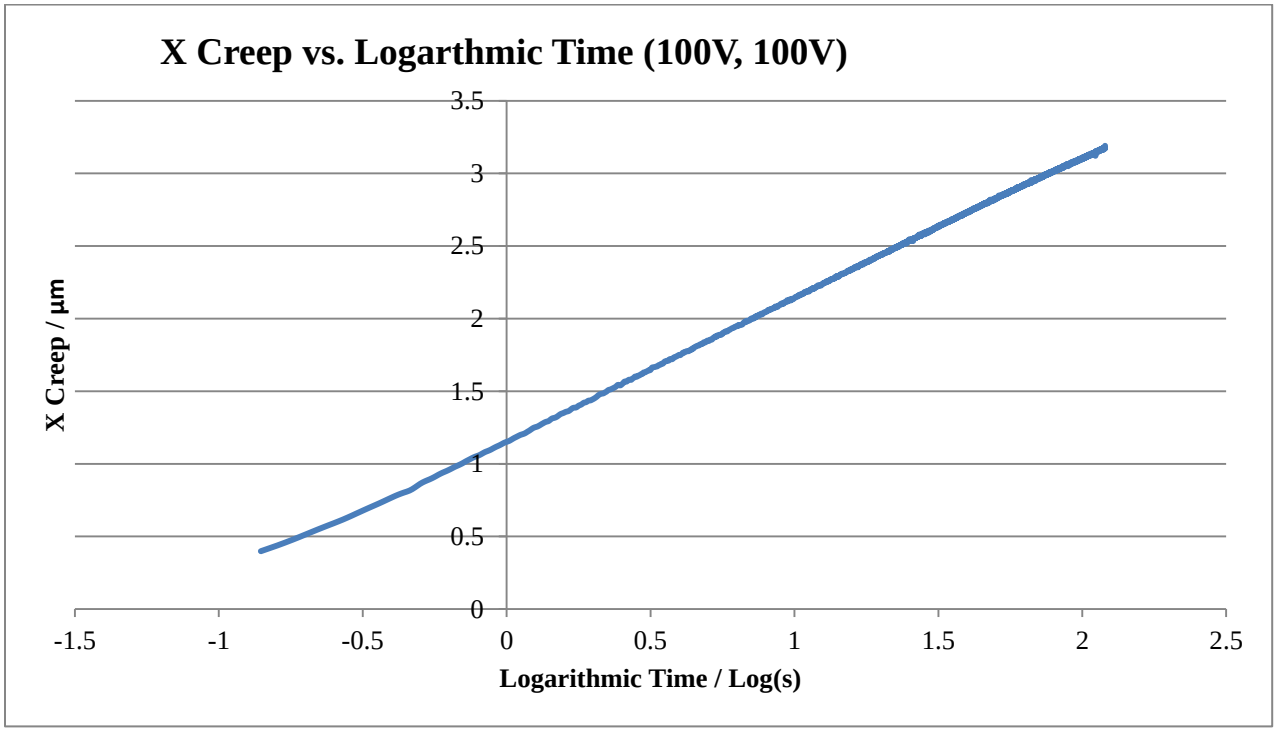

With voltage applied to the displacing axis only:

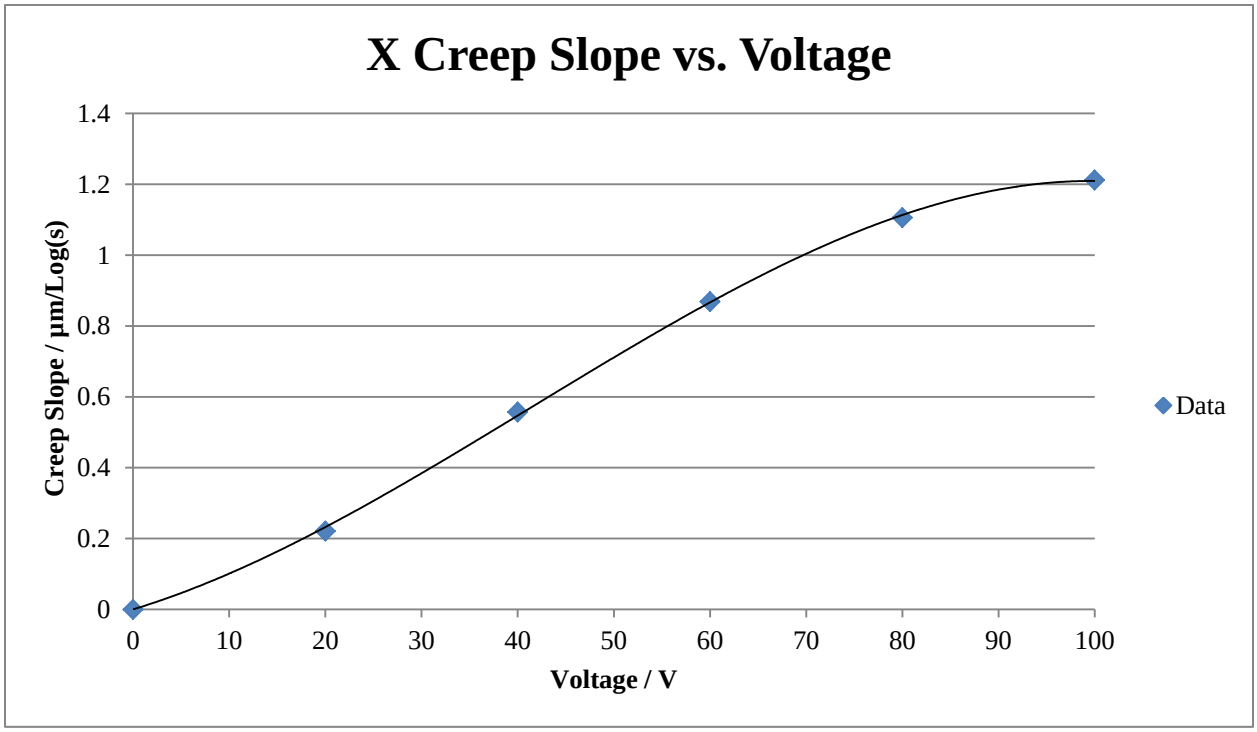

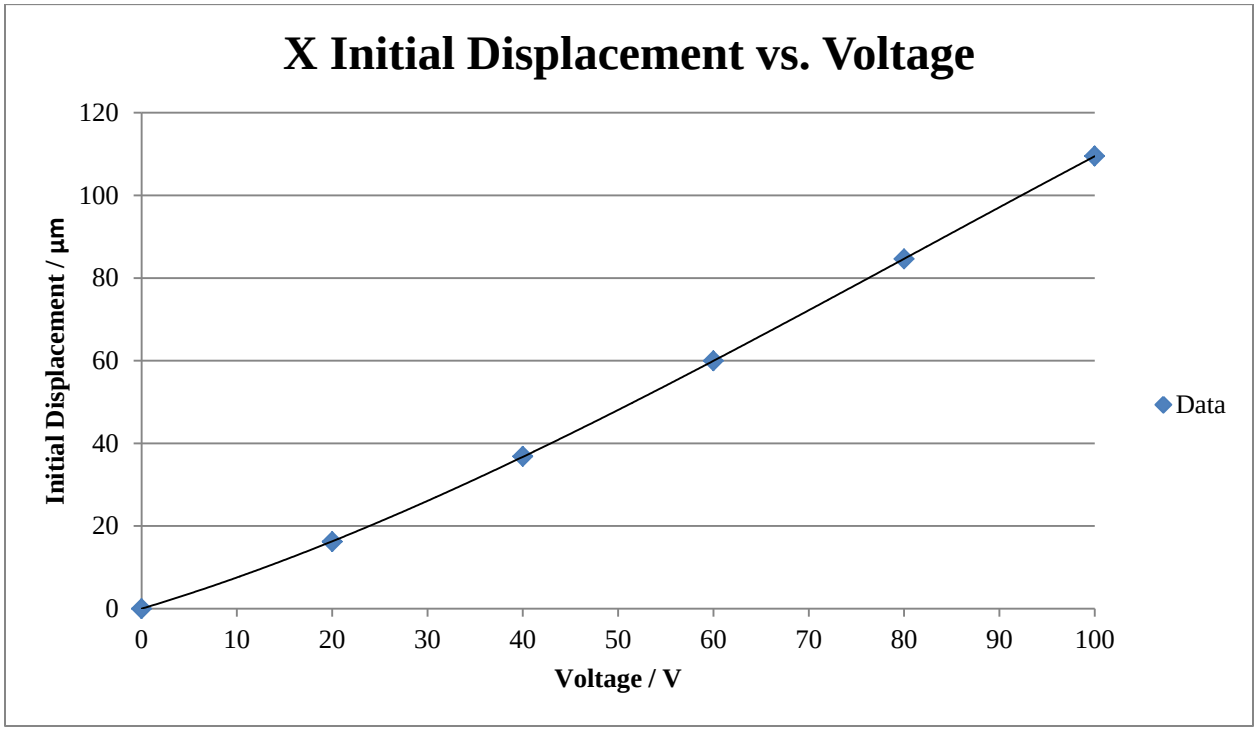

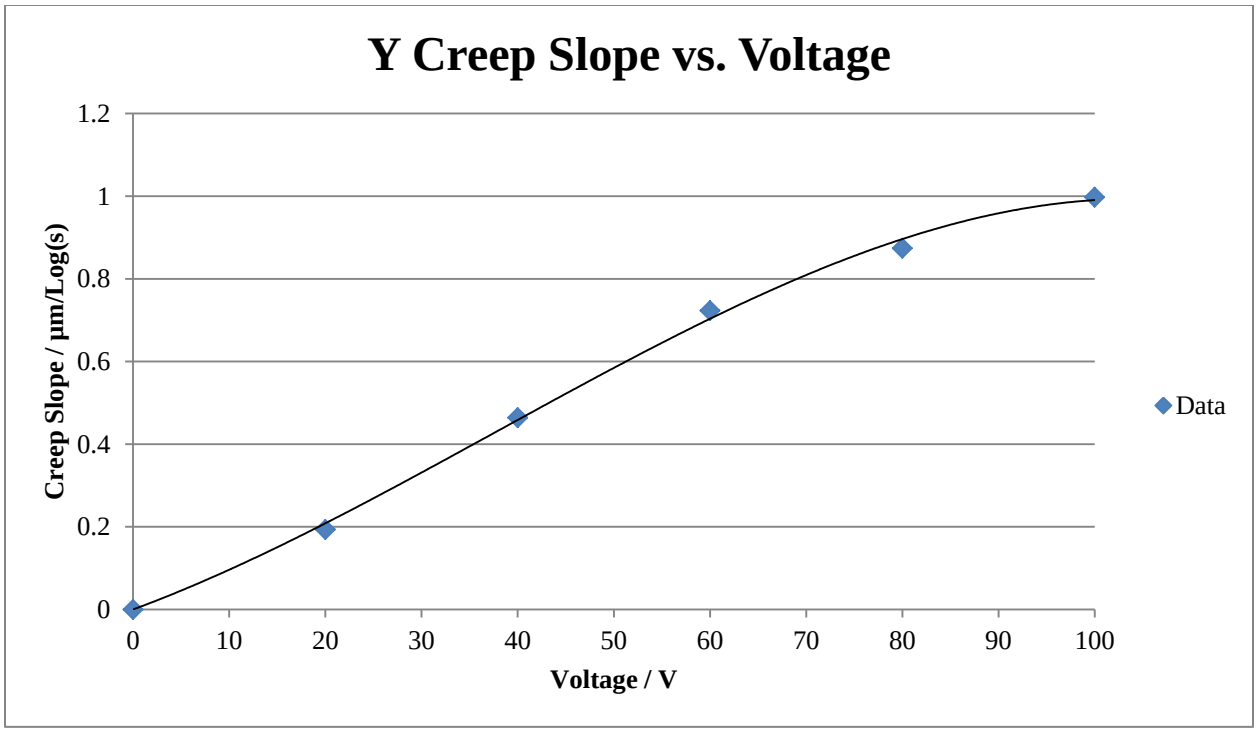
Y Creep Slope vs. Voltage
Creep Slope / µm/Log(s)
1.2
1
0.8
0.6
0.4
0.2
0
0
10
20
30
40
50
60
70
80
90
100
Voltage / V
Data

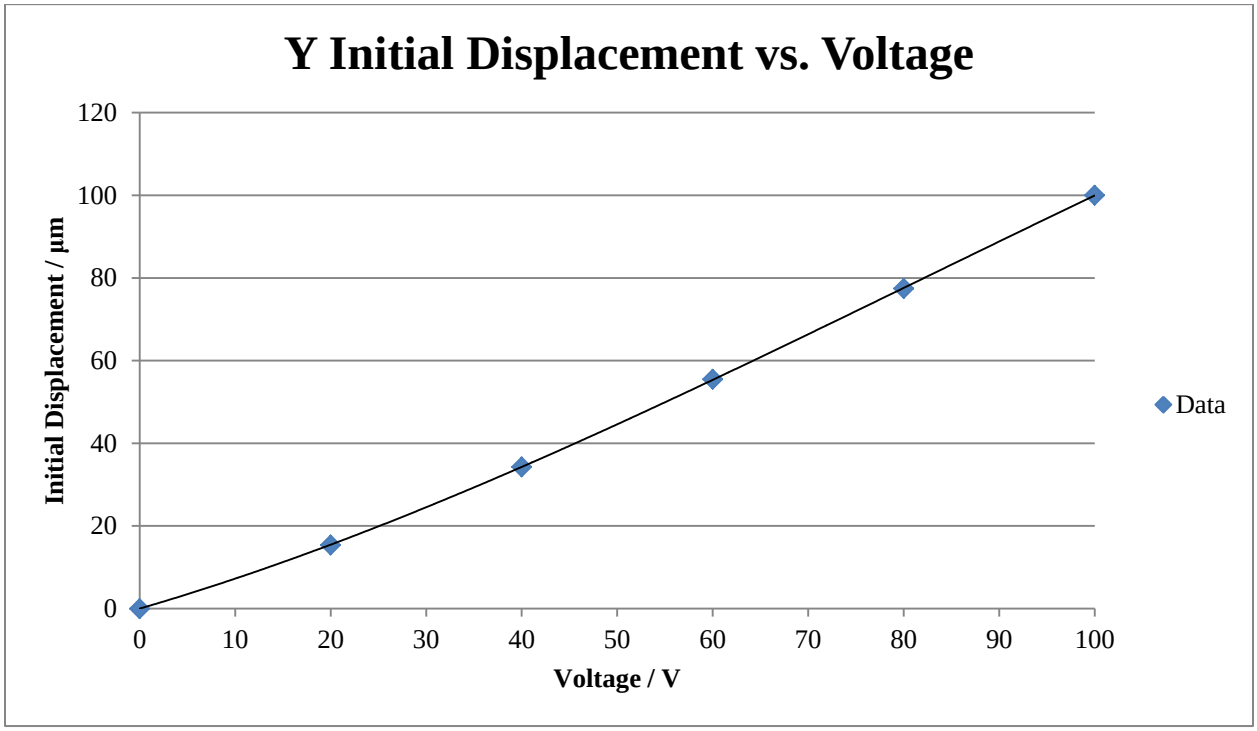
Y Initial Displacement vs. Voltage
Initial Displacement / µm
120
100
80
60
40
20
0
0
10
20
30
40
50
60
70
80
90
100
Voltage / V
Data

With voltage applied to both axes:

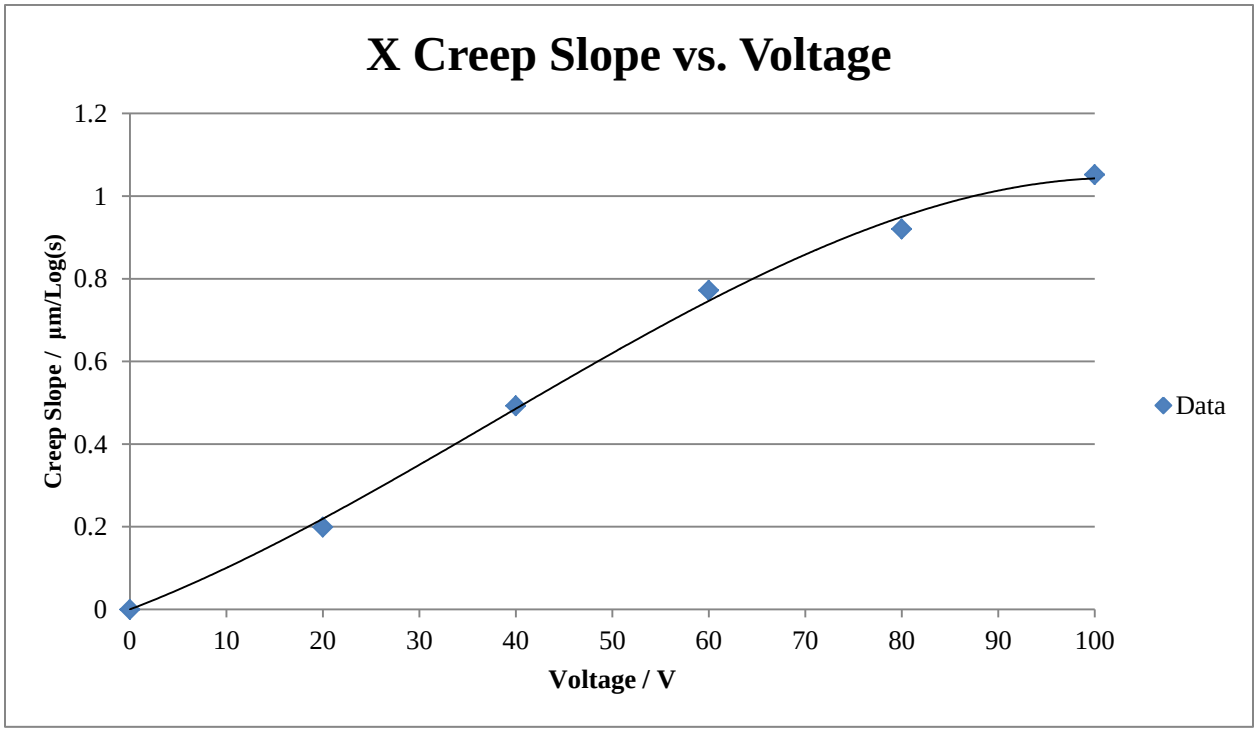

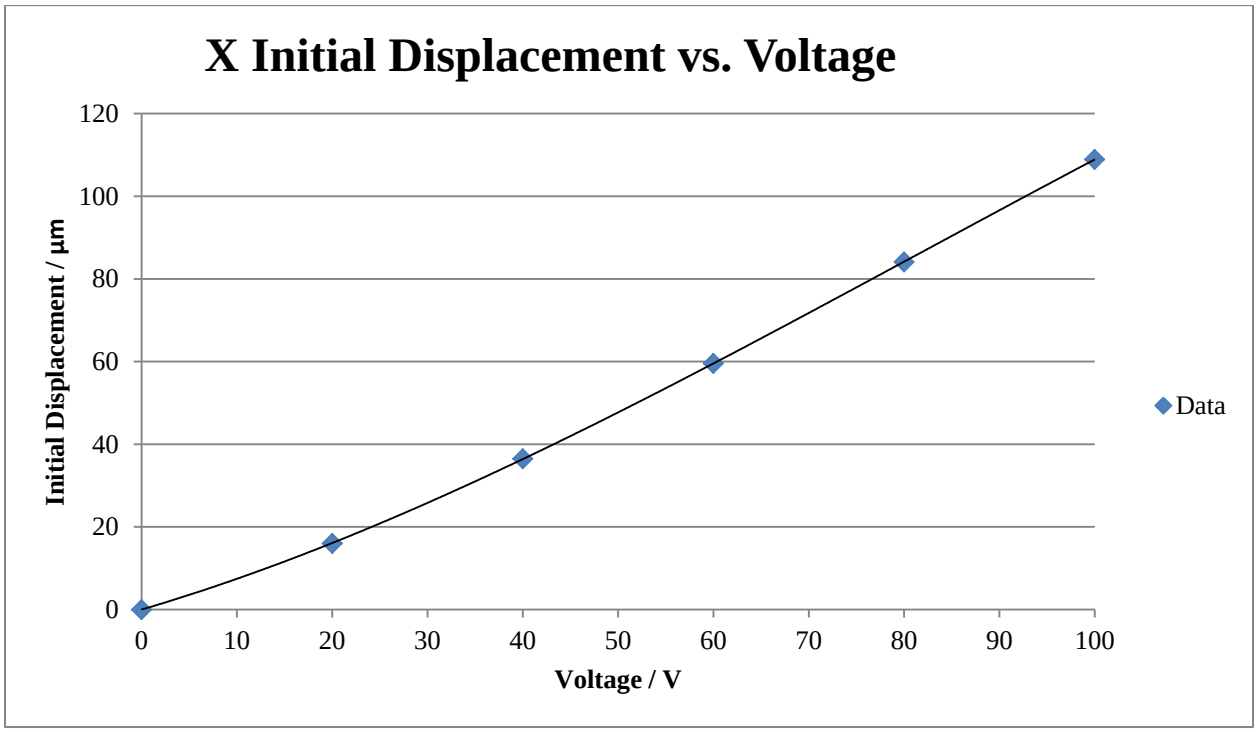

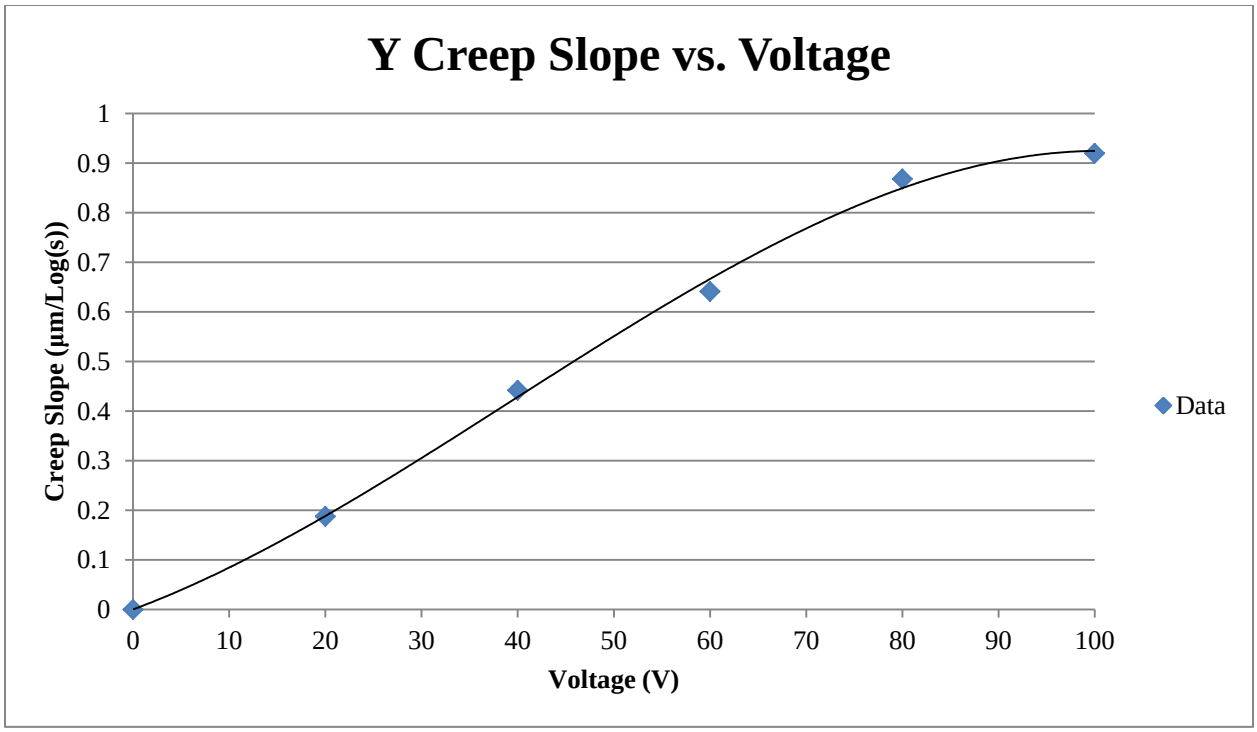
Y Creep Slope vs. Voltage
Creep Slope (µm/Log(s))
1
0.9
0.8
0.7
0.6
0.5
0.4
0.3
0.2
0.1
0
0
10
20
30
40
50
60
70
80
90
100
Voltage (V)
Data

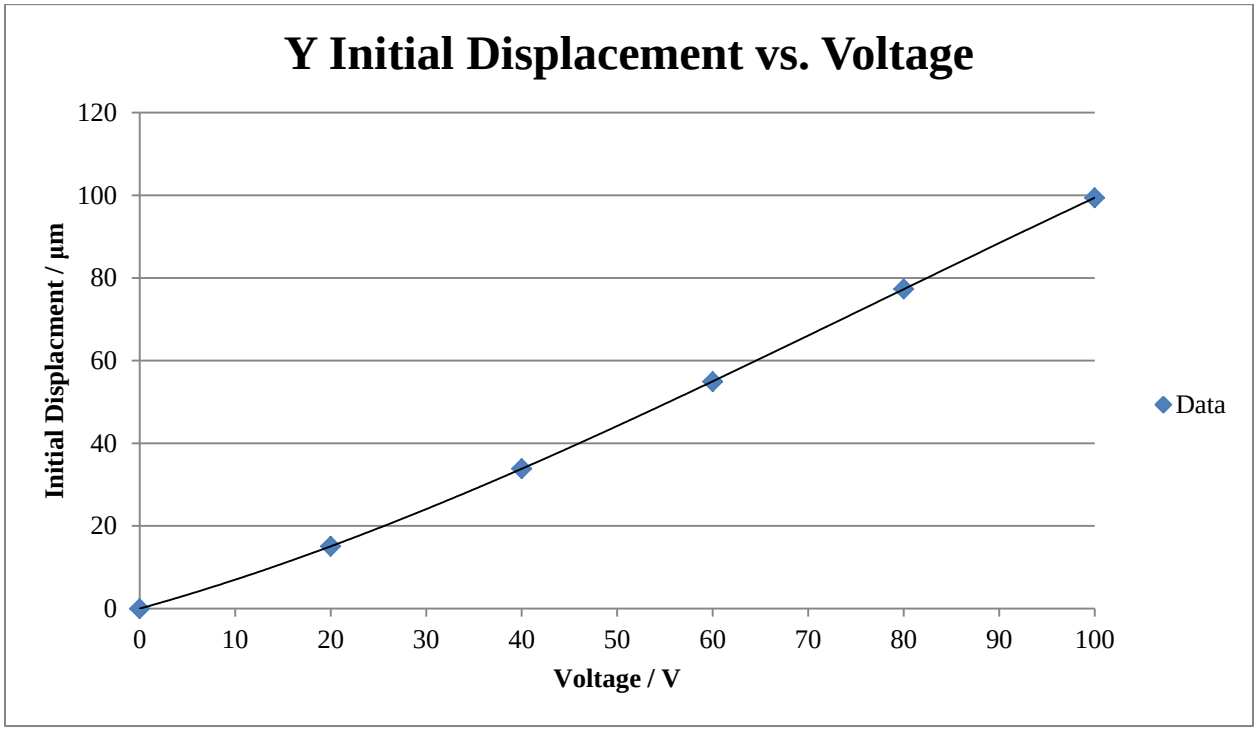
Y Initial Displacement vs. Voltage
Initial Displacment / µm
120
100
80
60
40
20
0
0
10
20
30
40
50
60
70
80
90
100
Voltage / V
Data

Appendix K: Creep Charts

X Creep Data at t=120 s
Voltage on the X Axis

Voltage	Displacement (µm)
20	0.77
40	1.88
60	2.87
80	3.65
100	4.04

0 Y Creep Data at t= 120 s
Voltage on the Y Axis

Voltage	Displacement (µm)
20	0.69
40	1.59
60	2.41
80	2.88
100	3.29

X Creep Data at t= 120 s
Voltage on X and Y Axes

Voltage	Displacement (µm)
20	0.69
40	1.68
60	2.43
80	3.09
100	3.51

Y Creep data at t=120 s
Voltage on X and Y Axes

Voltage	Displacement (µm)
20	0.66
40	1.5
60	2.11
80	2.87
100	3.06

Appendix L: Temperature Profiles

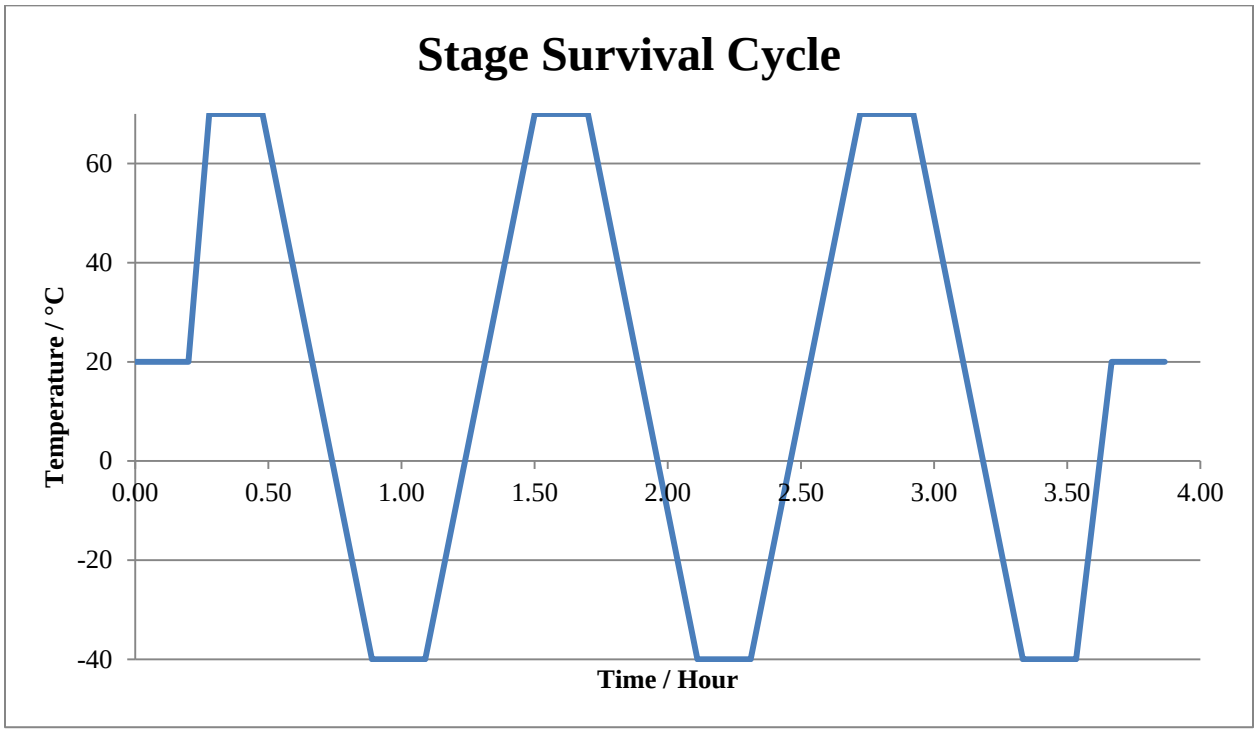

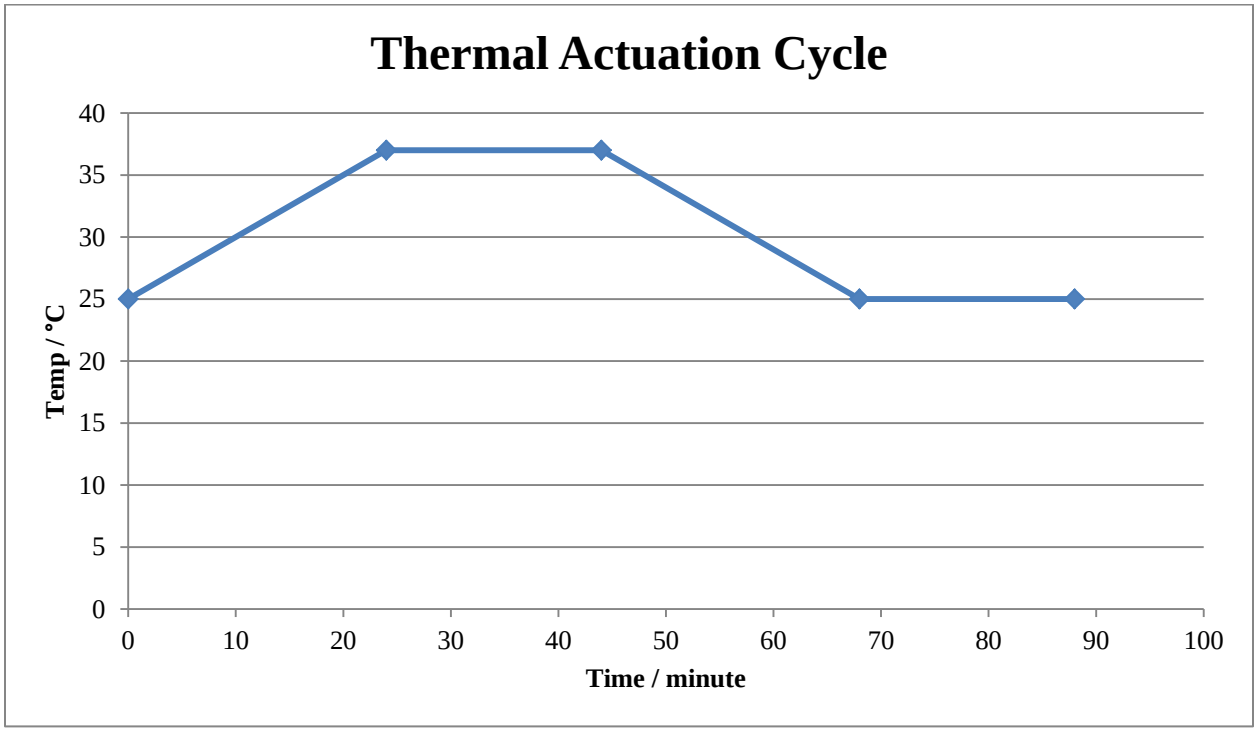

Appendix M: Sensor Drift Graph

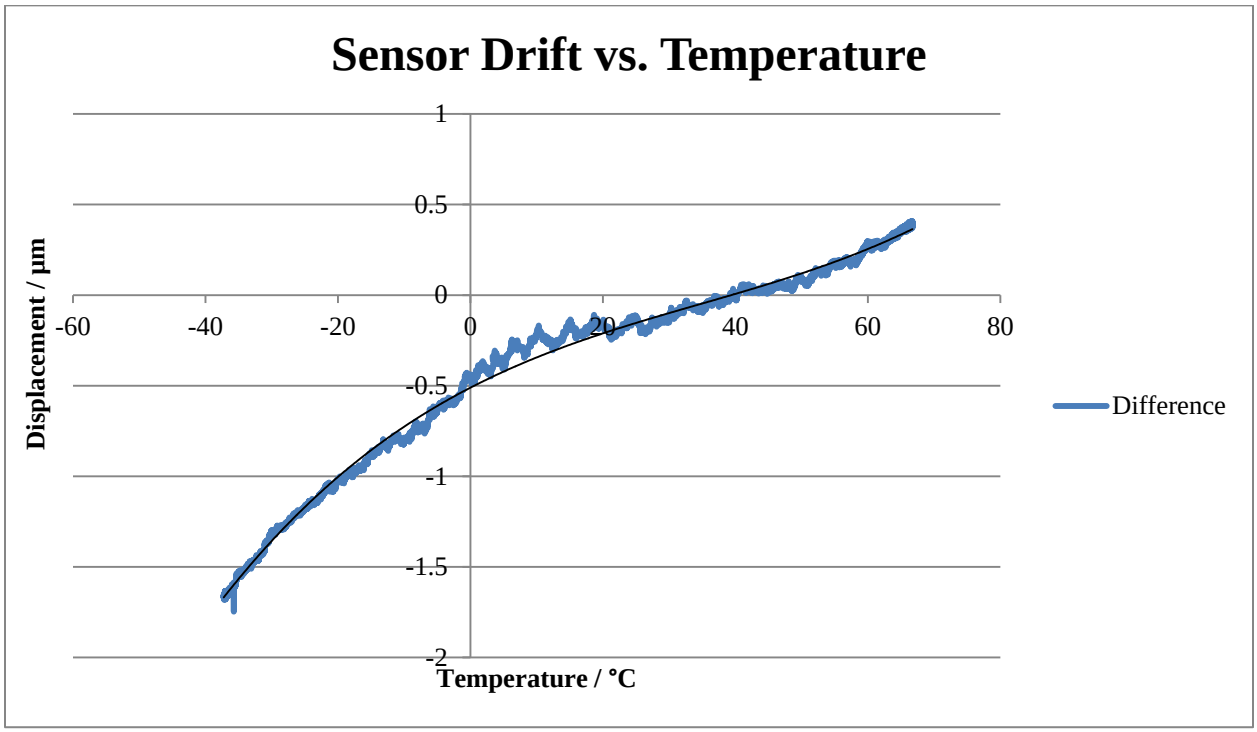

Appendix N: Thermal Actuation Graphs (10 mil vs. 12 mil)

The temperature difference is between the crystals and the other components of the NPS

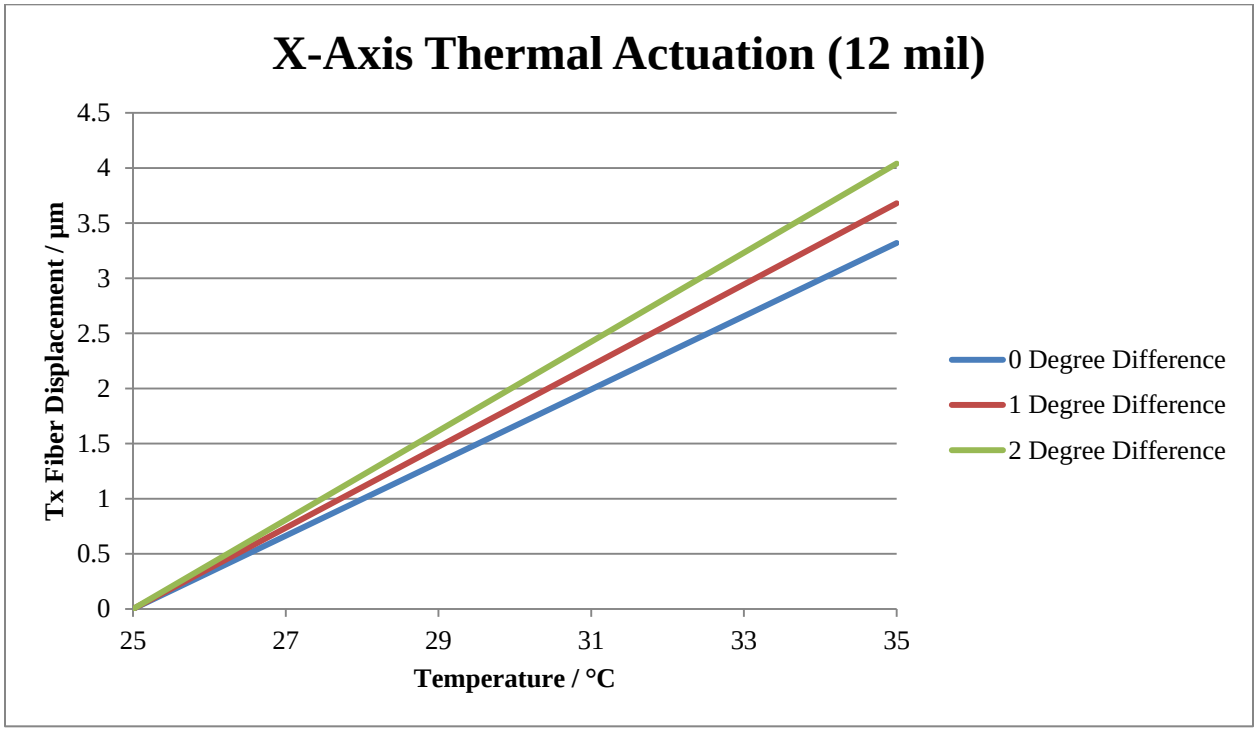

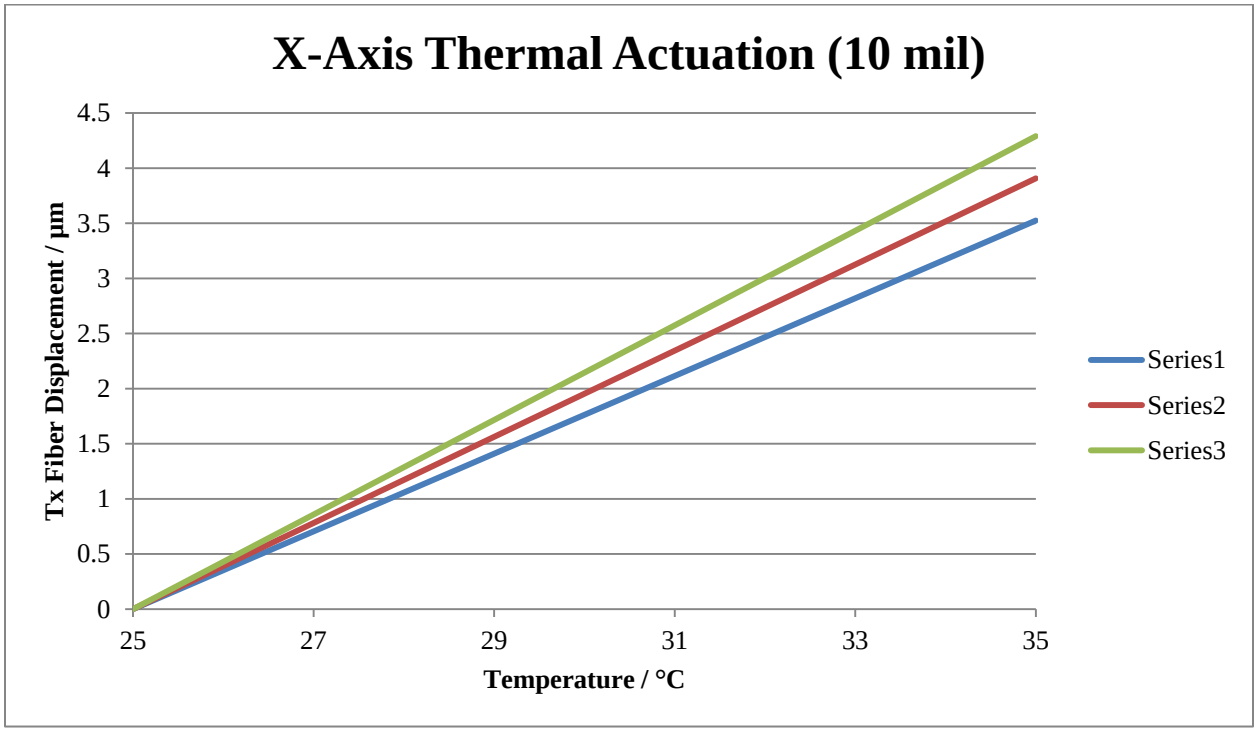

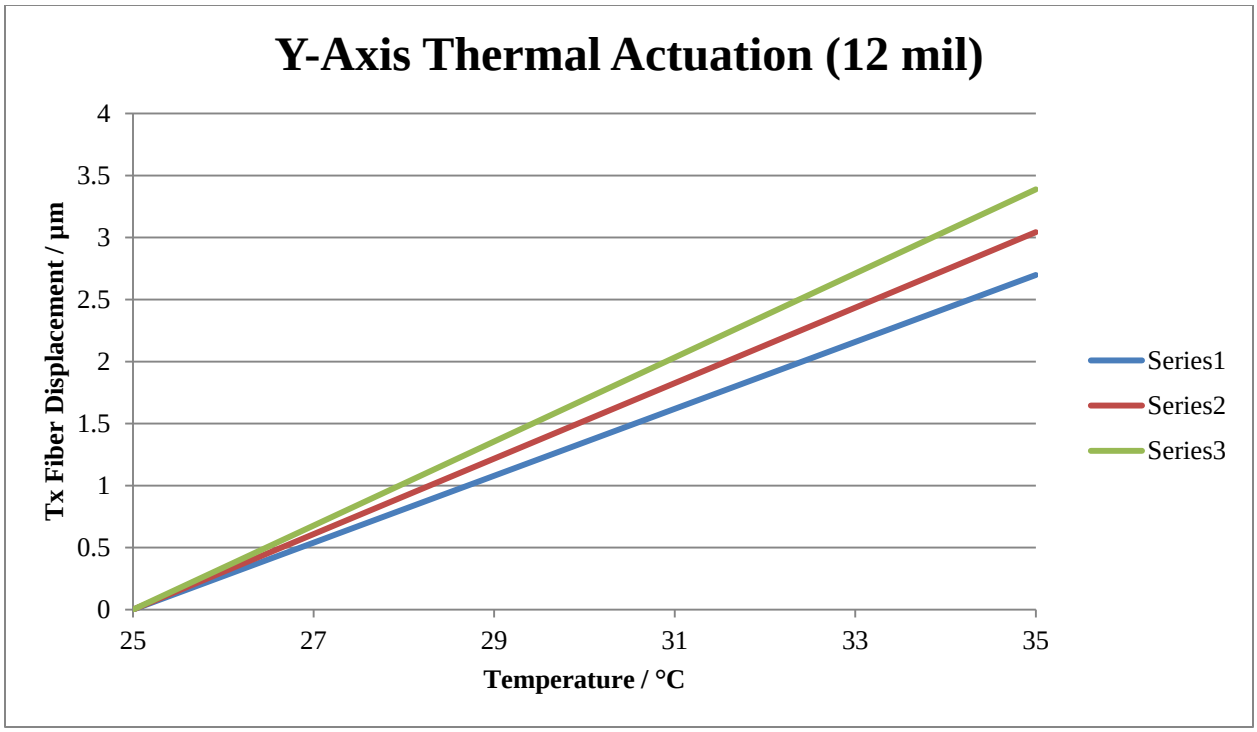
Y-Axis Thermal Actuation (12 mil)
Tx Fiber Displacement / µm
4
3.5
3
2.5
2
1.5
1
0.5
0
25
27
29
31
33
35
Temperature / °C
Series1
Series2
Series3

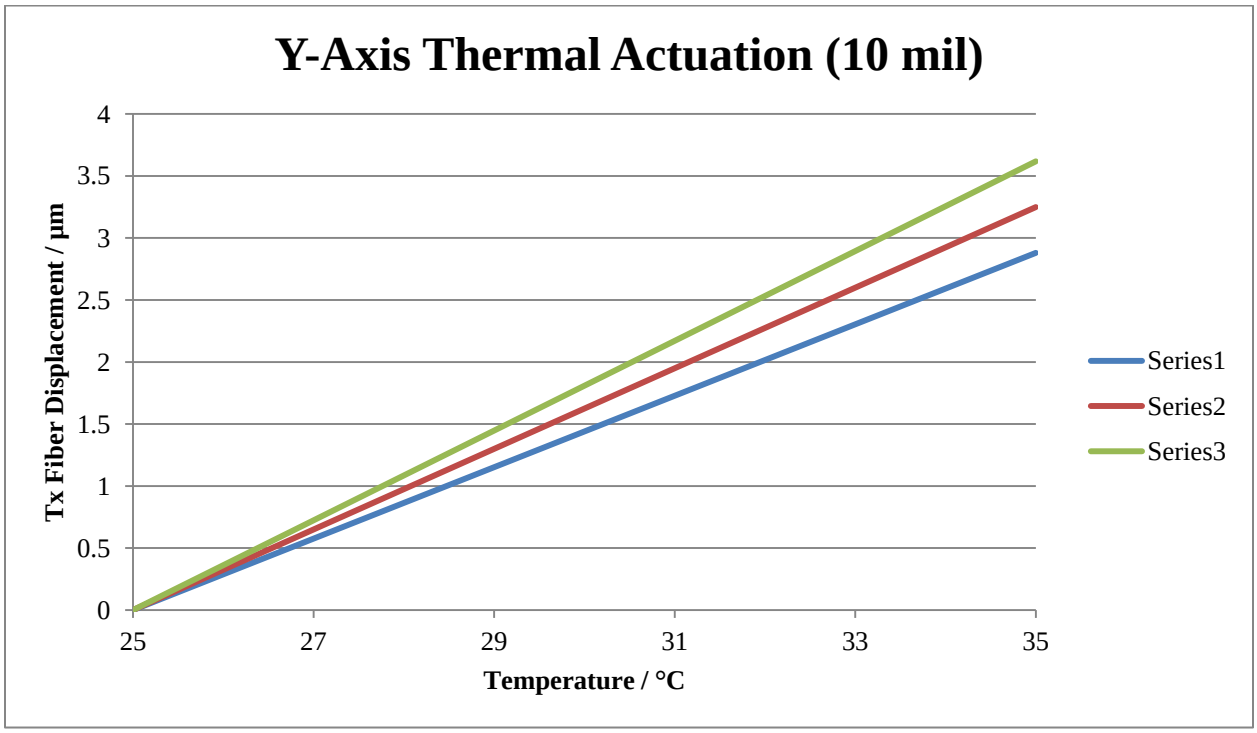
Y-Axis Thermal Actuation (10 mil)
Tx Fiber Displacement / µm
4
3.5
3
2.5
2
1.5
1
0.5
0
25
27
29
31
33
35
Temperature / °C
Series1
Series2
Series3